Theses and Dissertations   1. Thesis and Dissertation Collection, all items

2006-09

Reactive shear layer mixing and growth rate effects on afterburning properties for axisymetric rocket engine plumes

Hartsfield, Carl Rex.

Monterey, California.: Naval Postgraduate School, 2006.

https://hdl.handle.net/10945/10152

![NPS shield logo — PRAESTANTIA PER SCIENTIAM, 1909]

NAVAL POSTGRADUATE SCHOOL

MONTEREY, CALIFORNIA

DISSERTATION

REACTIVE SHEAR LAYER MIXING AND GROWTH RATE EFFECTS ON AFTERBURNING PROPERTIES FOR AXISYMETRIC ROCKET ENGINE PLUMES

by

Carl Rex Hartsfield

September 2006

Dissertation Supervisor:	Christopher M. Brophy
Committee Chairman:	Knox T. Millsaps

Approved for public release; distribution is unlimited

THIS PAGE INTENTIONALLY LEFT BLANK

REPORT DOCUMENTATION PAGE		*Form Approved OMB No. 0704-0188*
Public reporting burden for this collection of information is estimated to average 1 hour per response, including the time for reviewing instruction, searching existing data sources, gathering and maintaining the data needed, and completing and reviewing the collection of information. Send comments regarding this burden estimate or any other aspect of this collection of information, including suggestions for reducing this burden, to Washington headquarters Services, Directorate for Information Operations and Reports, 1215 Jefferson Davis Highway, Suite 1204, Arlington, VA 22202-4302, and to the Office of Management and Budget, Paperwork Reduction Project (0704-0188) Washington DC 20503.		

1. AGENCY USE ONLY (*Leave blank*)	2. REPORT DATE September 2006	3. REPORT TYPE AND DATES COVERED Dissertation	
4. TITLE AND SUBTITLE: Reactive Shear Layer Mixing and Growth Rate Effects on Afterburning Properties for Axisymetric Rocket Engine Plumes		5. FUNDING NUMBERS NF046110501013	
6. AUTHOR(S) Carl Rex Hartsfield			
7. PERFORMING ORGANIZATION NAME(S) AND ADDRESS(ES) Naval Postgraduate School Monterey, CA 93943-5000		8. PERFORMING ORGANIZATION REPORT NUMBER	
9. SPONSORING / MONITORING AGENCY NAME(S) AND ADDRESS(ES) AFRL/PRSA Edwards AFB CA		10. SPONSORING / MONITORING AGENCY REPORT NUMBER	
11. SUPPLEMENTARY NOTES The views expressed in this thesis are those of the author and do not reflect the official policy or position of the Department of Defense or the U.S. Government.			
12a. DISTRIBUTION / AVAILABILITY STATEMENT Approved for public release; distribution is unlimited		12b. DISTRIBUTION CODE	

13. ABSTRACT (*maximum 200 words*)

A semi-empirical model was developed for predicting the afterburning ignition location of film cooled rocket engines. The model is based on two characteristic distances, the distance required for turbulent mixing to generate a combustible mixture with the reactive film layer and the distance traveled during the ignition delay. The mixing length is affected by the mass flow, composition of the film cooling layer and the fuel-rich air to fuel ratio required to support combustion. The ignition delay is determined by the composition directly through the auto-ignition reaction time. Both distances are affected by the velocity and temperature of the rocket core and air. This model was experimentally verified over a range of co-flow air velocities using a liquid rocket engine of approximately 440 N thrust, varying amounts of reactive film cooling and compositions of film coolant, and a co-axial annular airflow generator producing airflow at velocities up to nearly 200 m/s. Mean ignition locations experimentally observed were between 3.8 and 9.8 centimeters from the nozzle lip and varied due to the airstream velocity, and film coolant composition and mass flow. All model predictions were within the standard deviation of the experimentally observed ignition points.

14. SUBJECT TERMS Rocket Exhaust Plume, Afterburning, Compressible Shear Layer, Turbulent Mixing			15. NUMBER OF PAGES 179
			16. PRICE CODE

17. SECURITY CLASSIFICATION OF REPORT Unclassified	18. SECURITY CLASSIFICATION OF THIS PAGE Unclassified	19. SECURITY CLASSIFICATION OF ABSTRACT Unclassified	20. LIMITATION OF ABSTRACT UL

THIS PAGE INTENTIONALLY LEFT BLANK

REACTIVE SHEAR LAYER MIXING AND GROWTH RATE EFFECTS ON AFTERBURNING PROPERTIES FOR AXISYMETRIC ROCKET ENGINE PLUMES

Carl Rex Hartsfield
Major, United States Air Force
B.A.E., Georgia Institute of Technology, 1991
M.S.A.E., Air Force Institute of Technology, 2001

Submitted in partial fulfillment of the
requirements for the degree of

DOCTOR OF PHILOSOPHY IN ASTRONAUTICAL ENGINEERING

from the

NAVAL POSTGRADUATE SCHOOL
September 2006

Author: _____
Carl R. Hartsfield

Approved by:

_____   _____
Christopher M. Brophy   Knox T. Millsaps
Associate Professor of MAE   Professor of MAE
Dissertation Supervisor   Dissertation Committee
                                      Chairman

_____   _____
Oscar Biblarz   Garth V. Hobson
Emmeritus Professor of MAE   Professor of MAE

_____   _____
Robert G. Hutchins   Marty J. Venner
Associate Professor of ECE   Research Physical Scientist
                                      AFRL/PRSA

Approved by: _____
Anthony J. Healey, Chairman, Department of Mechanical and
Astronautical Engineering

Approved by: _____
Julie Filizetti, Associate Provost for Academic Affairs

iii

THIS PAGE INTENTIONALLY LEFT BLANK

ABSTRACT

A semi-empirical model was developed for predicting the afterburning ignition location of film cooled rocket engines. The model is based on two characteristic distances, the distance required for turbulent mixing to generate a combustible mixture with the reactive film layer and the distance traveled during the ignition delay. The mixing length is affected by the mass flow, composition of the film cooling layer and the fuel-rich air to fuel ratio required to support combustion. The ignition delay is determined by the composition directly through the auto-ignition reaction time. Both distances are affected by the velocity and temperature of the rocket core and air. This model was experimentally verified over a range of co-flow air velocities using a liquid rocket engine of approximately 440 N thrust, varying amounts of reactive film cooling and compositions of film coolant, and a co-axial annular airflow generator producing airflow at velocities up to nearly 200 m/s. Mean ignition locations experimentally observed were between 3.8 and 9.8 centimeters from the nozzle lip and varied due to the airstream velocity, and film coolant composition and mass flow. All model predictions were within the standard deviation of the experimentally observed ignition points.

THIS PAGE INTENTIONALLY LEFT BLANK

TABLE OF CONTENTS

LIST OF FIGURES

LIST OF TABLES

THIS PAGE INTENTIONALLY LEFT BLANK

LIST OF SYMBOLS

<u>English Symbols</u>

A   Arrehnius pre-exponential reaction rate constant

C_1 Ignition location model constant 1
C_2 Ignition location model constant 2

D   Constant for reaction timescale model

E   Activation energy for chemical reaction

F   Constant for reaction timescale model

GB   Gigabyte
GHz   GigaHertz

Hz   Hertz

J   Joule

K   Degrees Kelvin

L_{ign} Ignition location

M   Mach number
M_c Convective Mach number

N   Newton

Pa   Pascal (N/m^2)

Q   Thermal energy release of chemical reaction

R Universal Gas Constant

T   Temperature
T_o Wall temperature for autoignition reaction

U   Axial velocity

V   Radial velocity

a   Speed of sound

c_v	Specific heat at constant volume
f_c	Film cooling fraction
kg	kilogram
km	kilometer
l	length
lb	pound
lbf	pound-force
m	meter
$\dot{m}$	Mass flow rate
n	Order of reaction
nm	nanometers
ns	nanoseconds
r	velocity ratio
r	radius
s	density ratio
s	seconds
sec	seconds
t	film thickness

Greek Symbols

γ	Ratio of specific heats
ε	Mole or Mass Fraction for Arrehius Reaction Rates
θ	Helical pitch angle
λ	Wavelength
ρ	Density
σ	Standard Deviation
τ	Timescale
τ_i	Ignition Timescale
τ_r	Reaction Timescale

Acronyms

RP1	Rocket Propellant-1, similar to Kerosene

ACKNOWLEDGMENTS

THIS PAGE INTENTIONALLY LEFT BLANK

EXECUTIVE SUMMARY

A semi-empircal model for prediction of rocket exhaust plume afterburning ignition locations was developed and verified. Rocket exhaust plume afterburning is a combustion process taking place outside of the rocket engine nozzle and is fueled by both the exhaust core flow, which contains a significant percentage of unburned fuel products, and the film cooling layer, a layer of nearly pure fuel products used to provide a protective thermal barrier for the combustion chamber and nozzle walls. Behind the rocket engine nozzle exit plane, turbulent mixing layers combine air with the fuel-rich rocket exhaust plume to generate a combustible mixture that ignites due to hot rocket exhaust core gases, resulting in afterburning. The semi-empirical model was verified using a laboratory scale kerosene-oxygen rocket engine of about 400 Newtons thrust with an annular co-flow of air at speeds up to nearly 200 meters per second. Mean observed ignition offsets from the nozzle lip were between 3.8 and 9.8 centimeters, depending on airstream velocity and chemical composition of the film coolant. For all observed conditions, the model predictions were within the standard deviation of the mean observed ignition locations. The semi-empirical model and experimental results indicate that for the small engine used, the offset due to the distance traveled during the autoignition process was 47-89 percent of the overall ignition offset from the nozzle lip.

THIS PAGE INTENTIONALLY LEFT BLANK

I.   INTRODUCTION

A.   MOTIVATION

Understanding and accurate characterization of the physics and chemistry that give rise to thermal emissions from rocket exhaust plumes continues to be of interest to multiple government and private agencies. Afterburning processes can be a significant component of some rocket engine exhaust plume signatures. One particular area in need of better characterization is the afterburning ignition location. Currently, the methods of predicting the mixing and reaction of chemical species in the shear layer and the resultant combustion are limited, due to existing mixing models and computational power. The purpose of this research was to improve understanding of the mixing and ignition processes leading to afterburning in film-cooled liquid rocket engine exhaust plumes and develop a model to predict the location of initial afterburning ignition based on experimentally observed mixing rates and chemical timescales associated with practical fuels. Potential applications of this work include missile detection and tracking, rocket engine development, and even environmental monitoring.

Afterburning of rocket exhaust plumes occurs often due to the inherent presence of unburned fuel and fuel products in the rocket exhaust. Optimal performance of a rocket engine is defined in terms of the specific impulse or effective exhaust velocity. The maximum exhaust velocity occurs when the ratio of total temperature to the molecular weight of the exhaust products is maximized. For example, while a mixture of 8 parts oxygen to one part hydrogen, by mass, would lead to stoichiometric combustion and maximum energy release, the primary combustion product is water, which has a relatively high molecular mass, reducing the exhaust velocity. Therefore, most H_2/O_2 engines are run at between 4:1 and 6:1 mass ratios of oxygen and hydrogen, leading to a large fraction of unburned hydrogen in the exhaust, which lowers the average molecular mass of the mixture and increases the exhaust velocity. Rockets using hydrocarbon fuels exhibit a similar behavior and are run fuel-rich to increase specific impulse. The stoichiometric ratio for an RP1/Oxygen engine would be slightly over 3.0, but such engines typically run in the range of 2.2-2.4 to improve performance [1]. The fuel-rich

1

exhaust condition is further exaggerated by the use of fuel as a film coolant for the combustion chamber/nozzle walls. Fuel is used to form a cooler layer of fluid along the wall of the combustion chamber to provide a thermal barrier, increasing combustion chamber life at minimal weight. The fuel "film" flows down the chamber and nozzle walls, possibly undergoing composition changes as the bulk temperature increases, and forms a layer of nearly pure fuel products around the well-mixed core flow at the exhaust plane.

The overall flowfield is shown schematically in Figure 1. At the nozzle exit, a turbulent shear layer is formed between the rocket exhaust and the surrounding air. Air is entrained into the shear layer along with products from the fuel film layer that makes up the outer edges of the exhaust plume. As the distance downstream increases, air is continually entrained, until a combustible mixture exists. Once a combustible mixture is formed in the shear layer the ignition reaction sequence is initiated by the hot core gases. Heat is released after a short ignition delay that may represent a significant downstream distance due to the velocity of the mixture.
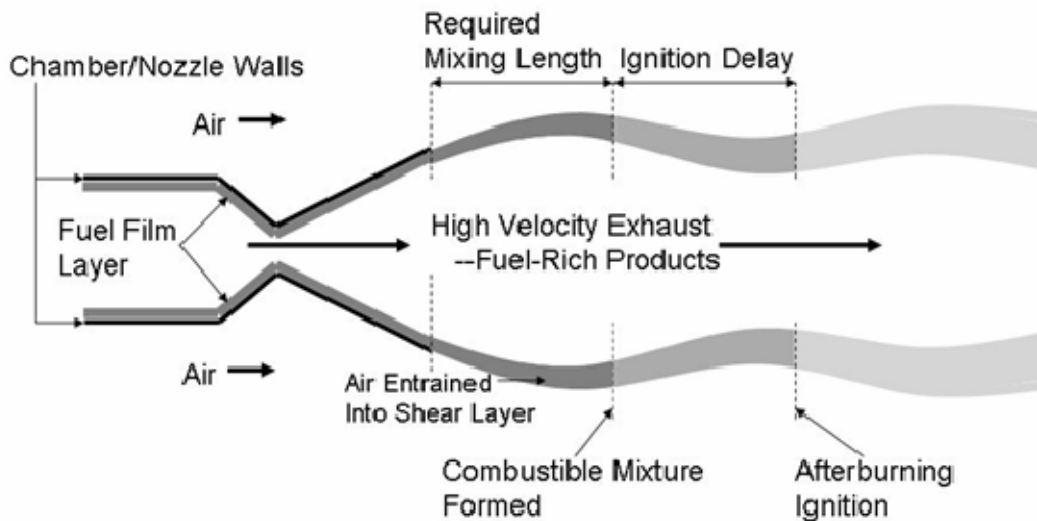
Figure 1.   Schematic of Rocket Exhaust Flowfield

B.   OBJECTIVES

The primary objective of this research was to develop a mathematical model to allow analytical prediction of afterburning ignition locations. In developing this model, it was necessary to evaluate and model the growth rate characteristics of an axisymetric, reactive shear layer. In addition to directly predicting afterburning locations, this model should provide a framework to allow simplified computational simulation of afterburning liquid rocket engine exhaust plumes. A secondary objective was to determine the radial location of afterburning ignition to evaluate whether the ignition mechanism was driven by hot particulates such as soot, or combustible gases coming into contact with, and mixing with very high temperature core exhaust products.

THIS PAGE INTENTIONALLY LEFT BLANK

II. THEORETICAL CONSIDERATIONS

A. OVERVIEW

A great deal of research has been performed on compressible shear layers, mixing of heterogeneous shear layers, and even chemical reactions in shear layers. Unfortunately, most have not been aimed at the type of shear layer found in rocket exhaust plumes. There are three common compressible shear layer problems: the supersonic combustion ramjet problem, the jet engine exhaust problem, and the rocket engine exhaust plume problem.

The flowfield inside of a Supersonic Combustion RAMjet (SCRAMjet) involves mixing a relatively slow moving fuel-rich stream with a supersonic air stream in as short a distance as possible, so that combustion occurs within the engine. Much of the SCRAMjet related work focuses on enhancing the mixing process without inducing large pressure losses.

The noise emitted from jet engine exhaust is primarily generated by the compressible shear layer between the exhaust and the ambient atmosphere. Reduction of shear layer generated noise is the primary consideration. The flow of the jet is faster than the surrounding air, and since gas turbine engines run fuel lean, the exhaust products have generally fully reacted, and chemical reactions in the exhaust plume are of little immediate importance.

The exhaust plume from a rocket engine is differentiated from the previous types by several characteristics. The core of the rocket exhaust flowfield is fuel rich, and unlike gas turbine engines, which burn fuel lean for efficiency, rocket engines burn fuel rich for performance. The core is also often significantly faster and hotter than the surrounding airflow. The velocity difference is largest early in the flight trajectory and anywhere along a rocket flight path where mixing with air is a concern, the core will be faster than the surrounding airflow. Given that rocket exhaust velocities are routinely between 2,500 m/s and 4,500 m/s, it is unlikely that the local airspeed of the rocket or missile will exceed the jet velocity, at least while there is significant air present. This is not an

exhaustive representation of every rocket or missile, but does present representative trends. Figure 2 depicts the flight path of a generic rocket, and it can be seen that at an altitude of 30 km the airspeed is expected to be about 1,100 m/s. The altitude and airspeed increase roughly linearly, so that by the time the flight velocity reaches 2,500 m/s, the rocket is effectively out of the atmosphere at 60 km altitude.
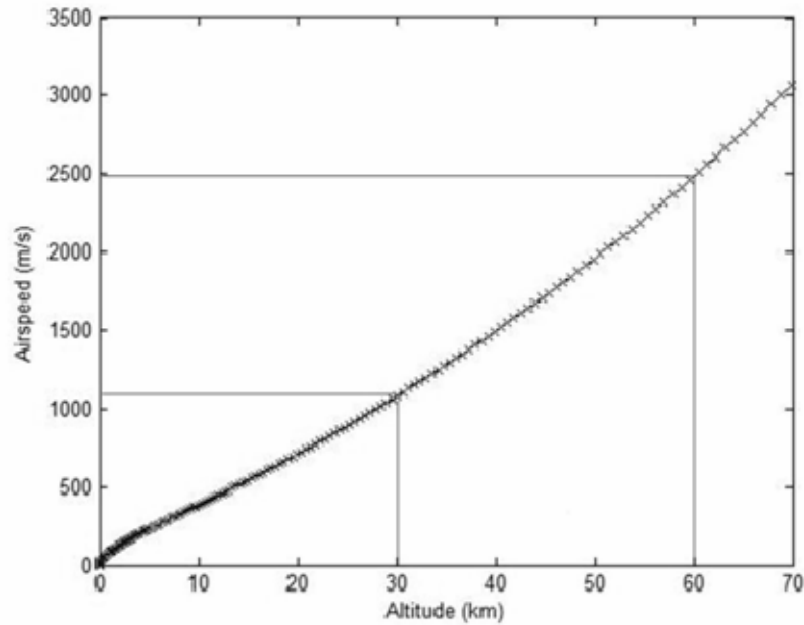
Figure 2.   Generic Rocket Flight Path: Altitude and Airspeed

Chamber pressures in excess of 50 atmospheres and combustion temperatures around 3,000-3,500 K are common. Even the most heat resistant metals and composites cannot tolerate this environment for long durations. In rocket engines, therefore, some combination of several techniques is employed to maintain structural integrity. In some cases, the nozzle, especially the nozzle throat, is manufactured from heat tolerant materials, and allowed to ablate. This technique is used mainly in solid fuel rocket motors. In liquid fuel engines, two methods of chamber and/or nozzle cooling are common. First, fuel is circulated through the nozzle and chamber walls, to convect away heat from the walls. Second, many rocket engines, employ film cooling, where relatively low temperature fuel is sprayed down the walls of the chamber to provide thermal protection to the chamber and nozzle walls. The presence of the fuel provides a thermal

6

barrier, protecting the structure from direct exposure to the combustion gases. This results in a mixture of unburned fuel and fuel components generated by chemical decomposition due to the high temperature, forming a layer around the hot core exhaust. In some cases around 10 percent, or more, of the total mass flow of the engine is in this film coolant layer. Clearly, this significantly increases the fuel mass available to initiate and sustain afterburning of the exhaust plume. An example of how the percentage of film coolant can affect the visible plume emissions is shown in Figure 3, showing images of the laboratory scale engine used in this research with kerosene film cooling percentages from 0 to 18 percent.
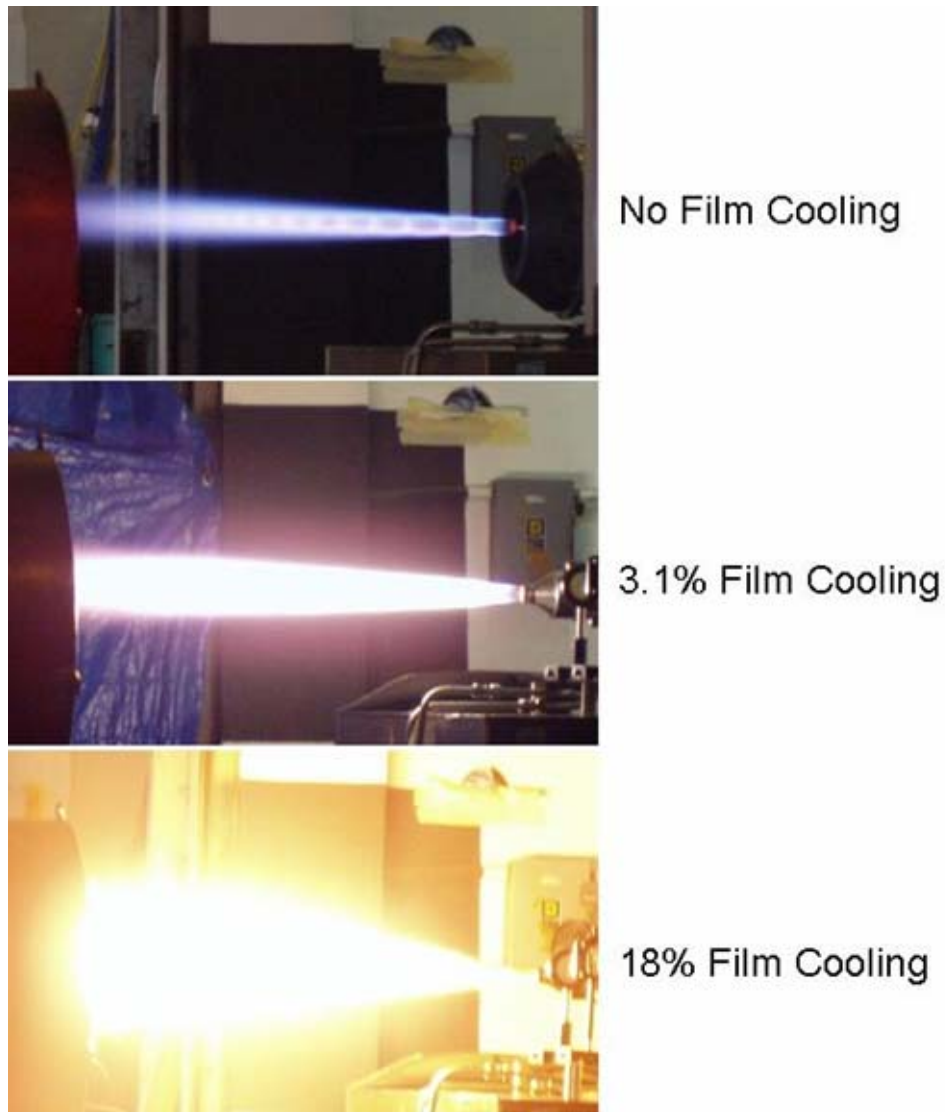
Figure 3.　Comparison of Visible Plume for Levels of Kerosene Film Cooling

7

A NASA image of a 750,000 lb thrust hydrocarbon/oxygen fueled Evolved Expendable Launch Vehicle (EELV) engine test is shown in Figure 4 [2]. The afterburning appears to visually begin about 0.25-0.5 nozzle diameters back from the nozzle lip.
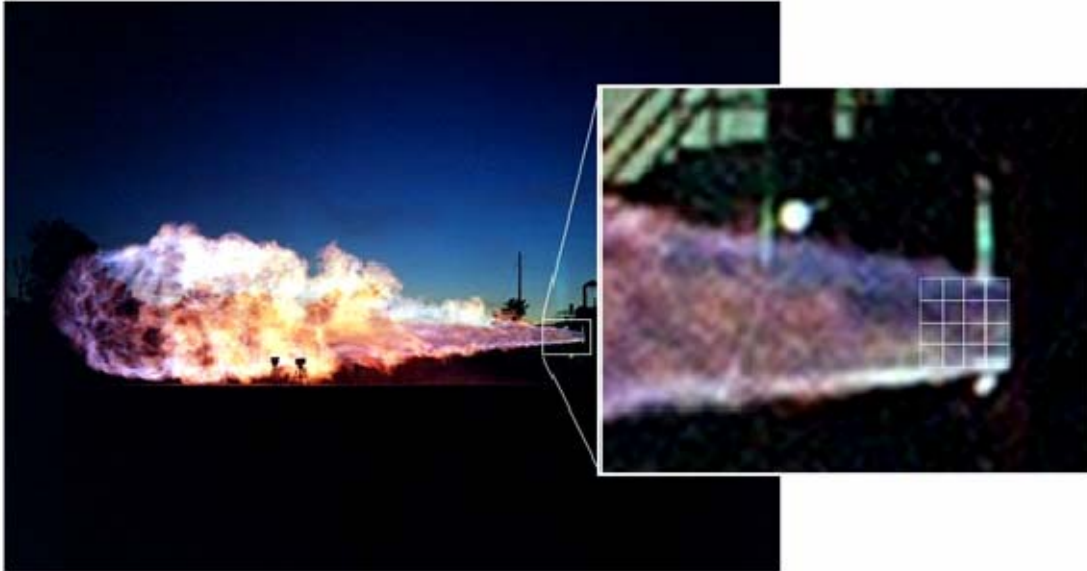
Figure 4.   NASA EELV Test-Firing: Showing Afterburning (From Ref. [2])

In spite of the differences in the details of these flows, the work on other compressible shear layers can be used to some extent in analyzing the rocket exhaust flows which are the subject of this research. The previously developed theory can be viewed in terms of the general trends of shear layer growth and the mixing rates caused by the growing shear layer. Analysis of mixing for compressible shear layers has historically been based on incompressible shear layer growth analysis, corrected for the additional effects of compressibility. This research will treat compressible shear layer growth similarly. Additional considerations for axisymetric jets and finally the problem of the three-stream, axisymetric shear layer will be developed.

B.   SHEAR LAYER GROWTH

A basic shear layer consists of two plane flows with different velocities, U_1 and U_2, and densities ρ_1 and ρ_2, which are initially separated by a partition which ends at x = 0, where the flows meet and begin to act upon each other. The general regions are shown

in Figure 5. Downstream of the partition between the streams, the flow develops into a region where the mean flow approaches similarity in terms of *y/x*. The profiles of streamwise velocity and density take the similarity forms, as shown by Brown and Roshko [3]:

$$U/U_1 = fn(\eta; r, s) \quad \rho/\rho_1 = fn(\eta; r, s)$$

$$\text{where} \tag{1}$$

$$\eta \equiv y/(x - x_o) \quad r \equiv U_2/U_1 \quad s \equiv \rho_2/\rho_1$$

The origin shift, x_o, is included to correct for what are essentially the effects of a wake behind the partition near x = 0. Due to these effects, the flow, in a strict sense, only asymptotically approaches the similarity state at very large values of x, such that $x_o/x \to 0$.
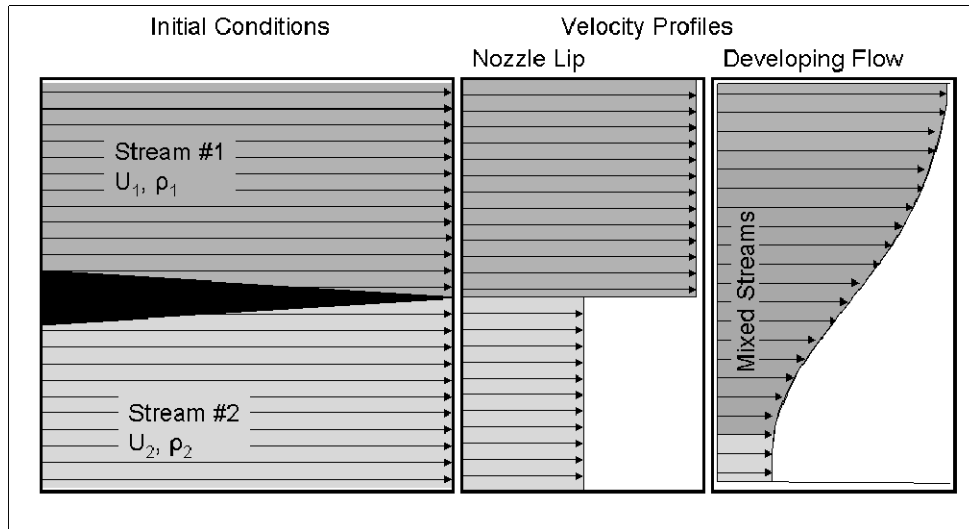
Figure 5.   Shear Layer Schematic

Each shear flow described by the relationships defined in Equation 1 spreads linearly, such that:

$$\frac{d\delta}{dx} \equiv \delta' = \frac{\delta}{x - x_o} = C \tag{2}$$

where δ symbolizes any measure of the local thickness of the mixing layer. This may be defined in a variety of ways depending on the diagnostics in use. For example, if a hot-wire probe is used, δ may be defined using the vorticity thickness, δ_ω (see below) since

9

the velocity gradient can be determined. However, a visual method, such as Schlierien or shadowgraph images, would not allow this measurement, so a δ_{vis} would be determined. The constant, C, is a function of the velocity ratios and density ratios.

$$C = C(r,s) = C\left(\frac{U_2}{U_1}, \frac{\rho_2}{\rho_1}\right) \tag{3}$$

Papamoschou and Roshko [4] proposed the following model for the mixing layer growth rate, δ'_{vis}, using the mixing layer visible on Schlieren photographs of the mixing layer as their mixing layer thickness.

$$\delta'_{vis,0} = 0.17 \frac{\Delta U}{U_c} = 0.17 \frac{\left[1 - \frac{U_2}{U_1}\right]\left[1 + \left(\frac{\rho_2}{\rho_1}\right)^{1/2}\right]}{1 + \frac{U_2}{U_1}\left(\frac{\rho_2}{\rho_1}\right)^{1/2}}$$

or $\tag{4}$

$$\delta'_{vis,0} = 0.17 \frac{\Delta U}{U_c} = 0.17 \frac{[1 - r]\left[1 + s^{1/2}\right]}{1 + r(s)^{1/2}}$$

Since the mixing layer growth is related to the kinetic energy of the two streams, the effect of density differences is less than that of velocity differences. Therefore the density ratio, s, appears only as its square root. The velocity ratio, r, is always less than 1, as the higher velocity stream is, by default, stream 1. This means that the value of the density ratio, s, may be any positive value, and is not limited to values greater or less than unity.

The relationship reflected in Equation 4 was derived using planar shear layer data. Given that the shear layers of interest in this research are not planar, but axisymetric, a modified form will be used:

10

$$\delta'_{vis,0} = 0.17 \frac{\left[1-\left(\frac{U_2}{U_1}\right)^{1/2}\right]\left[1+\left(\frac{\rho_2}{\rho_1}\right)^{1/2}\right]}{1+\left(\frac{U_2}{U_1}\right)^{1/2}\left(\frac{\rho_2}{\rho_1}\right)^{1/2}}$$

<div align="center">or</div> (5)

$$\delta'_{vis,0} = 0.17 \frac{\left[1-r^{1/2}\right]\left[1+s^{1/2}\right]}{1+r^{1/2}s^{1/2}}$$

The proposed model incorporates similar features, but the change in the geometry of the shear layer makes it reasonable to assume that the effects may be slightly different with the velocity and density ratios having greater or lesser effects than in a planar shear layer. Tennekes and Lumley [5] noted that the velocity of an axisymetric jet varies as the inverse of the axial (downstream) distance, while the velocity of a planar jet varies with the inverse of the square root of the axial position. The growth rate is related to the dissipation in the core of the rocket exhaust jet. Therefore, if the velocity of the core in a planar jet drops proportionally to $x^{-1/2}$ and the growth rate is dependent on the velocity ratio r^1, then for an axisymetric jet where the core velocity drops by x^{-1}, the growth rate should be proportional to $r^{1/2}$. The exponent applied to the velocity or velocity ratio is simply reduced by ½ in all cases. If the density ratio, s, is held constant in Equations 4 and 5, the effect of changes in velocity ratio is much stronger and the mixing rates are lower since as the mixing layer grows thicker, the momentum of the core is reduced faster. The effects of the velocity ratio exponent on the shear layer growth rate are shown in Figure 6. Nothing indicates that the effect of density is changed by the transformation from planar to axisymetric jets, so the exponent remains 0.5.
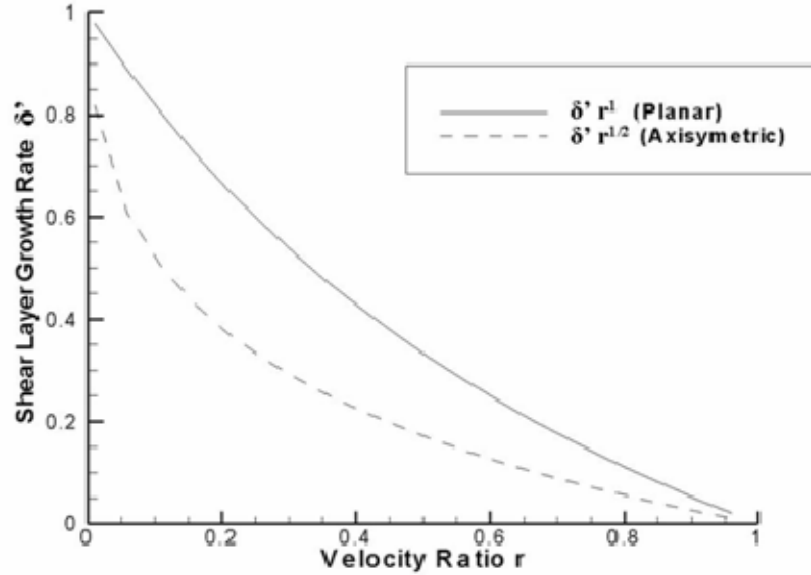
Figure 6.   Effect of Velocity Ratio Exponent on Predicted Shear Layer Growth Rates

Papamoschou and Roshko [4] have also shown that other measures of mixing layer thickness may be proportionally related to this visual thickness, such that the vorticity thickness, δ_ω, may be taken to be $0.5\delta_{vis}$, and given several potential values from 0.72 to 0.90, they assumed that the pitot thickness, δ_{pit} was 0.82 δ_{vis}. These thicknesses were defined as follows: δ_{pit} is the width of the pitot (axial velocity) profile, from 5% to 95% of the free-stream velocity differences, or, if a wake defect exists in the shear layer as often happens near the splitter, the measurement is from 95% of the velocity difference from the lower layer to the minimum velocity, to 95% of the velocity difference from the upper layer to the minimum velocity. The vorticity thickness δ_ω is defined as:

$$\delta_\omega = \frac{U_1 - U_2}{\left(\partial U / \partial y\right)_{max}} \tag{6}$$

This clearly results in a thickness calculation much smaller than the actual mixing layer thickness, but provides a reasonable point of comparison that can be calculated for many methods of flow measurement and is independent of any assumed velocity profile.

12

This research used a δ_{vis} based on the observed thickness of the soot layer generated by by reactions inside the rocket engine and/or in the exhaust plume.

C.   TWO-STREAM MIXING

The growth of mixing layers inherently requires the entrainment of additional mass into the mixing layer. If the mixing layer is treated as a stream moving at the convection velocity U_c, having average density ρ_c, and a thickness of δ_i, represented by segment AC in Figure 7, at a distance, l, the thickness will have grown by $\delta'l$, represented by segment BD in Figure 7. The shear layer mass flows can then be given as:

$$\dot{m}_{AC} = \delta_{AC}U_c\rho_c \quad \dot{m}_{BD} = \left(\delta_{AC} + \delta'l\right)U_c\rho_c$$
$$\dot{m}_{ent} = \dot{m}_{BD} - \dot{m}_{AC} = \delta'lU_c\rho_c$$
$$or$$
$$\dot{m}'_{ent} = \delta'U_c\rho_c$$

(7)

This gives a total entrained mass flow, but not the proportion of the mass entrained from each side of the shear layer. For the purposes of this analysis, it is assumed that half comes from each stream. However, the density of the mixing layer is dependent on the exact composition of the mixing layer at a given point, which will be a combination of the core, film, and air. This calculation is highly dependent on the assumed proportions of the mass flow entrained from each side of the shear layer, as the assumed proportion determines the density changes, resulting in a non-linear dependency. However, by looking at the other facet of the mixing process, instead of calculating the entrainment of air into the mixing layer, the entrainment of air from the airstream can be calculated without knowledge of the composition of the mixing layer. In addition to simplifying the calculations, this reduces the dependency of the calculated entrainment rates on the assumed proportions of the mass entrained from each side of the mass flow to a linear dependency. Therefore, the air entrainment rate will be based on the values of the co-flowing air, rather than values dependent on the shear layer composition that changes continuously with axial location. Using the density of air, and substituting a velocity based on the difference between the convective velocity of the shear layer, which is the velocity at which vortices within the shear layer propagate, and the velocity of the airstream, an axial length scale of mixing can be determined. The length scale required to

13

entrain sufficient air into a reactive film coolant layer to produce a combustible mixture can be calculated by the following formula:

$$\dot{m}_{film}\left(\frac{Air}{Fuel}\right)_{req'd} = \dot{m}_{air_{ent}} = \frac{1}{2}\dot{m}'_{ent} = \frac{1}{2}\delta'|U_c - U_{air}|\rho_{air}l_{mix}(2\pi r_{mean})$$

$$l_{mix} = \frac{2\dot{m}_{film}\left(\dfrac{Air}{Fuel}\right)_{req'd}}{\delta'|U_c - U_{air}|\rho_{air}(2\pi r_{mean})} \tag{8}$$
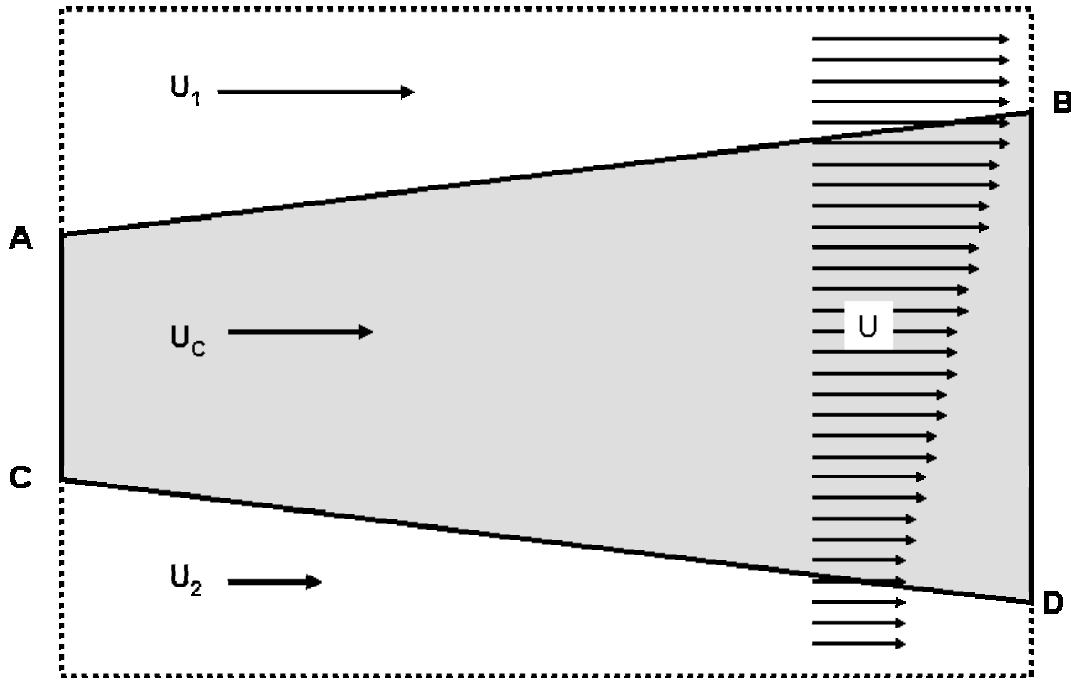
Figure 7.   Shear Flow Entrainment Schematic

Equation 8 yields a semi-empirical model of the distance from the nozzle lip required to mix sufficient air into the fuel-film layer to produce a combustible mixture in the shear layer. The mean radius of the shear layer has been incorporated into Equation 8 and the mean radius is taken as the exit radius of the rocket exhaust nozzle. However, for significantly under-expanded flows, where the exit pressure is much greater than the ambient pressure, the mean radius of the plume shear layer could be significantly larger than the nozzle exit radius, and the entrainment rate would therefore be increased. The shear layer growth rate, δ' is not specified, and can vary significantly. Depending on which δ' is specified, the length scale multiple will vary similarly, and unique

14

coefficients would correct for the choice of shear layer thickness measurement. However, for this research, δ'_{vis} will be used exclusively. Since δ'_{vis} is the largest growth rate, the constant multipliers will be minimized. The visible shear layer thickness is the largest shear layer thickness outlined and thus will have the fastest growth rates and shortest length scales.

The air/fuel mass ratio required for combustion of the film coolant with air is also included in the length scale relationship in Equation 8 and should be represented by the rich combustion limit. Using data from Glassman [6] and the Cal Tech Explosion Dynamics Lab Webpage [7], the rich combustion limits have been calculated for a number of fuels/film coolants, and can be found in Table 1.

Table 1.   Rich Combustion Limit Air/Fuel Ratios for Potential Fuels/Film Coolants

Fuel	Formula	Molar Mass	Rich Air/Fuel Limit (by Volume)	Rich Air/Fuel Limit (by mass)
Ethanol	C_2H_5OH	46	0.190	2.669
Hydrogen	H_2	2	0.750	4.800
Benzene	C_6H_6	78	0.079	4.300
Acetylene	C_2H_2	26	1.000	0
Ethylene	C_2H_4	28	0.360	1.829
JP-4	$CH_{1.97}$	130	0.080	2.548
Kerosene	$CH_{1.953}$	175	0.048	3.264

D.   COMPRESSIBILITY CONSIDERATIONS

Compressibility effects tend to suppress shear layer growth and mixing. The Mach number of concern for compressible shear layers is the Mach number of the flows relative to the mixing vortices. The vortices between the two streams convect downstream at a velocity between those of the outer and inner streams. The Mach number governing the compressibility effects on mixing is called the convective Mach number, designated M_c. In general, there are two convective Mach numbers for each mixing layer, one relative to stream one and one relative to stream two, and are represented by M_{c1} and M_{c2} respectively. Papamoschou and Roshko [4] related the convective Mach numbers to the flow parameters as follows:

$$M_{c_1} = \frac{U_1 - U_c}{a_1} \quad M_{c_2} = \frac{U_c - U_2}{a_2} \tag{9}$$

Equation 9 reveals that it is clearly possible to have two supersonic streams, with negligible convective Mach numbers affecting the mixing between them. Papamoschou and Roshko also related the two convective Mach numbers to each other through an implied equality of total pressure relative to the mixing structure. Using isentropic relations, they established the following relationship between the two convective Mach numbers:

$$\left(1 + \frac{\gamma_1 - 1}{2} M_{c_1}^{\ 2}\right)^{\frac{\gamma_1}{\gamma_1 - 1}} = \left(1 + \frac{\gamma_2 - 1}{2} M_{c_2}^{\ 2}\right)^{\frac{\gamma_2}{\gamma_2 - 1}} \tag{10}$$

They detail further simplifications for low values of M_{c1} and M_{c2} and nearly identical ratios of specific heats, but these do not necessarily apply to the present work. The flows being studied in the present research may exhibit relatively large convective Mach numbers and very different chemical species due to the air, film coolant vapor, and fuel-rich combustion products. Therefore, those simplifications will not be presented. A recursive arrangement can be established from Equations (9) and (10) to determine a value of convective velocity, U_c, which fulfills the relationship in Equation (10). Equation (10) shows that, if the ratio of specific heats, γ, is different, then the convective Mach numbers will be different for the two streams. However, given the potential range of γ, from approximately 1.1 to 1.66, a large difference in the two convective Mach numbers cannot be supported. If the second stream is fixed as air ($\gamma = 1.4$) the limits of the relative difference in the convective Mach numbers are as shown in Figure 8.
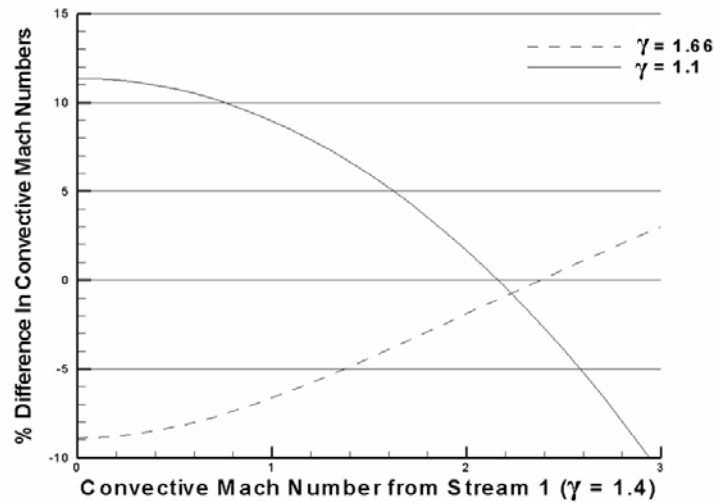
Figure 8.   Variation in Convective Mach Number Due to Differences in the Ratio of Specific Heats or γ

Figure 8 shows that, across a very wide range of convective Mach numbers and γ, there is relatively little difference in the two convective Mach numbers, such that it will make little difference which side is selected to determine the magnitude of the compressibility effects on mixing and shear layer growth, and in fact an average will be used.

Having established the measure of compressibility that applies to the problem, the effects of that compressibility must be evaluated. Increasing compressibility tends to suppress mixing and growth, although the vast majority of the suppression takes place prior to achieving supersonic convective Mach numbers [4, 8, 9]. In fact, the mixing or growth rate is nearly constant above a convective Mach number of about 0.7. Bogdanoff [8] proposed that this was due to mixing modes oriented at an angle to the mean flow, which results in an effectively reduced convective Mach number driving the flow development. It is apparent from the data that the angle sets itself such that the effective convective Mach number, defined as $M^+ = M_c \cos\theta$, remains subsonic. The swept

vortex structure prevents a loss of energy in shock waves leading into the turbulent vortices [10]. This is analogous to the wing sweep of high speed aircraft being selected to reduce the formation of shock waves on the wing.

The convective Mach numbers are relatively large in the case of the present research. The rocket exhaust velocities are approximately 2,400-2,700 m/s with core temperatures around 1,800 K, while the air velocities are limited to a maximum of about 200 m/s with temperatures around 290 K. The result is a range of convective Mach numbers of 1.7 to 1.9 for the flows generated experimentally. These values are well into the region for shear layer growth and mixing rates that are nearly independent of convective Mach number. The shear layer condition for the exhaust of a rocket or missile in powered flight is continuously changing. The rocket exhaust velocity is often nearly constant, while the airspeed increases. The constant exhaust jet velocity and increasing airspeed result in an increasing convection velocity, U_c, but a decreasing convective Mach number, as shown in Equation 9. The condition of decreasing convective Mach number with increasing convective velocity is somewhat counter-intuitive, but as the flight speed increases, the convective Mach number decreases, until the flight speed matches the exhaust speed.

Figure 9, taken from Nixon and Keefe [11] and presenting data from Bogdanoff [8], shows the limiting effect of compressibility on mixing layer growth. In addition to the relationship outlined by Nixon and Keefe, Murakami and Papamoshou [12] provide a simple, empirical fit to the data as:

$$\frac{\delta'}{\delta'_{inc}} = 0.23 + 0.77 \exp\left(-3.5 M_c^2\right) \tag{11}$$

Equation (11) defines the relationship between the actual mixing layer growth rate, δ', and the mixing layer growth rate for an equivalent incompressible flow, δ'_{inc}. The growth rate for an incompressible flow can be either a calculated or observed quantity based on equivalent velocity and density ratios for the two streams, but only for low values of convective Mach number.

18

The data contained in Figure 9 shows the constants contained in Equation 11 will lead to values considerably below those shown from the experimental data taken from Schadow, et al. [13]. The data provided by Schadow has a δ' / δ'_{inc} value of approximately 0.3 at a M_c of about 2.2. If the constants are modified such that the δ' / δ'_{inc} asymptotically approaches 0.3, rather than 0.23, the Schadow data is better matched and better reflects the effects of compressibility on axisymetric shear layers. For this, Equation 11 becomes:

$$\frac{\delta'}{\delta'_{inc}} = 0.3 + 0.7 \exp\left(-3.5 M_c^2\right) \tag{12}$$
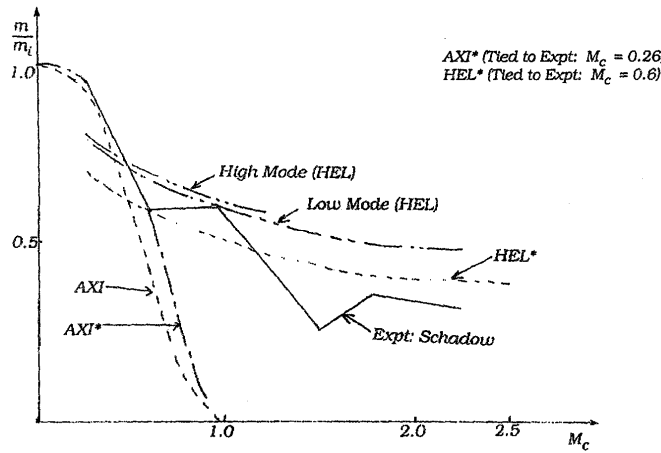
Figure 9.　Mixing Ratio and Convective Mach Number in Circular Jets: Comparison Between Experiment and Theory (From Ref. [9])

E.　OTHER COMPRESSIBILITY CONSIDERATIONS FOR AXISYMMETRIC JETS

The mixing flow around an axisymetric jet is governed [9] by the Prandtl-Glauert Equation:

$$\beta^2 \phi_{xx} + \phi_{rr} + \frac{1}{r}\phi_r + \frac{1}{r^2}\phi_{\theta\theta} = 0 \tag{13}$$

Where θ is the azimuth angle, x is an axial distance, r is radius, and φ is the perturbation velocity potential. The last element, β, is given by:

$$\beta^2 = 1 - M_c^2 \tag{14}$$

19

There are two possibilities for mixing modes about axisymetric jets. The first is purely axisymmetric vortical structure. Purely axisymmetric structure would imply that the azimuthal variations are zero, and leads to the following equations for the axial and radial induced velocities [9]:

$$V_x = \frac{\Gamma}{4\pi r_o \beta} \int_0^{2\pi} \frac{\left[1 - r\cos(\theta - \theta')\right]}{\left[\frac{x^2}{\beta^2} + r^2 + 1 - 2r\cos(\theta - \theta')\right]^{3/2}} d\theta'$$

$$V_r = \frac{-\Gamma}{4\pi r_o \beta} \int_0^{2\pi} \frac{\left[x\cos(\theta - \theta')\right]}{\left[\frac{x^2}{\beta^2} + r^2 + 1 - 2r\cos(\theta - \theta')\right]^{3/2}} d\theta'$$

(15)

Where Γ is the vortex strength and r is the radius, normalized by r_o. Clearly there is a major problem with Equations 13-15 as $M_c \rightarrow 1$, since division by zero will occur. Avoiding division by zero leads to the possibility of a helical vortex structure. For the helical vortex structure, β is redefined as follows:

$$\beta^2 = 1 - M_c^2 \cos^2 \theta_s$$

(16)

Since the previous assumption of no azimuthal variation is invalid for the helical vortex structure, the axial, radial and azimuthal velocities are given by:

$$V_x = \frac{\Gamma\left(1 + \mu^2\right)^{\frac{1}{2}}}{4\pi r_o} \int_0^{2\pi} \frac{\left[1 - r\cos(\theta - \theta')\right]}{\left[\frac{(x - \theta'\mu)^2}{\beta^2} + r^2 + 1 - 2r\cos(\theta - \theta')\right]^{3/2}} d\theta'$$

$$V_r = \frac{-\Gamma\left(1 + \mu^2\right)^{\frac{1}{2}}}{4\pi r_o} \int_0^{2\pi} \frac{\left[\frac{(x - \theta'\mu)}{\beta}\cos(\theta - \theta') + \mu\sin(\theta' - \theta)\right]}{\left[\frac{(x - \theta'\mu)^2}{\beta^2} + r^2 + 1 - 2r\cos(\theta - \theta')\right]^{3/2}} d\theta' \qquad (17)$$

$$V_\theta = \frac{\Gamma\left(1 + \mu^2\right)^{\frac{1}{2}}}{4\pi r_o} \int_0^{2\pi} \frac{\left[-\frac{(x - \theta'\mu)}{\beta}\sin(\theta - \theta') - \mu r + \mu\cos(\theta' - \theta)\right]}{\left[\frac{(x - \theta'\mu)^2}{\beta^2} + r^2 + 1 - 2r\cos(\theta - \theta')\right]^{3/2}} d\theta'$$

20

And μ is given by:

$$\mu = \tan\theta_s \tag{18}$$

Equations (16), (17) and (18) depend on the pitch angle of the helix, θ_s, which remains unknown. Keefe and Nixon [9], using data reported by Seiner [14] determined three variations of μ, corresponding with multiple wavelengths of turbulence in the shear layer. By estimating the jet Mach number in the data to be twice the convective Mach number, and relating the helical pitch to the wavelength of the generated sound by:

$$\mu = \tan\theta_s = \frac{\lambda}{2\pi r_o} \tag{19}$$

Keefe and Nixon were able to fit linear functions to these data to obtain:

$$\mu = \begin{cases} \dfrac{1}{\pi}\left(1+4.4M_c\right) & \text{"low mode"} \\[2mm] \dfrac{1}{\pi}\left(1.5+5.5M_c\right) & \text{"intermediate mode"} \\[2mm] \dfrac{1}{\pi}\left(1.75+6.2M_c\right) & \text{"high mode"} \end{cases} \tag{20}$$

Interestingly, for each of these functions, there exists a limiting β, as follows:

$$\begin{aligned} \min\beta^2 &= Lim_{M_c\to\infty}\left\{1-M_c^2\cos^2\left[\tan^{-1}\left(\frac{a+bM_c}{\pi}\right)\right]\right\} \\[2mm] \min\beta^2 &= Lim_{M_c\to\infty}\left\{1-\frac{\pi^2 M_c^2}{b^2 M_c^2 + 2abM_c + a^2 + \pi^2}\right\} \\[2mm] \min\beta^2 &= Lim_{M_c\to\infty}\left\{1-\frac{\pi^2}{b^2 + \dfrac{2ab}{M_c}\!\!\!\diagup + \dfrac{a^2}{M_c^2}\!\!\!\diagup + \dfrac{\pi^2}{M_c^2}\!\!\!\diagup}\right\} \\[2mm] \min\beta^2 &= 1-\frac{\pi^2}{b^2} = \begin{cases} 0.490 & \text{"low mode"} \\ 0.674 & \text{"intermediate mode"} \\ 0.743 & \text{"high mode"} \end{cases} \end{aligned} \tag{21}$$

A limiting β implies that the limiting convective Mach number normal to the vortices is about 0.71. This corresponds well to the general leveling of the mixing layer growth beyond a convective Mach number of 0.7 in these data presented by multiple researchers [4, 8, 9, 13].

F. CONSIDERATIONS FOR THREE-STREAM MIXING

One of the difficulties of the current three-stream mixing problem is that the film layer inside or outside the rocket engine cannot be precisely measured due to the uncertainty in the composition of the film layer exiting the nozzle. A petroleum based hydrocarbon, such as kerosene or RP-1, will undergo compositional changes and "crack" into various fuel constituents as the fuel film is heated and gradually mixes with the core flow gases as the flow develops inside the engine and nozzle. Additionally, the degree of fuel decomposition is dependent on the temperature history of the film coolant and does occur at some finite rate. In the case of the film cooling layer, since the velocities inside the film layer are unknown, the residence times can only be estimated, as well as the maximum temperatures reached. One of the contributing reasons that the velocities are unknown is that the location of any phase change from liquid to vapor is unknown. Additionally, for most liquid hydrocarbon fuels, the conditions within a rocket engine place the mixtures at a supercritical state, increasing the difficulty of predicting the mixing process within the engine.

The resulting film layer makes up a significant portion of the rocket nozzle boundary layer. The core flow and fuel film layers cannot effectively be separated, and therefore, a bulk velocity, ratio of specific heats, temperature, etc, will be assumed. Since very little is known about the actual fuel film layer, assumptions must be based on the core flow, which can be calculated. Composition, velocity, temperature, and pressure can be calculated using either the area ratio of the nozzle or the pressure ratio from combustion chamber to ambient, for both frozen expansion or complete equilibrium flow. The bulk velocity of the film layer can be assumed to be near, but less than, the core velocity. Since the film layer effectively makes up the boundary layer region of the overall flowfield, the average fuel film velocity must be near the core velocity. The temperature of the rocket core flow at the nozzle exit can also be determined, based on

similar calculations. The temperature and ratio of specific heats can be assumed to be similar to the core. The ratio of specific heats will be similar due to the presence of large mass fractions of polyatomic hydrocarbon fuel component molecules holding the ratio of specific heats down towards 1.1-1.2. The ratio of specific heats would be expected to be, if anything, slightly lower, as the fuel products in the film layer will likely be made up of larger, more complex molecules than the combustion products, which will have large portions of water, carbon monoxide and carbon dioxide. The ratio of specific heats is reduced as the number of atoms in the molecule increases and as the temperature increases. For example, monatomic gases have a ratio of specific heats of about 1.66, diatomic gases have a ratio of specific heats around 1.4, and more complex polyatomic molecules tend towards a ratio of specific heats of 1.1. In addition, as shown in Figure 8, the exact value of the ratio of specific heats has limited impact on the calculation of convective Mach number, and even less on the final shear layer growth rates. The temperature will be similar due to the viscous recovery in the boundary layer, that will keep the film layer temperature closer to the stagnation temperature of the film layer, and slightly reduced expansion of the film layer, relative to the core, caused by a slightly lower ratio of specific heats. The assumption that the conditions of the core apply to the film layer permits estimates of velocity and density ratios between the streams, and estimates of the mixing layer growth rates. Overall, the problem will be treated much like two-stream mixing, except for the use of the mass flow rates for the third stream of film coolant. Since the film and core velocities are assumed to be nearly the same, any mixing effects at the film/core interface can essentially be ignored. Referring to Equation 5, as the velocity ratio approaches unity, the mixing rapidly approaches zero. Since the velocity ratio is very close to unity, as is the density ratio, the mixing layer growth rate will be nearly zero between the core and film layer. The mixing layer between the core and film will be relatively quickly absorbed by the mixing layer with the surrounding airflow, whose growth is driven by much larger velocity and density differences.

G.   CHEMICAL REACTION DISTANCE

The distance involved in initiating or completing the reaction is not considered in most combustion problems. However, in this case, combustion takes place in a fuel/air mixture moving at several hundreds of meters per second, implying that even very short

times, on the order of 10^{-5}-10^{-4} seconds can result in downstream distances on the order of centimeters, in addition to the distance required to entrain sufficient air to produce a combustible mixture. While this may not be large in terms of full scale rockets, in terms of a laboratory scale rocket, a few centimeters may make up a good portion of the afterburning ignition standoff distance. Therefore, that distance must be quantified.

According to Glassman [15], a time scale for thermal spontaneous ignition can be estimated as:

$$\tau_i = \tau_r \left(\frac{c_v R T_o^2}{QE} \right)$$

(22)

where τ_i is the ignition timescale, and τ_r is the reaction timescale. The hot wall temperature used to ignite the mixture is T_o, R is the universal gas constant, c_v is the specific heat at constant volume for the mixture, Q is the thermal energy release of the reaction and E is the activation energy for the reaction. Glassman neglects the effects of pressure and mole concentration, showing that those effects have a minimal effect on the timescale calculation. The reaction timescale, τ_r, can be estimated by the following [15]:

$$\tau_r = \frac{\rho}{\left[\rho^n \varepsilon^n A e^{\left(\frac{-E}{RT_o} \right)} \right]}$$

(23)

There are three new constants: A is the Arrhenius pre-exponential reaction rate constant for the specific reaction, ε is the mole or mass fraction of the species, and n is the order of the reaction, given as an integer. These two equations can be combined to obtain:

$$\tau_i = \frac{\rho}{\left[\rho^n \varepsilon^n A e^{\left(\frac{-E}{RT_o} \right)} \right]} \left(\frac{c_v R T_o^2}{QE} \right)$$

or rearranging: (24)

$$\tau_i = \frac{\rho c_v R}{\rho^n \varepsilon^n A Q E} \left(T_o^2 e^{\left(\frac{E}{RT_o} \right)} \right)$$

24

One significant difficulty in using these equations is the selection of the various constants, especially in the case of kerosene or other petroleum based fuels. Since the fuels are a mixture of various hydrocarbon components, rather than being composed of a single petroleum fraction, it is difficult to represent its combustion as a single step. In reaction modeling, multiple simple reactions are assumed, and rates determined using the specific set of constants for each individual reaction. The use of all the individual rates then allows a macroscopic prediction of the overall combustion process to be determined, for the given initial conditions. There are generally around 80-100 reactions for a relatively complete hydrocarbon-air combustion model. This complicates the determination of the ignition delay time. A reaction timescale could be determined for each potential reaction, and then the shortest, average, or primary initiating reaction timescale could be selected. However, this does not take into account the uncertainty about the composition of the film layer at the nozzle exit. Since the exact composition is unknown, this approach would be highly questionable. An empirical fit to data for the film coolant as injected will be used to capture the gross behavior. The approach uses experimental autoignition data which should inherently account for the breakdown in petroleum based fuels with temperature to some degree, as the high temperatures used for self-ignition testing would have produced some of the cracking and decomposition expected in the rocket chamber and nozzle. By assuming dependency only on the temperature, and holding all other values constant, a dependency on temperature for the ignition timescale can be obtained:

$$\tau_i = DT_o^2 e^{\left(\frac{F}{T_o}\right)} \tag{25}$$

Using ignition time data from Glassman [16], the constants, D and F, for carbon monoxide, ethanol, hydrogen, and kerosene can be estimated as shown in Table 2.

Table 2.   Ignition Time Estimate Constants by Reactant

Carbon Monoxide	
D	$2.30 \cdot 10^{-21} \dfrac{s}{K^2}$
F	23003.77 K
Ethanol	
D	$2.00 \cdot 10^{-15} \dfrac{s}{K^2}$
F	13455.24 K
Hydrogen	
D	$4.89 \cdot 10^{-19} \dfrac{s}{K^2}$
F	15506.77 K
Kerosene	
D	$5.77 \cdot 10^{-16} \dfrac{s}{K^2}$
F	14341.03 K

These values lead to film ignition timescales of the order 10^{-5} seconds for temperatures near the rocket core temperature. The values also produce monotonically decreasing ignition times for temperatures between 500K and 3000K. Autoignition experiments used a controlled wall temperature to provide a heat source to ignite the fuel/air mixture. In the plume, the hot rocket exhaust core will provide the heat source, and the core temperature will be substituted for the wall temperature. For ethanol, assuming a core/wall temperature of 1,800 K, about the nozzle exit temperature of the exhaust plume core, leads to an ignition timescale of 1.14×10^{-5} second, while for kerosene the same conditions lead to an ignition timescale of 5.39×10^{-6} second. Using a predicted convective velocity of around 500 m/s, the ignition delay component of the offset from the nozzle lip would have length scales are on the order of 2-6 mm. Actual ignition delay distance components will be relatively small multiples of these distances and, while significant from the point of view of this research, would be less significant on a full scale rocket engine, where a few millimeters or centimeters would be lost in the scale of the problem, as the distance component due to mixing would be much larger. In contrast, the distances for the core constituents, carbon monoxide and hydrogen are much smaller. The timescale for either is on the order of 10^{-9} seconds, for 1,800 K wall temperatures,

8.73x10^{-9} s for hydrogen, 2.65x10^{-9} s for carbon monoxide, leading to length scales on the order of micrometers, which are negligible from the point of view of this research.

H. RELATIONSHIP OF EXPERIMENTAL CONDITIONS TO FLIGHT CONDITIONS

The applicability of this work to many regions of practical rocket flight may be questioned, since most rocket powered vehicles accelerate to supersonic velocities early in their flight profiles. The altitude and airspeed for a generic missile in ballistic flight was shown in Figure 2. The airspeeds for the generic model are supersonic at altitudes over about 7-8 km. However, the local conditions experienced by the exhaust plume near the nozzle will be subsonic for most vehicles, due to presence of a bow-shock upstream of the nozzle exit plane. Figure 10 shows local Mach number for an inviscid computational fluid dynamic simulation of the steady flow around a generic rocket flying at 500 m/s, or about Mach 1.6, at approximately 16 km altitude. There are significant regions of subsonic flow around the rocket, first behind the bow-shock on the nose and second, around the nozzle skirt, leading into the exhaust plume. Due to the effect of the highly underexpanded rocket plume, the plume expands significantly after the nozzle exit. This expansion of the plume is accompanied by another bow shock ahead of the exhaust plume. The bow shock ahead of the plume leads to largely subsonic flow in the regions around the forward end of the exhaust plume. The simulated vehicle is 12 m long with a 1 m diameter, the half angle of the nosecone is approximately 30˚, with a 0.15 m radius of curvature on the tip. This geometry was selected to approximate the primary characteristics of a number of small sounding rockets.
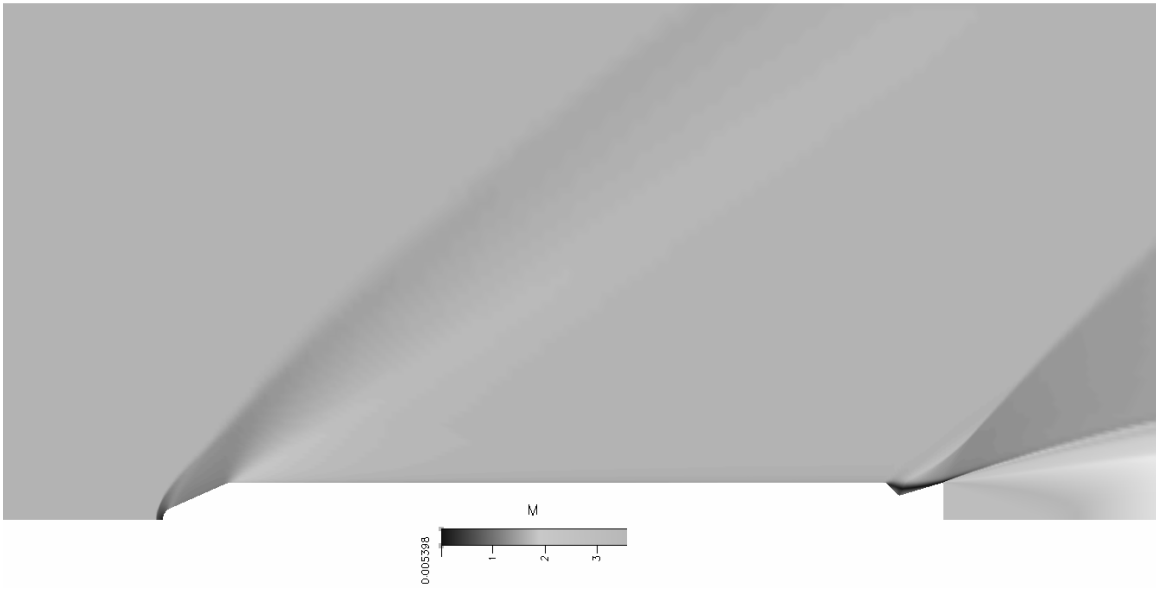
Figure 10.   Inviscid Flowfield Around Generic Rocket (Mach Number Shown)

III.   EXPERIMENTAL SET UP

A.   ROCKET ENGINE CONFIGURATION

A water-cooled, liquid rocket engine was used for the test program and produced approximately 100 lbf (445 N). Liquid film cooling could be injected along the combustor axis, but from a separate pressurized vessel so that the film coolant could be different from the fuel used for combustion. The engine was designed to fit inside an airflow assembly, leading to a relatively long, narrow combustion chamber and nozzle. The engine was modular, made up of an injector head and housing, three combustion chamber sections, a film cooling injection ring, and a nozzle assembly. Detailed drawings of all the components can be found in Appendix C. External and internal views of the rocket engine can be found in Figures 11 and 12.

Figure 11.   Rocket Engine Assembly

Figure 12.   Rocket Engine Assembly Cutaway

1.   Injector Head and Housing

The uni-element injector consisted of an axial jet of oxygen with three small fuel ports that allowed the fuel to be tangentially injected upstream of the injector exit. The design had several advantages. The injector could be throttled over a very wide range of oxidizer/fuel (O/F) ratios and was very durable i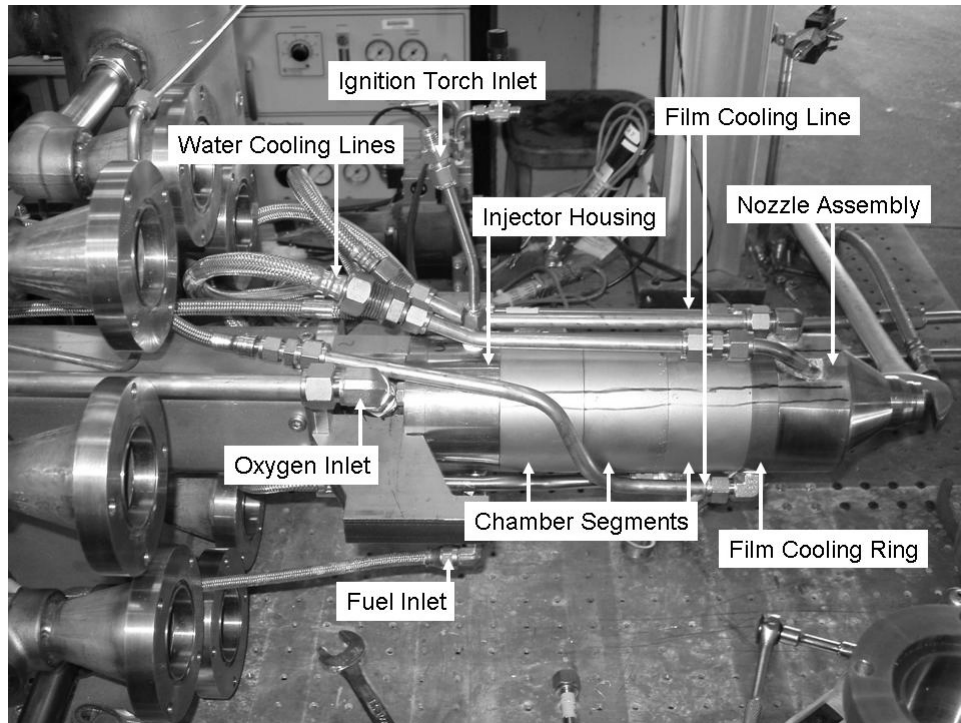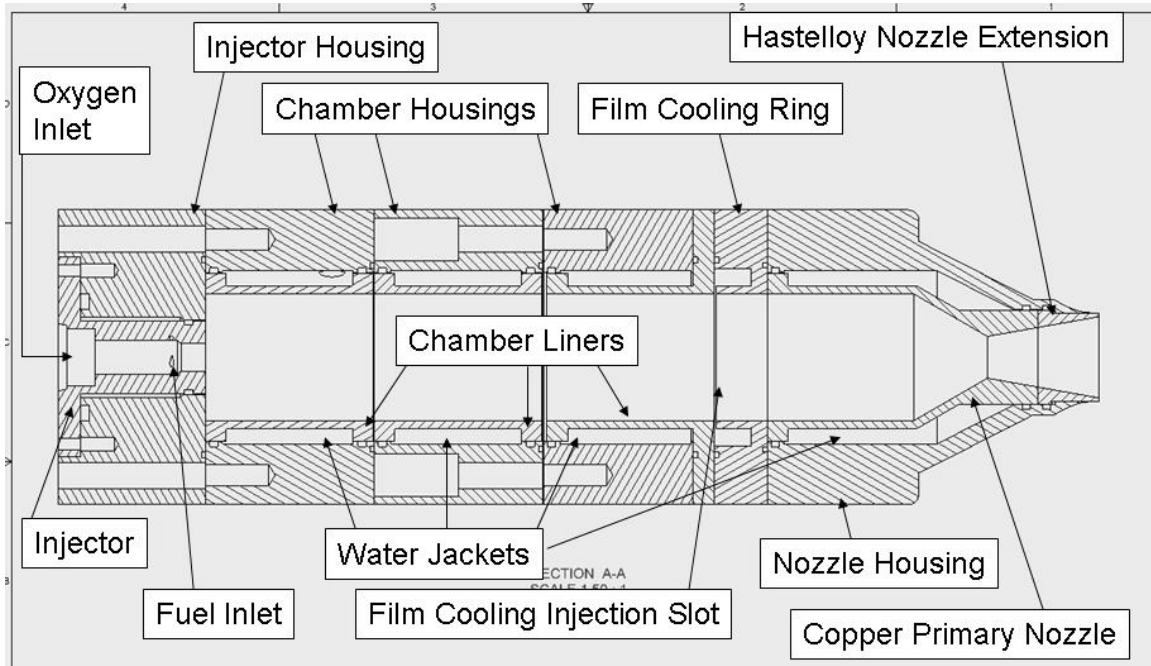n operation. Two injectors were used over the course of this research. The first was made of brass for higher thermal conductivity and improved tolerance of fuel-lean conditions. However, this injector heated the o-ring seals between the injector and injector housing significantly, so a second injector was manufactured from Hastelloy X, a high nickel super-alloy. The injectors demonstrated negligible performance differences, but the reduced thermal conductivity increased the lifespan of the fuel injector o-rings. The injector housing was made of stainless steel and contained the fittings for the fuel inlet as well as the hydrogen/oxygen ignition torch, used to ignite the kerosene/oxygen mixture in the rocket.

2.   Combustion Chamber Segments

The first two combustion chamber sections were identical, and consisted of a stainless steel housing and copper liner. The housing provided a structural housing for the water coolant flow path and incorporated the cooling water fittings. The third segment aft

30

of the injector was of similar construction, but the copper liner incorporated a large flange face which mated to the film cooling injector ring to provide dimensional stability for the film cooling injection slot.

3. Film Cooling Injection Ring

The film-cooling injection ring was made of oxygen-free copper alloy C10100 for high thermal conductivity and had four film coolant inlets, all feeding tangentially into a deep recess cut from one face of the ring. The inner wall was cut back slightly, so that when the film cooling ring was assembled to the upstream combustion chamber segment, a small slot existed for the film coolant to enter the combustion chamber. The relatively large volume of the recess and the tangential entry of the coolant to the recess, promoted a uniform radial coolant injection to the combustion chamber.

4. Nozzle Assembly

The nozzle assembly consisted of a stainless steel outer housing, which incorporated cooling water inlets. A water-cooled copper liner included additional combustion chamber length, the converging portion of the nozzle and approximately 45% of the diverging portion of the nozzle. A Hastelloy X nozzle segment completed the diverging portion of the nozzle. The Hastelloy segment was required since the airflow was delivered nearly parallel to the rocket exhaust flow, which did not leave room for water cooling jackets near the end of the nozzle. The Hastelloy nozzle extension was only cooled through conduction with adjacent hardware and radiation.

B. AIRFLOW ASSEMBLY

The airflow assembly, shown in Figures 13 to 16, was installed around the rocket engine and provided radially symmetric airflow using as little axial distance as possible. The air supply system, shown in Figure 13, was capable of delivering flow rates up to 4.5 kg/s (10 lbm/s). A metering choke was used to determine the overall air mass flow rate, and a series of converging/diverging nozzles were used to reduce the total pressure. The air then entered a section that directed the flow inward and through a cylinder of perforated aluminum to reduce velocity fluctuations. After the layer of perforated aluminum, the flow was directed axially through two more layers of perforated aluminum, separated by one-half inch spacers, a two inch deep annulus of one-quarter inch cell honeycomb and then through an annulus region with decreasing area to prevent

separation of the flow. Figures 13 and 14 show the external features of the airflow apparatus, Figure 16 shows a cutaway view of the airflow assembly and detailed drawings can be found in Appendix C.
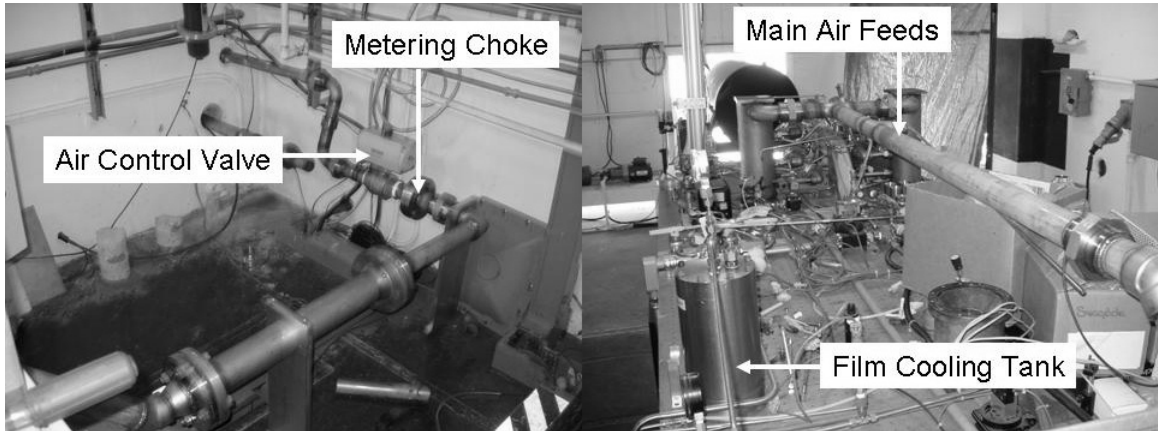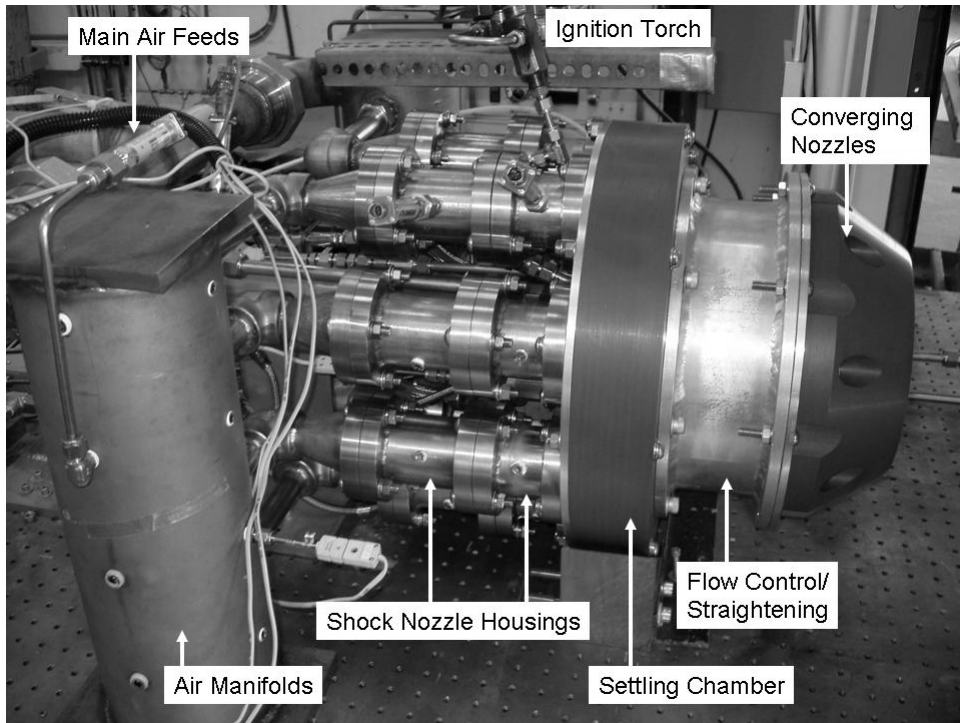

Figure 13.   Air Feed Plumbing

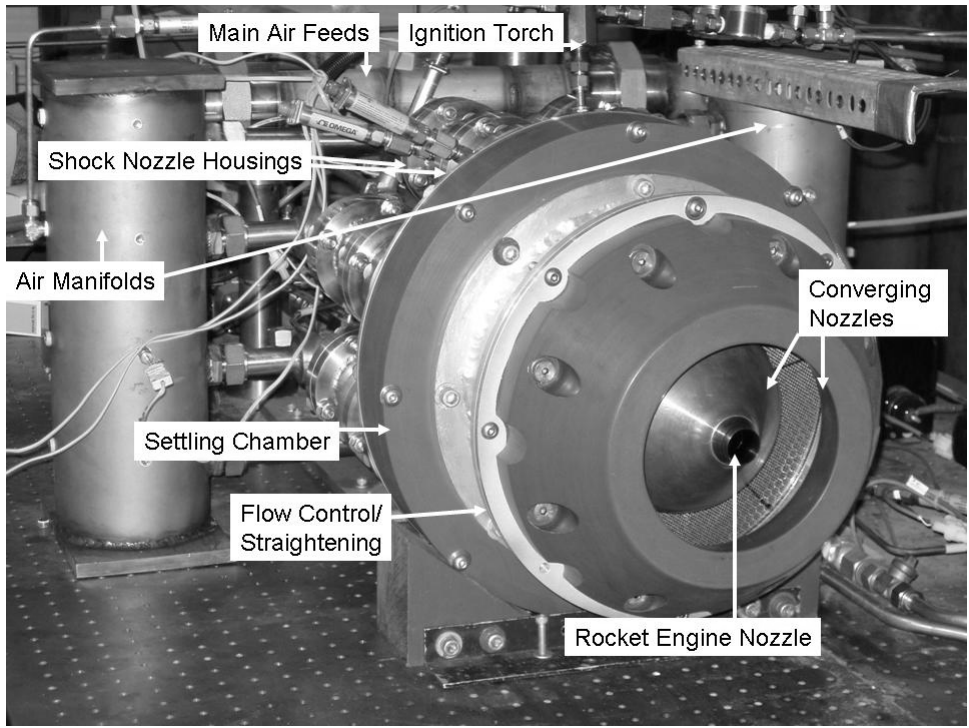Figure 14.   Airflow Assembly: Sideview

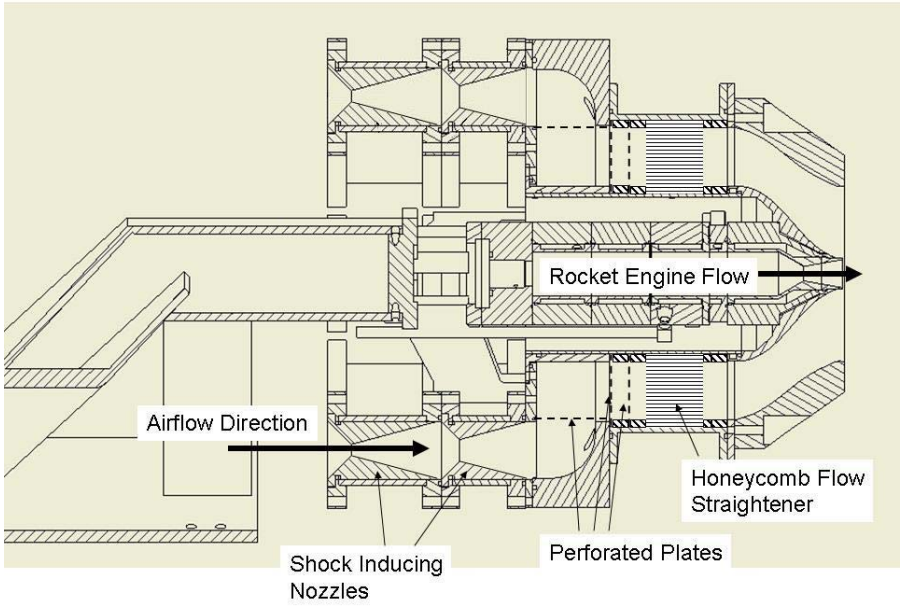Figure 15.   Airflow Assembly: Front Quarter View

Figure 16.   Rocket and Airflow Assembly Cutaway

The radial distribution of airflow velocities was mapped using a hot wire anemometer and compared to the nominal velocity expected based on the mass flow through the choke. During the characterization of the airflow distribution, a nitrogen purge through the rocket was enabled to prevent the formation of a recirculation zone within the core area for a better representation of the distribution during a hot fire test. Figure 16 shows the distribution of velocity and turbulence intensity over one quadrant of the airflow, consolidated by radius. The spike in both velocity and turbulence at the origin is an artifact of the nitrogen purge flow through the rocket engine, and should be ignored when evaluating the airflow distribution. Also, the turbulence intensity is much higher around the edge of the airflow region, showing the effects of the boundary layer on the outer edge of the nozzle. There is a relatively large wake in the region of the nozzle, indicating that the flow may have separated on the inner side of the nozzle. While the hardware was designed to minimize this condition, it is likely representative of the actual conditions for operational rocket engines. Since the aft regions of operational rockets and missiles tend to be blunt and have large amounts of exposed plumbing, leading to separated flow. The data is the result of seven horizontal scans during seven different tests, and some part of the variation in velocity contained in Figure 17 is due to a variation in the actual air delivery between tests. However, there are consistent trends, in that the velocity is actually very close to the overall prediction, and the turbulent intensity is very consistent at about 5% across the quadrant.
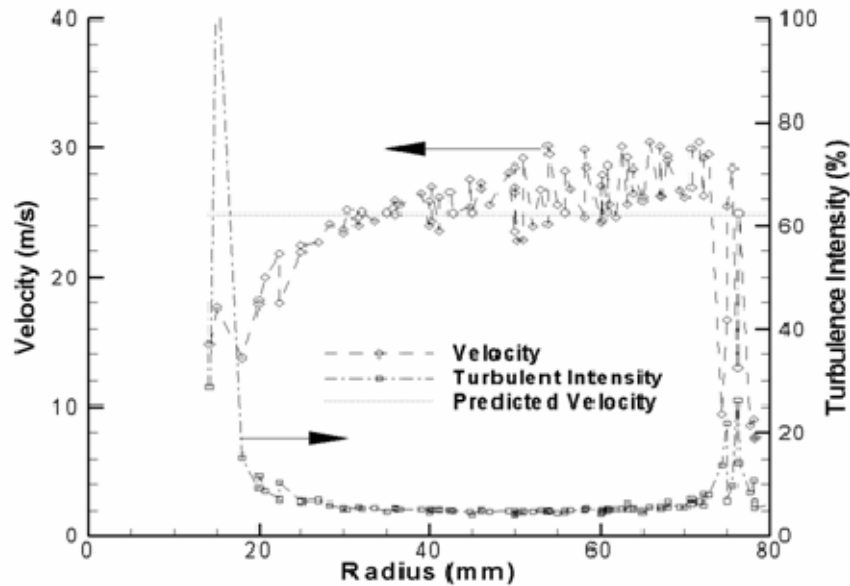
Figure 17. Co-flow air velocity and Turbulent Intensity for 100 psi Choke Pressure

C. CONTROL, INSTRUMENTATION AND DATA COLLECTION

1. Control

The rocket engine was controlled using a Visual Basic graphical user interface. The program allowed the user to specify the target chamber pressure, oxygen/fuel ratio, run time duration, ignition timing, and the timing of the film coolant injection. The chamber pressure and O/F ratio were determined using chokes and cavitating venturies by controlling the metering pressures of the oxygen and the nitrogen pressurization for the fuel tank. The program calculated the pressures required to achieve the desired mass flows for both the chokes and venturies. The plumbing featured multiple cavitating venturies which could be selected individually or in pairs, using a system of hand-operated ball valves to allow more variation in fuel and film mass flow rates.

The GUI provided real time updates of the various rocket operating conditions, including chamber pressure, fuel manifold and venturi pressure, oxygen manifold and choke feed pressure, nitrogen purge pressure, film cooling venturi and manifold pressure, and cooling water temperatures exiting the third chamber section and the nozzle assembly. The data was saved into output files for each run.

Ignition was accomplished using a hydrogen/oxygen torch. The reactants delivered to the torch were set using chokes. The torch was set for a hydrogen-rich mixture to provide fuel rich combustion products to the chamber for easier ignition. Igniting the torch was accomplished using an MSD-6AL automotive multiple spark capacitive discharge system and spark plug operated at 50 Hz.

2. Instrumentation

Diagnostics of the plume were carried out using multiple systems, including two video cameras, an infrared (IR) camera, an intensified camera and a neodymium-yttrium-aluminum-garnet (Nd-YAG) laser sheet for illumination. A photograph of the instrumentation is presented in Figure 18 with schematics of the viewing angles and positions.
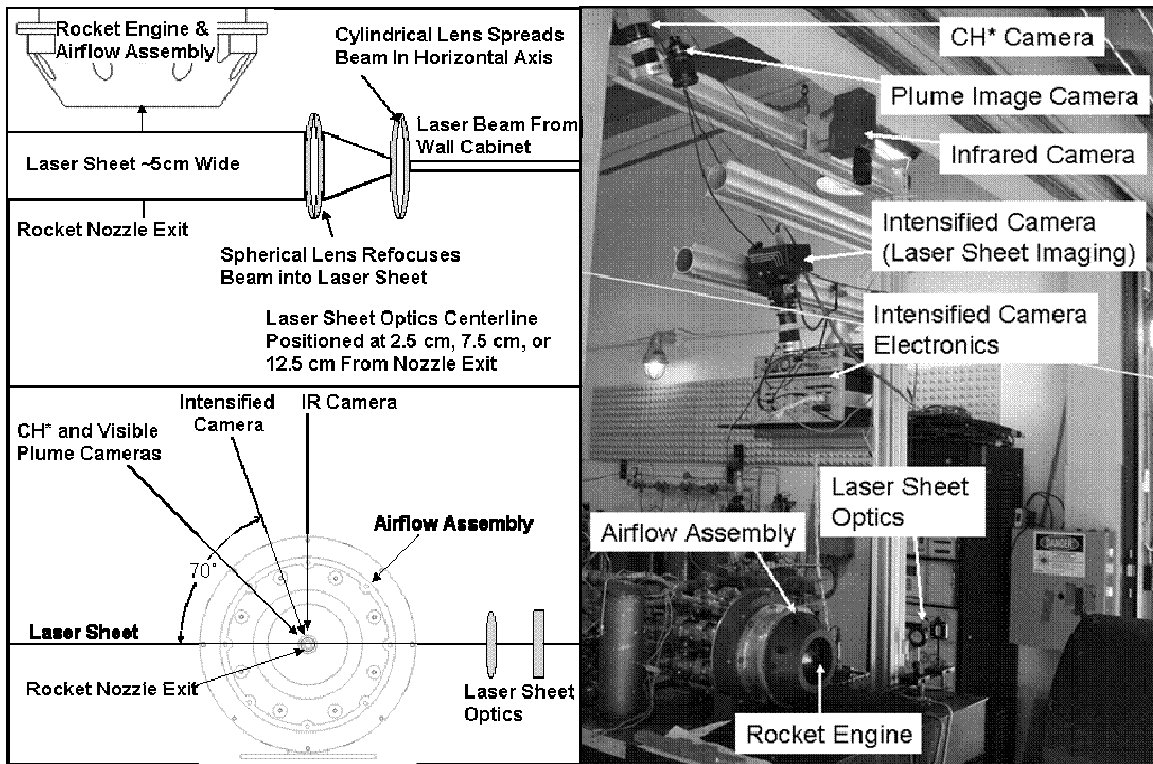

Figure 18.   Instrumentation Layout

a.   CH* Video

To determine the location of hydrocarbon-air combustion within the plume, a video camera was fitted with a 431.5 nm optical filter with a 3 nm bandpass.

36

The aperture of the video camera was set very low, to further limit the small portion of the broadband radiation within the bandpass of the filter. To check the degree to which the broadband radiation was eliminated, a test was made using the 531.5 nm bandpass filter used to image the laser sheet light. This filter had nearly identical bandwidth (5 nm), and a similar center wavelength. The video showed no broadband emission above the noise in the video signal. Since the 531.5 nm bandpass filter was at a longer wavelength, and used a slightly wider bandwidth, the broadband emissions recorded should have been stronger than those in the 431.5 nm filter's bandpass. This demonstrated that we could assume that broadband emission was not present in our images. By filtering out nearly all of the broadband emission, the 431.5 nm molecular emission due to chemiluminescence the CH* radical could be spatially imaged. This chemical species has a very short lifespan and is formed during the early steps of hydrocarbon combustion. While there are many potential products formed during hydrocarbon/air combustion, the CH* radical is formed relatively early in the combustion process, and produces a distinct chemiluminescent signature, making CH* radiation a useful diagnostic tool. In this research, hydrocarbons included the kerosene film coolant, the products formed from the heating and decomposition of the kerosene film coolant, and the ethanol film coolant. Due to the short lifespan, there should be little or none still present from the combustion chamber, and none was detected in the core near the nozzle exit. Using the video images of the CH* emission, the location of reactions could be determined at 30 Hz throughout the run time. This permits about 50 good data points in each three second run, discarding the start-up and shut-down transient periods. Combining data over several runs, a large number of samples were used to determine a mean ignition location and the approximate distribution of ignition locations.

b. *Visible Plume Image Video*

A video camera using no filters was mounted very near the CH* video camera, but with the aperture closed to it's minimum setting. This camera captured the visible emission from the plume for comparison to the CH* image, which allowed the determination of where the ignition is taking place radially, in relation to the visible plume boundaries. Even with the aperture closed to it's minimum setting, the image was completely saturated, so that only the outer boundaries could be measured.

c. *Infrared Camera*

The IR camera was mounted directly above the rocket, and was intended for determining the spatial temperature distribution in the plume. The bandpass of the IR camera was set for 3.5 to 5.0 micrometers

d. *Intensified Camera and Laser Sheet*

A Princeton Instruments intensified camera with a 576 by 384 pixel detector allowed images to be recorded of the laser sheet's scattered radiation from the soot existing in the film cooling layer around the rocket exhaust core. The camera was fitted with a 532 nm filter with a 5 nm bandpass to eliminate broadband radiation, and the aperture was set low to eliminate the broadband radiation effects. The camera was gated by a PG200 pulser and set for a 50 ns exposure triggered by the laser's Q-switch output. The laser was set for 2 Hz operation, while each frame from the camera takes just over one second to transfer to the computer. The laser pulse every 0.5 seconds triggered a new image, producing a single 576 by 384 pixel frame on the computer with two images of the laser sheet illumintated area approximately 240 by 384 pixels, and a small portion of a third. This generally allowed two useful images from each test. The laser was protected from the test cell environment by placement in another room, and the beam was directed into the cell through a cable tray using several mirrors. The beam was spread using a cylindrical lens mounted on the test cell's optical table, and refocused into a flat sheet aimed to cross the plume at the midline. The intensified camera was placed at about 20 degrees off vertical to correspond to a strong lobe of the expected scattering pattern from the expected soot particles, with diameters less than 100 nm. Three axial locations, two inches apart, were used for the laser sheet and camera to produce images up to 14 centimeters back from the nozzle exit. These data were used to estimate the actual shear layer growth rates, since most of the shear layer growth should be from the air/film layer side, rather than the core/film layer side, and in a fairly short distance, the two mixing layers will combine, and there will be only a core/air driven mixing layer.

3. Data Collection

Three methods of data collection were used for this research. Video data was collected using a quad-processor, that combined the four video signals into a single frame simultaneously showing the data from all four cameras, as well as incorporating a text

display of the run number, chamber pressure and operating oxygen/fuel ratio. This data was captured using a conventional video cassette reporter (VCR), and later recopied onto digital video disc (DVD) media. Video capture software allowed snapshots of individual frames from the DVDs for data extraction and presentation purposes. The data relating to the health and operational status of the rocket engine was collected using a 14 bit National Instruments PCI-MIO-16E-4 digital data acquisition card installed in the control PC. The GUI captured the pressure transducer and thermocouple data and produced an output file for each run with all data saved in 0.1 second intervals. The intensified camera sent serial digital data to a separate computer that used WinView32 software to reconstruct the intensified camera images. The images were then saved for later exploitation, and could be transformed into conventional graphic (bitmap, JPEG, GIF) formats, for use in documents.

THIS PAGE INTENTIONALLY LEFT BLANK

IV. COMPUTATIONAL EFFORTS

A. HARDWARE/SOFTWARE

Computational Fluid Dynamics (CFD) simulations were performed on a Dell Precision Workstation, using a 3.2 GHz Pentium IV processor and 4 GB of RAM available. A compressible flow solver, known as FASTRAN, was used for the simulations. The software is produced by Computational Fluid Dynamics Research Corporation/Electronics Systems International, and contained modules to handle inviscid flows, laminar viscous flows, turbulent viscous flows, chemical mixing, and chemical reactions in the flowfield. All plume simulations were modeled as axisymetric turbulent flows with chemical mixing. While the software was capable of handling chemical reactions, the primary interest of this research was in hydrocarbon-air reactions, which would require over 80 reaction equations to handle well, and a minimum of eight to ten for a rudimentary attempt. The addition of two to three chemical reactions would result in a significant increase to the computational workload for the CPU and would significantly increase solution time. Therefore, in the interests of minimizing solution time, all runs tracked only the mixing of chemical species, not reactions. Since reactions were not included, there was no possibility of determining ignition locations, except by determining where the mixture was potentially combustible.

The FASTRAN software calculates solutions based on the Farve-averaged Navier-Stokes equations. Farve-averaging uses density and density/velocity products as conserved variables to capture the mean effects of turbulence on the flowfield solution. Extra terms, representing the additional stress caused by turbulence, are modeled to capture the effects of turbulence at scales smaller than the grid. The extra stresses are modeled using a k-ε turbulence model. The k-ε turbulence model was shown in research by Pergament, Dash and Varma [17] to best capture rocket exhaust plume dynamics.

B. FILM COOLING PERCENTAGE

The film cooling percentage mentioned throughout this effort is the percentage of the total mass flow of the engine (core products plus film coolant) that is represented by the film coolant, or:

$$\text{Film Cooling Percentage} = 100 \bullet f_c = 100 \bullet \frac{\dot{m}_{Film}}{\dot{m}_{Film} + \dot{m}_{core}} \tag{26}$$

Therefore, a five percent film cooling value indicates that five percent of the total mass flow exiting the engine is film coolant, which equates to $(5/95)$ or 5.26 percent of the core mass flow.

C.   INTERNAL SIMULATIONS

Due to hardware and software limitations, external flow simulations were limited to purely axisymmetric geometries. However, as discussed above (Chapter II, section E) when the convective Mach numbers are relatively high, as in the case of all the experimental flows considered, the flow will not be purely axisymetric, but contain a swirling turbulent structure. The resulting flow requires a fully three dimensional simulation, with relatively fine grid structure in all three coordinates to properly resolve the flowfield. The grid also would have to represent a relatively large physical area to reduce the effects of the imposed boundary conditions on the areas of interest. This would require significantly more time consuming simulations, and more computational resources than were available. Therefore, the simulations were aimed at gaining a qualitative understanding of the injection and mixing of the film coolant into the combustion chamber and how the film layer's bulk temperature changed during the transit time within the combustion chamber. The flow within the combustion chamber occurs at a very low Mach number and can be reasonably expected to remain purely axisymetric. Unfortunately, FASTRAN was not equipped to allow a steady stream of liquid to be injected along the edges of a gaseous flow and undergo phase changes after being heated by hot gases. Therefore, it was necessary to model the injection of a cool gaseous flow of film coolant and ignore the wall temperature effects that would depend on the phase change process. The film cooling injection slot width was adjusted to keep the gaseous film coolant velocities close to the velocities expected for a liquid film coolant.

The result of the computational study was a qualitative knowledge of the distribution of the film coolant in the exhaust flow from the rocket engine. Figure 19 shows the film thickness may potentially be estimated from the film cooling percentage by calculating the thickness of the annulus around the outside of the nozzle exit that makes up the same percentage of the nozzle exit area:

$$t = r - r\sqrt{1 - f_c} \equiv \text{ film thickness}$$

$$\frac{t}{r} = 1 - \sqrt{1 - f_c} \equiv \text{ radial fraction of film coolant} \tag{27}$$

where r is the radius of the nozzle at the exit plane

The points were calculated by finding the thickness at which the film coolant concentration exceeded 80%. Equation 27 indicates that a 5% film cooling will lead to a film thickness of 0.0253r, and 10% will lead to a thickness of 0.0513r. Figure 19 was derived from the data presented in Figures 19 and 20, showing the distribution of the water film layer across the exit of a simulated rocket. Figures 20 and 21 indicate that the velocity distribution is not significantly affected by the presence of the film layer. However, the velocity distribution is not necessarily entirely accurate, due to the inability of the software to include the effects of injecting a liquid film coolant and allowing its transition to a gas film. A liquid film would not be expected to accelerate as rapidly inside the combustion chamber, and would remain significantly cooler and denser than the purely gaseous layer. These effects could combine to alter the velocity of the film layer at the exit plane, and for a fixed mass flow of film coolant, the thickness of the film cooling layer would also be affected. Therefore, the CFD results for the velocity distribution and film cooling layer thickness should be viewed as qualitative only.
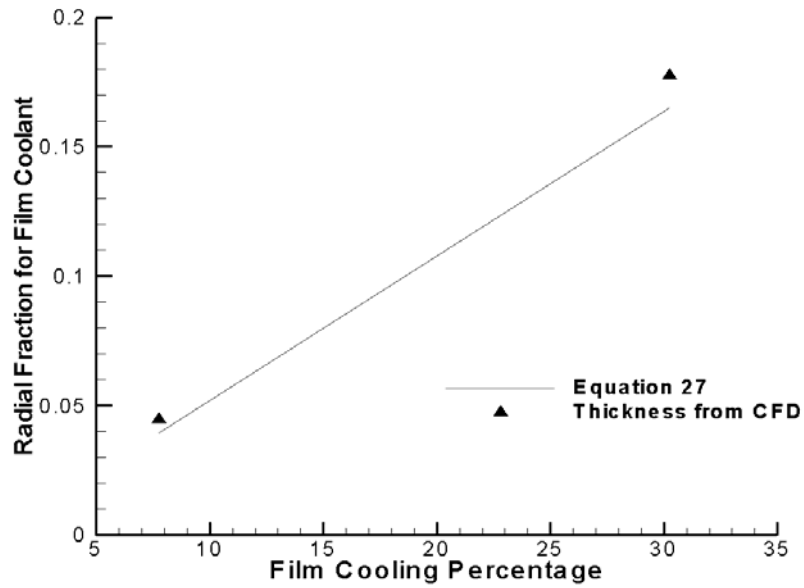
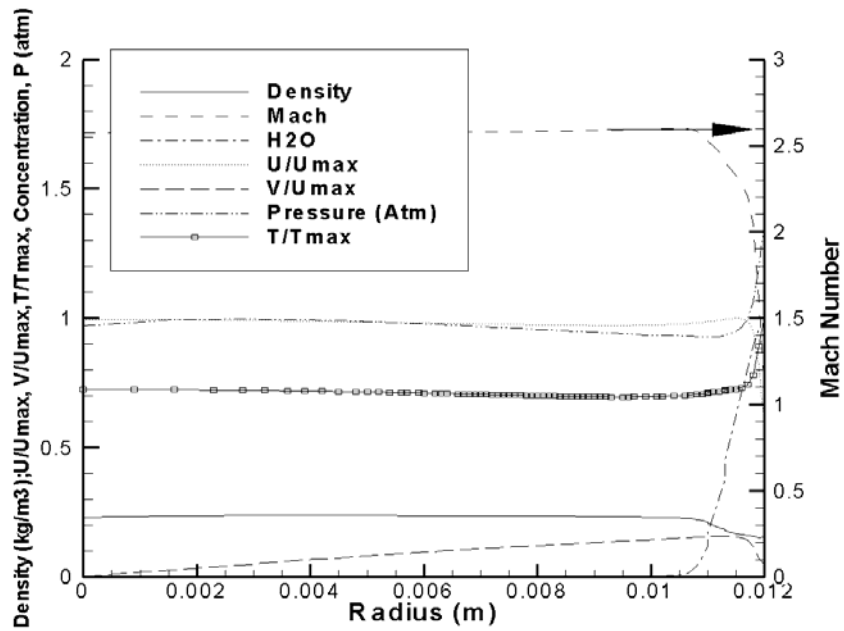Figure 19.   Coolant Film Thickness as a Function of Film Cooling Percentage

Figure 20.   Computed Nozzle Exit Conditions for 7.8% Film Cooling
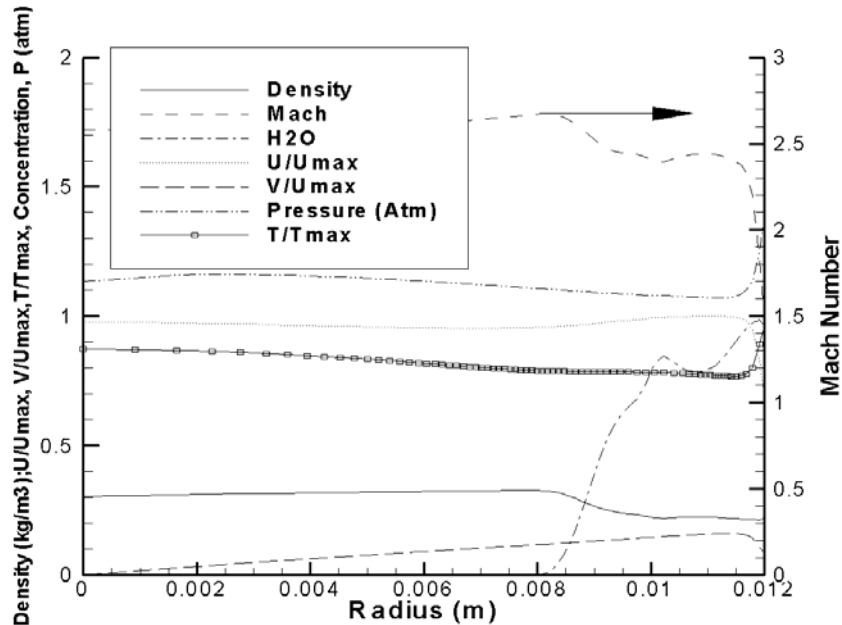
Figure 21.   Computed Nozzle Exit Conditions: 30.2% Film Cooling

The grid for the internal simulations was based on the geometry of the laboratory scale engine used in the experimental portion of the research and featured tighter grid spacing near the walls and transition areas such as the nozzle throat, core and film inlets and nozzle exit. The minimum grid spacing was 38 μm (at the wall in the nozzle throat), while the maximum grid spacing was about 0.9 mm (at the centerline, axially in the middle of the combustion chamber). Images of the internal flow computational domain can be found in Appendix A.

D.   EXTERNAL SIMULATIONS

Although a full three dimensional simulation was prohibited due to hardware and software limitations, axisymetric simulations were performed for comparison to theoretical results. Most simulations were made without film cooling and assumed a 4:1 H_2/O_2 mixture ratio in the combustion chamber, leading to core exhaust gases with nearly equal mass fractions of water and hydrogen. The shear layer thickness was determined by evaluating the radial position where the water concentration went from 5% below the core concentration (49%) to 5% above the air concentration (0%). The shear layer boundaries are shown in Figure 22, and the thickness is shown in Figure 23.

The shear layer growth observed in the CFD was well below theoretical predictions. Analytical theory predicts an approximately eight percent growth rate for the simulated conditions, but the computational results produced about 1.4 percent. The substantially reduced growth rate values were at least partially due to the CFD forcing axisymetric limitations on the flow, where the real vortex structure would be helical. The rectilinear structure of the grid used for the simulations may also have limited the shear layer growth, by artificially constraining the solution along the grid lines. An expanding shear layer region built into the grid or an unstructured grid might have yielded different results, at the cost of potentially introducing different grid dependencies. Since the flow in the simulation will prefer to follow the lines of the computational grid, an expanding shear layer region may artificially force a fixed growth rate on the simulation. An unstructured grid of mixed triangles and quadrilaterals may be a better choice for the simulation, but introduces its own issues, making grid generation more difficult, and prone to creating poor grid geometry in the form of very narrow angles, especially in the triangular cells. The inability of an axisymmetric simulation to capture the full effects of a helical mixing structure reveals the necessity for CFD simulations of rocket exhaust plumes to be fully three dimensional allowing the formation of the helical mixing modes. This requirement, coupled with the need for high spatial resolution to capture mixing behavior, makes such simulations impractical using commercial CFD software on a single personal computer. A parallel processing configuration, with large memory reserves would be required to make practical simulations. Even with such capabilities, the issues involved with simulating the chemically reacting, turbulent flows, would restrict the utility of the simulations to very simple cases, with simplified chemistry.

The grid for the external simulations started 5 cm upstream of the nozzle exit and extended 45 cm past the nozzle exit axially and to 25 cm radially. The external grid had tighter grid spacing towards the nozzle walls, and near the lines axially back and radially outward from the nozzle lip. The minimum grid spacing was approximately 0.9 μm near the nozzle lip and the maximum grid spacing was approximately 9 mm approximately 0.25 m back from the nozzle lip at the outer edge of the computationally domain. Appendix A contains images of the external computational domain.
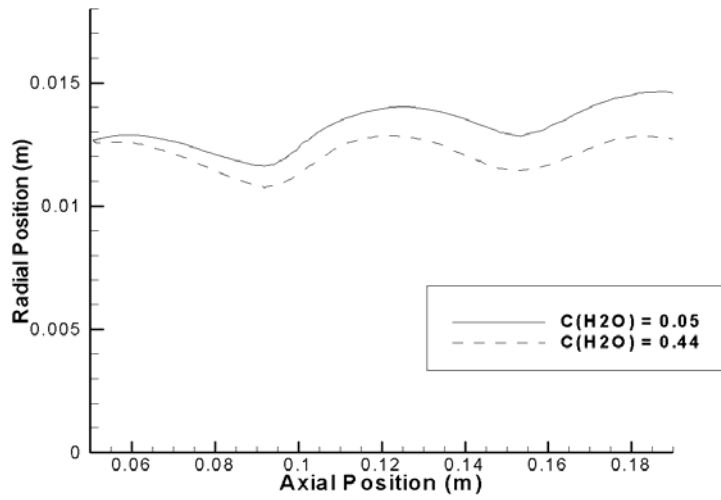
46

Figure 22.   Shear Layer Boundaries from CFD (Based on Water Concentration)
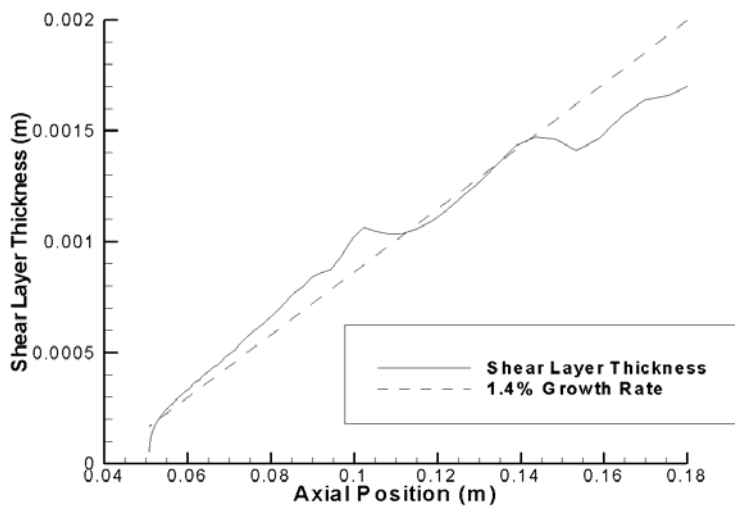

Figure 23.   Shear Layer Growth Rates from CFD

THIS PAGE INTENTIONALLY LEFT BLANK

V. EXPERIMENTAL RESULTS

The rocket exhaust flowfield consists of a supersonic jet of high temperature gas, surrounded by a thin layer of fuel film coolant at nearly the same velocity and temperature conditions, all surrounded by the airflow. There are a number of features which differentiate the rocket exhaust flow from a standard shear flow, even a normal axisymetric jet flow. The expansion and contraction of the plume, caused by pressure differences at the nozzle exit, produces a series of curved barrel shocks, with normal shocks, or Mach disks, in the flow between the expanding and contracting sections, as shown in Figure 24 [18]. The mixing layer surrounds that structure eventually combines enough air with the fuel rich products of the core and film layer, to produce a combustible mixture. The combustible mixture spontaneously ignites due to heating from the hot core gases, and the resultant chemical heat release causes thermal expansion of the mixing layer and enhances the entrainment of air into the mixing layer.
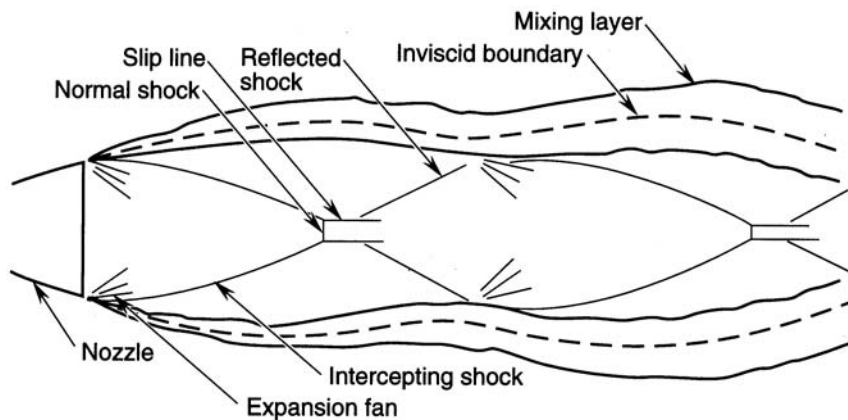
Figure 24.   Rocket Exhaust Plume Features (From Ref. [18])

A.   SHEAR LAYER GROWTH RATES

Shear layer growth rates were characterized, by observing the mixing, expansion and generation of a soot layer around the core of the plume. The soot layer was generated by local O/F and temperature conditions. A typical intensified camera image of the soot present in the flowfield is shown in Figure 25. Shear layer thicknesses were measured at

brightness similar brightness, and the large number of data points was used to reduce the effects of subjectivity on the growth rate determined from these data.
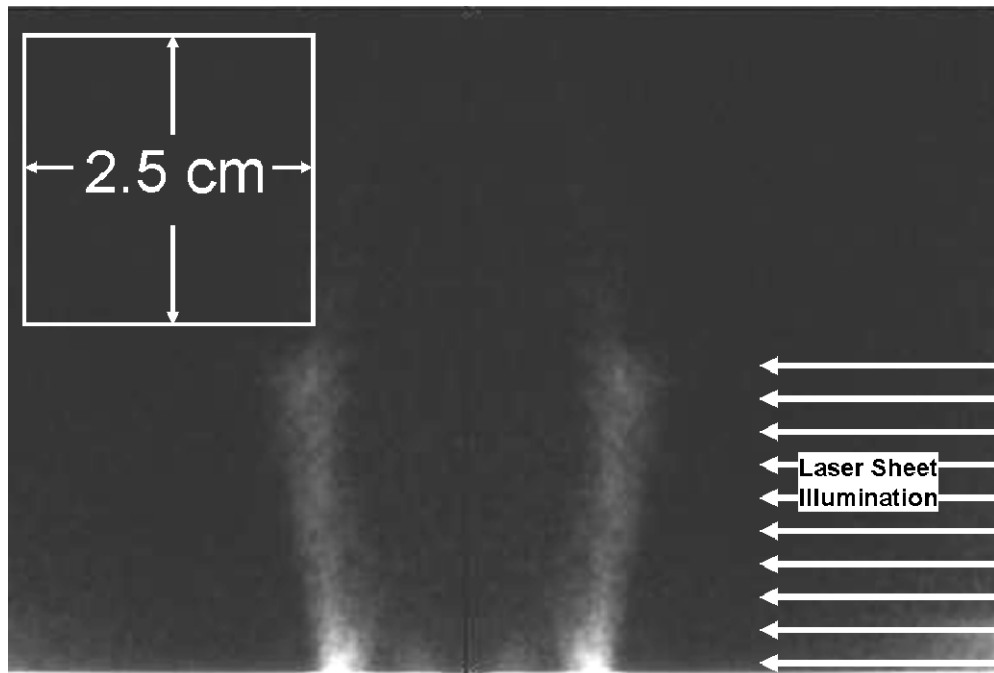
Figure 25.   Typical Intensified Camera Image (Rocket Flow is from Bottom to Top)

Data for different co-flow air velocities is summarized in Figures 26 through 29. The growth rate trends were calculated by two different methods. The first was a simple linear fit to the data, by performing a least squares regression, which produced the slope specified in the figures. The second method was developed due to an obvious discontinuity noted in the shear layer thickness data at around the first Mach disk. The Mach disk was generally located about 4 centimeters from the nozzle lip, between the field of view of the first and second positions of the Nd-YAG laser sheet. Since this area was not always imaged, the effects were determined through consideration of all diagnostics applied. Standard theoretical mixing models do not account for the type of rapidly turning flow caused by compressibility effects near the Mach disks. Near the first Mach disk, the streamlines in the flowfield change directions rapidly from radially inward to outward, resulting in locally high turbulence and rapid mixing, increasing the thickness of the soot layer in a significantly shorter distance. Figures 26 through 29

reveal that the thickness apparently increases dramatically about 4 centimeters axially downstream of the nozzle exit plane. This observed increase in thickness is accounted for in the second growth rate estimate. Essentially, two linear fits were performed, one to the data from the first laser sheet position, and one to the data from the second and third laser sheet positions. The slope was held common between the two, and the y-intercepts were allowed to vary. Airflow velocity calculations based on mass flow through the metering choke can be found in Table 3, and all growth rates are summarized in Table 4. The two intercept curve fits were about 20-25% better than the single linear fits, based on the sum of the residuals. The two-intercept model calculations have been used throughout the remainder of the calculations, due to the ability of the model to better capture the observed behavior of the shear layer and flowfield structure. Estmates of the standard deviation in the growth rate estimates were determined from the quotient of twice the mean distance from the two-intercept line fits to the individual data points, and the axial distance between the data point closest to the nozzle lip and the data point furthest away. The estimates of the standard deviation in the growth rates are located in Table 5.
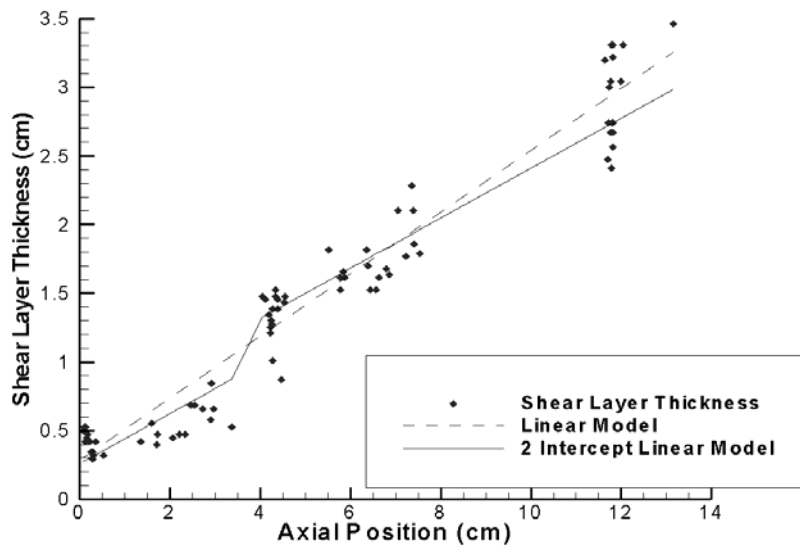
Figure 26.   Shear Layer Growth Data for 0 m/s Co-flow air velocity
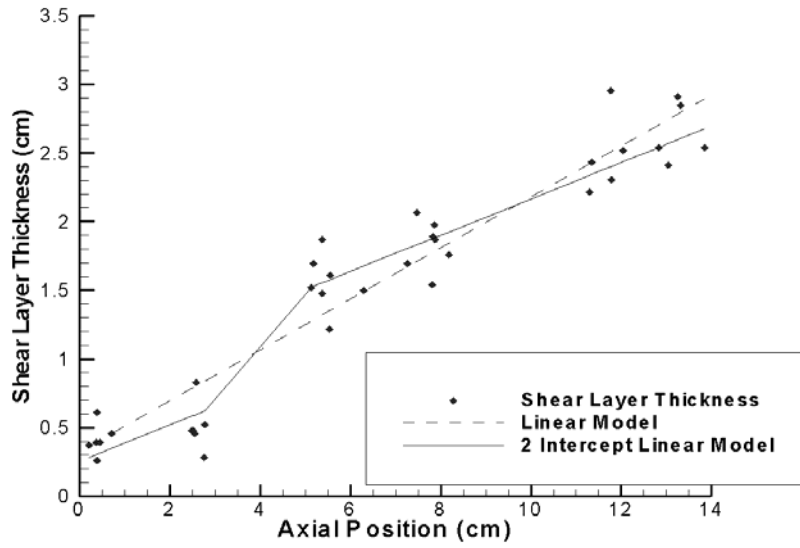
Figure 27.   Shear Layer Growth Data for 50.1 m/s Co-flow air velocity
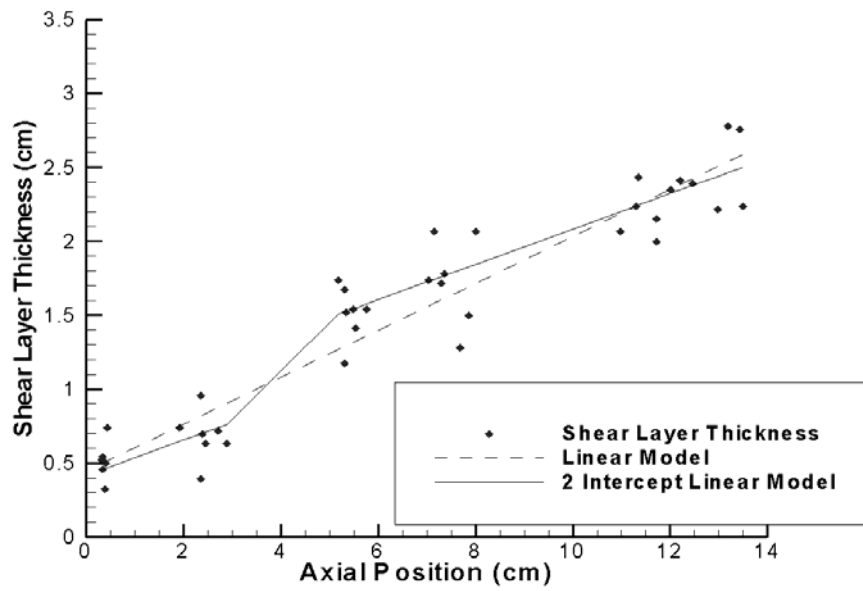
Figure 28.   Shear Layer Growth Data for 96.5 m/s Co-flow air velocity
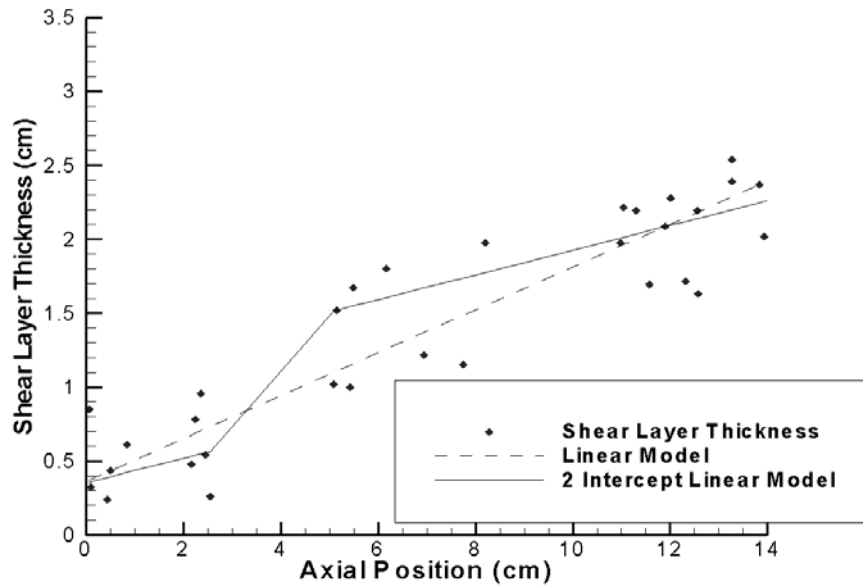
Figure 29.   Shear Layer Growth Data for 181.7 m/s Co-flow air velocity

Table 3.   Airflow Velocity Determination

Airflow Set Pressure (Pa)	Mass Flow (kg/s)	Output Velocity (m/s)	Airflow Parameters	
0	0	0	Choke Area	$2.8502 \bullet 10^{-4} m^2$
1.55x10⁶	1.1	50.1	Exit Area	$1.7735 \bullet 10^{-2} m^2$
3.10x10⁶	2.2	96.5	Exit Pressure	101300 Pa
6.20x10⁶	4.4	181.7	Total Temperature	280 K

Table 4.   Summary of Growth Rates Calculated from Intensified Camera Images

Co-flow Air Velocity	Single Intercept Linear Fit Growth Rate	Two Intercept Linear Fit Growth Rate
0 m/s	22.56%	18.20%
50.1 m/s	18.55%	13.24%
96.5 m/s	15.87%	11.97%
181.7 m/s	14.48%	8.37%

1.   Comparison of Shear Layer Growth Rates

Using equations from Chapter II, estimated shear layer growth rate were calculated. Equations (9) and (10) define a relationship using velocities, temperatures, ratios of specific heat and specific gas constants for both the rocket exhaust core and air streams to recursively obtain estimates of convective velocity and convective Mach

number. Then, using the velocities and densities of the core and air flows an incompressible shear layer growth rate was calculated from Equation 5. The estimate for convective Mach number provided a compressibility correction for the shear layer growth rate from Equation 12, and the product of the incompressible shear layer growth rate and the compressibility correction produced the final shear layer growth rate estimate. The air densities are different due to the compressibility effects on the temperature of the air flowing through the airflow apparatus. The results are summarized in Table 5 and shown graphically in Figure 30.

Table 5.   Theoretical and Observed Shear Layer Growth Rates

Co-flow air velocity (m/s)	U_c (m/s)	ρ_{air} (kg/m^3)	M_c	$\delta'_{vis,incomp}$	M_c Correction δ'/δ'_{incomp}	$\delta'_{vis,total}$	$\delta'_{vis,observed}$	$\delta'_{vis,observed}$ Standard Deviation Estimate
0	614.8	1.205	1.85	0.6582	0.3	0.1975	0.1820	0.0249
50.4	651.7	1.253	1.81	0.4023	0.3	0.1207	0.1324	0.0228
96.5	685.6	1.268	1.78	0.3387	0.3	0.1016	0.1197	0.0225
181.7	748.2	1.321	1.71	0.2719	0.3	0.0816	0.0837	0.0342
Rocket Parameters								
V_{jet}				2435 m/s				
ρ_{jet}				0.146 kg/m^3				
T_{jet}				1835 K				
R_{jet}				378 J/(kg*K)				
γ_{jet}				1.22				

B.   OBSERVED IGNITION LOCATIONS

Using the CH* filtered video, ignition locations in the exhaust plumes for the different conditions of film cooling and co-flow air velocity were obtained. A typical view of the imaging data is shown in Figure 31. The four quadrants of the image are as follows: The top left image is a visible image of the plume, which was bright enough to completely saturate the camera, even with the aperture closed to it's smallest setting; the top right image is the CH* filtered video image; the bottom left image is test cell; and the bottom right image is from the infrared camera. The two video cameras for the top two

54

images have nearly identical fields of view and can be compared to see where the combustion was being initiated radially in the plume. The CH* data was taken by measuring the distances in the CH* image in the top right quadrant, and calibrated using images of a calibration target taken without the filters. Three pressure/venture combinations were used to set film coolant mass flows for both kerosene and ethanol, the results of which are summarized in Table 6. Ignition location data is summarized in Tables 7 and 8 for kerosene and ethanol film coolants. Detailed data regarding ignition locations can be found in Appendix B.
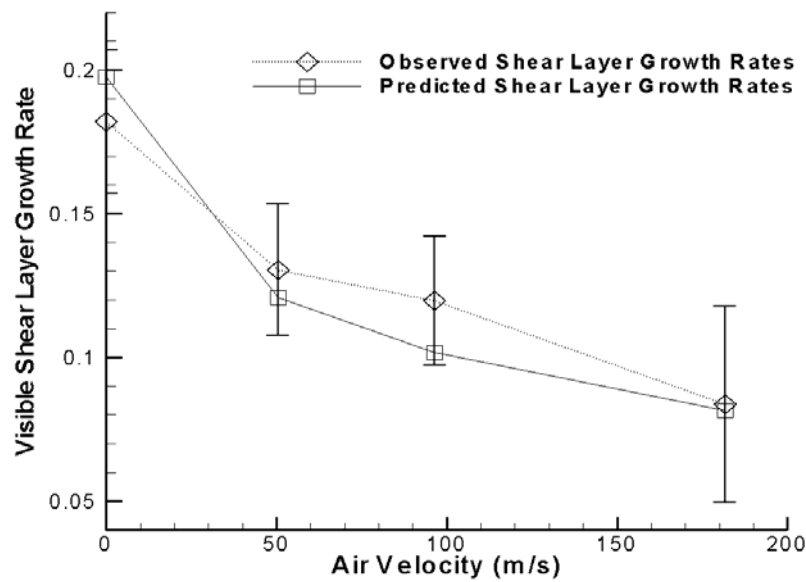
Figure 30.   Observed and Theoretical Shear Layer Growth Rates

Figure 31.   Typical Composite Video Image

Table 6.   Film Coolant Mass Flows Used

Venturi Size (mm)	Set Pressure (kPa)	Kerosene Film Coolant		Ethanol Film Coolant	
		Mass Flow (kg/s)	Film Cooling Percentage	Mass Flow (kg/s)	Film Cooling Percentage
0.508	4825	0.0156	8.44	0.0208	8.95
0.508	6893	0.0185	9.86	0.0244	10.67
0.737	4825	0.0314	15.64	0.0393	17.08

Table 7.   Ignition Location Summary: Kerosene Film Coolant

Film Cooling Percentage	Co-flow air velocity	Mean Ignition Location (cm)	Standard Deviation (cm)	Number of Image Frames
8.4%	0 m/s	3.82	0.33	250
	50.1 m/s	4.27	0.35	282
	96.5 m/s	4.83	0.56	289
	181.7 m/s	5.65	0.97	333
9.9%	0 m/s	4.32	0.39	391
	50.1 m/s	4.84	0.65	290
	96.5 m/s	5.66	0.82	279
	181.7 m/s	6.59	1.03	283
15.6%	0 m/s	5.08	0.56	391
	50.1 m/s	5.73	0.70	285
	96.5 m/s	6.85	1.27	284

Table 8.   Ignition Location Summary: Ethanol Film Coolant

Film Cooling Percentage	Co-flow air velocity	Mean Ignition Location (cm)	Standard Deviation (cm)	Number of Image Frames
8.95%	0 m/s	6.90	0.38	50
	50.1 m/s	7.91	0.29	41
	96.5 m/s	8.48	0.41	35
	181.7 m/s	9.30	0.28	35
10.67%	0 m/s	6.97	0.41	39
	50.1 m/s	7.97	0.50	50
	96.5 m/s	8.77	0.41	50
	181.7 m/s	9.83	0.32	39
17.08%	0 m/s	7.70	0.46	50
	50.1 m/s	9.08	0.31	50
	96.5 m/s	9.80	0.44	42

1.   Comparison of Observed Ignition Locations

Using the either predicted or observed growth rates, Equations 8 and 25 can be used to estimate the ignition locations based on the length required to create a combustible mixture and the ignition delay distance. Equations 8 and 25, restated below, repectively define the mixing lengthscale to generate a combustible mixture for a given flow rate of a specified fuel in the film cooling layer and the timescale associated with the autoignition of an air/fuel mixture of the specified fuel. The timescale defined in Equation 25 can be transformed to a lengthscale through multiplication by the characteristic velocity of the mixing layer, U_c.

Equation 8:

$$l_{mix} = \frac{2\dot{m}_{film}\left(\dfrac{Air}{Fuel}\right)_{req'd}}{\delta'\left|U_c - U_{air}\right|\rho_{air}\left(2\pi r_{mean}\right)}$$

Equation 25:

$$\tau_i = DT_o^{\,2}e^{\left(\frac{F}{T_o}\right)}$$

Applying empirical constants to both lengthscales, to obtain an actual length contribution from each source, and taking the sum of both leads to a total axial ignition location represented by Equation 28:

$$L_{ign} = C_1 \frac{2\dot{m}_{film}\left(\dfrac{Air}{Fuel}\right)_{req'd}}{\delta'\left|U_c - U_{air}\right|\rho_{air}\left(2\pi r_{mean}\right)} + C_2 U_c DT_o^2 e^{\left(\frac{F}{T_o}\right)} \tag{28}$$

The fuel rich limit (air/fuel ratio) for combustion and the ignition time delay constants must be determined for the appropriate film coolant chemistry. The kerosene film cooling cases are complex, due to the coolant chemically decomposing into different chemical species as it heats in the engine and nozzle. However, the combustion of kerosene inherently involves many similar decomposition (cracking-type) reactions as substeps, so overall values for kerosene are used here for mixture ratios and reaction times. Using least squares techniques, the constants C_1 and C_2 were determined to best match the data, for both kerosene and ethanol film coolants. The values $C_1 = 1.036$ and $C_2 = 8.686$ best match all 22 film cooling and co-flow air velocity conditions. Table 9 and 10 tabulate, for kerosene and ethanol film coolants respectively, the mean observed afterburning ignition locations and the statistical variation of the observed afterburning ignition locations, the predicted afterburning location calculated from Equation 28 using the theoretically derived shear layer growth rates from Equations (5) and (12) (also listed in Table 5) {the column headed "Predicted (Theory δ')"} and the afterburning locations predicted by Equation 28 using the shear layer growth rates observed experimentally {the column headed "Predicted (Observed δ')"}. These last two columns demonstrate the difference in ignition location predictions between the theoretically based shear layer growth rates and the experimentally observed rates, although both use empirical constants in the model.

Table 9.   Observed and Predicted Afterburning Ignition Locations (Kerosene Film)

Film Cooling Percentage	Co-flow air velocity (m/s)	Convective Velocity (m/s)	Mean Observed (cm)	Std. Dev. Observed (cm)	Predicted (Theory δ') (cm)	Predicted (Observed δ') (cm)
8.4	0	614.8	3.82	0.33	3.82	3.89
	50.1	651.7	4.27	0.35	4.56	4.45
	96.5	685.6	4.83	0.56	5.01	4.74
	181.7	748.2	5.65	0.97	5.74	5.68
9.9	0	614.8	4.32	0.39	3.99	4.09
	50.1	651.7	4.84	0.65	4.84	4.71
	96.5	685.6	5.66	0.82	5.35	5.03
	181.7	748.2	6.59	1.03	6.16	6.09
15.6	0	614.8	5.08	0.56	4.76	4.92
	50.1	651.7	5.73	0.70	6.08	5.86
	96.5	685.6	6.85	1.27	6.84	6.29

Table 10.   Observed and Predicted Afterburning Ignition Locations (Ethanol Film)

Film Cooling Percentage	Co-flow air velocity (m/s)	Convective Velocity (m/s)	Mean Observed (cm)	Std. Dev. Observed (cm)	Predicted (Theory δ') (cm)	Predicted (Observed δ') (cm)
8.95	0	614.8	6.90	0.38	6.90	6.97
	50.1	651.7	7.91	0.29	7.76	7.66
	96.5	685.6	8.48	0.41	8.35	8.12
	181.7	748.2	9.30	0.28	9.35	9.30
10.67	0	614.8	6.97	0.41	7.07	7.16
	50.1	651.7	7.97	0.50	8.04	7.92
	96.5	685.6	8.77	0.41	8.69	8.40
	181.7	748.2	9.83	0.32	9.76	9.71
17.08	0	614.8	7.70	0.46	7.79	7.93
	50.1	651.7	9.08	0.31	9.19	8.99
	96.5	685.6	9.80	0.44	10.06	9.57

Figures 32 through 37 show significant agreement between the theoretical model and the observed ignition locations for the different levels of kerosene and ethanol film cooling. The observed data is presented with the mean and $\pm 1\sigma$ values shown for each co-flow air velocity level. The model results, using the theoretical calculations for the growth rates, are shown as a dotted line. In all cases, the calculated values are within the $\pm 1\sigma$ range, and in most cases are very close to the observed mean location. The constant multipliers on the ignition reaction timescale, 8.686, and the mixture length scale, 1.036, were taken to form the best fit to the observed data, in a least-squares sense. These multipliers make sense objectively, as combustion would be more likely when the local mixture conditions are just above the rich limit, and the mixture length scale multiplier would make the mixture about four percent leaner. Additionally, the relatively large multiplier (8.686) on the reaction timescale would reflect the fact that the mixture is very near the rich limit of combustion, which would slow the reactions down. Table 11 shows the contributions to the afterburning ignition location from the two components. The mixing component is that portion of the distance required to produce a combustible mixture in the film layer. The reaction component is the distance traveled by the combustible mixture while it is reacting. For the small scale engine used in this research, the reaction component is 47-89% of the total offset of the afterburning location from the nozzle lip. The variation in the reaction component is due to the variation in convective velocity as the co-flow air velocity changes, as well as the difference in the reaction time between the two film coolants, with the ethanol reaction time being approximately twice the kerosene reaction time. The mixing component varies with the film coolant mass flow, the changing shear layer growth rate with the co-flow air velocity, and the changing rich-limit fuel/air ratio between the two film coolants. The mxing component was somewhat shorter for the ethanol film coolant, due to the somewhat lower air/fuel mass ratio at the rich limit. Since the reaction component does not vary with the scale of the rocket engine, the mixing component, which does scale with the size of the engine, will dominate in larger engines. Thus, for a large engine operating at sea level conditions the reaction time length scale would be of very little impact in the prediction of afterburning

60

ignition points. At high altitudes, where lower pressure conditions exist, the reaction rates would decrease and the ignition reaction distance could become significant.

Table 11.   Breakdown of Predicted Afterburning Ignition Locations

Film Cooling Percentage	Co-flow air velocity (m/s)	Ignition Location Predicted from Theoretical δ' (cm)	Mixing Component (cm)	Reaction Component (cm)
		Kerosene Film Coolant		
8.4	0	3.82	0.94	2.88
	50.1	4.56	1.51	3.05
	96.5	5.01	1.80	3.21
	181.7	5.74	2.24	3.50
9.9	0	3.99	1.11	2.88
	50.1	4.84	1.79	3.05
	96.5	5.35	2.14	3.21
	181.7	6.16	2.66	3.50
15.6	0	4.76	1.89	2.88
	50.1	6.08	3.03	3.05
	96.5	6.84	3.63	3.21
		Ethanol Film Coolant		
8.95	0	6.90	0.81	6.09
	50.1	7.76	1.30	6.45
	96.5	8.35	1.56	6.79
	181.7	9.35	1.94	7.41
10.67	0	7.07	0.99	6.09
	50.1	8.04	1.59	6.45
	96.5	8.69	1.90	6.79
	181.7	9.76	2.36	7.41
17.08	0	7.79	1.70	6.09
	50.1	9.19	2.73	6.45
	96.5	10.06	3.28	6.79
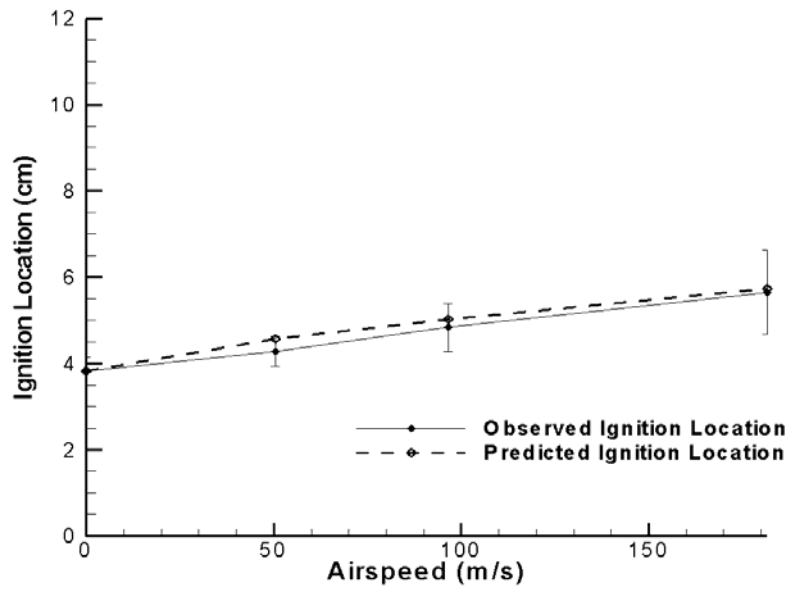
Figure 32.   Model Performance: 8.5% Kerosene Film Cooling
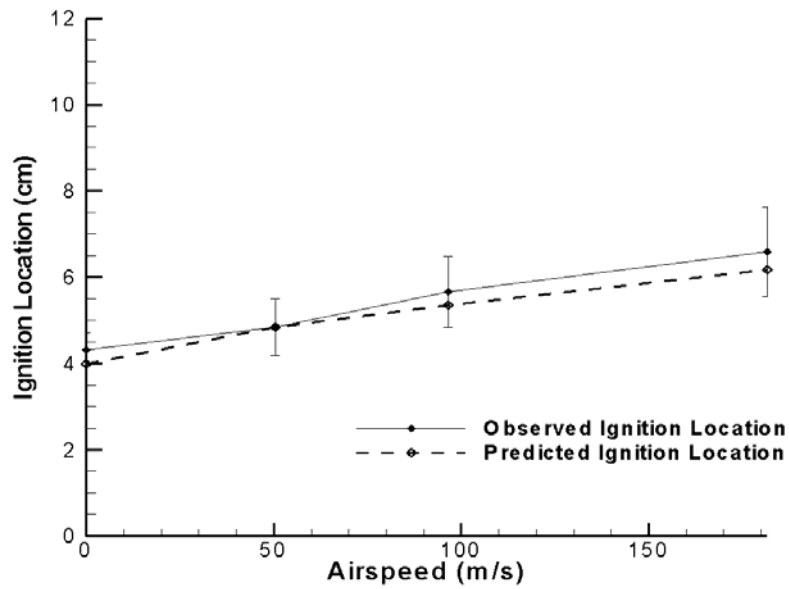
Figure 33.   Model Performance: 9.9% Kerosene Film Cooling
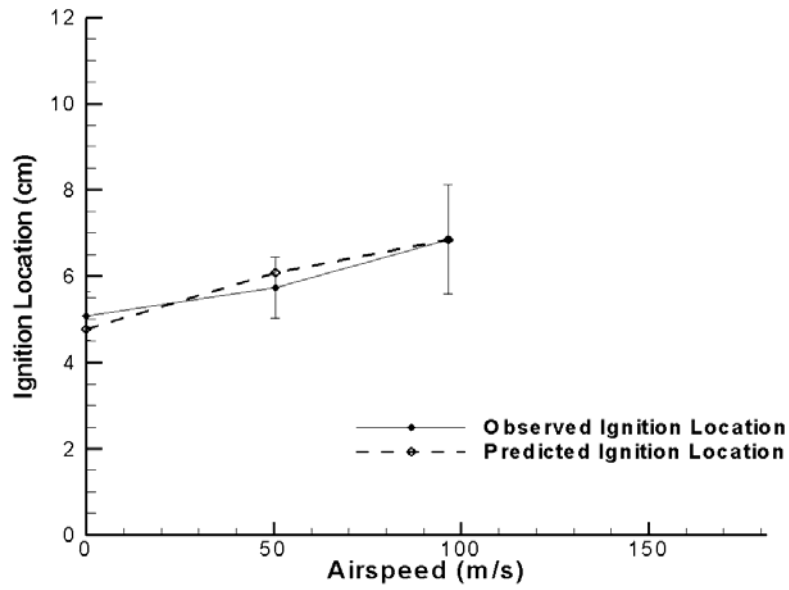
Figure 34.   Model Performance: 15.85% Kerosene Film Cooling
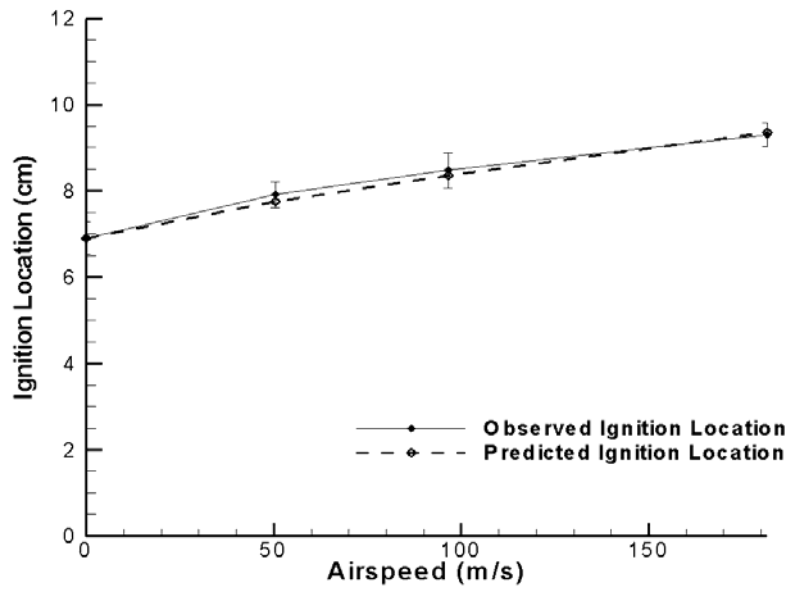
Figure 35.   Model Performance: 8.95% Ethanol Film Cooling
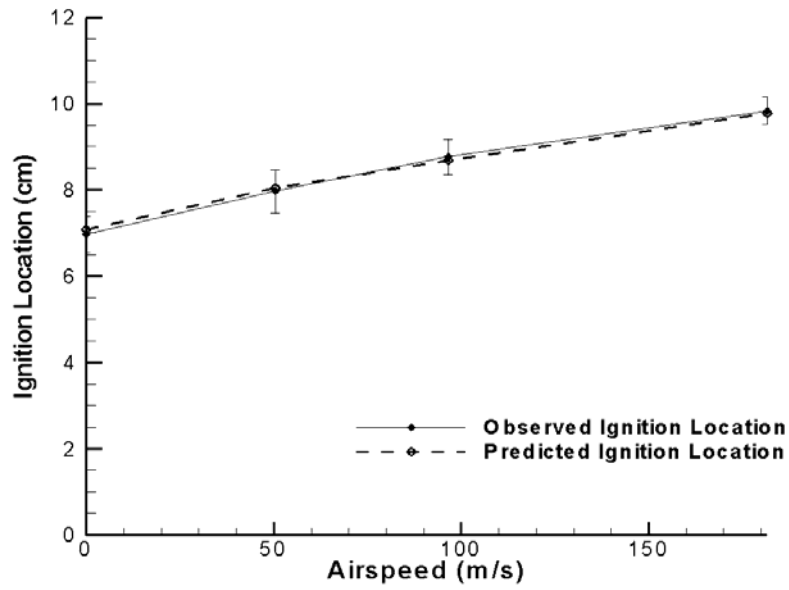
Figure 36.   Model Performance: 10.7% Ethanol Film Cooling
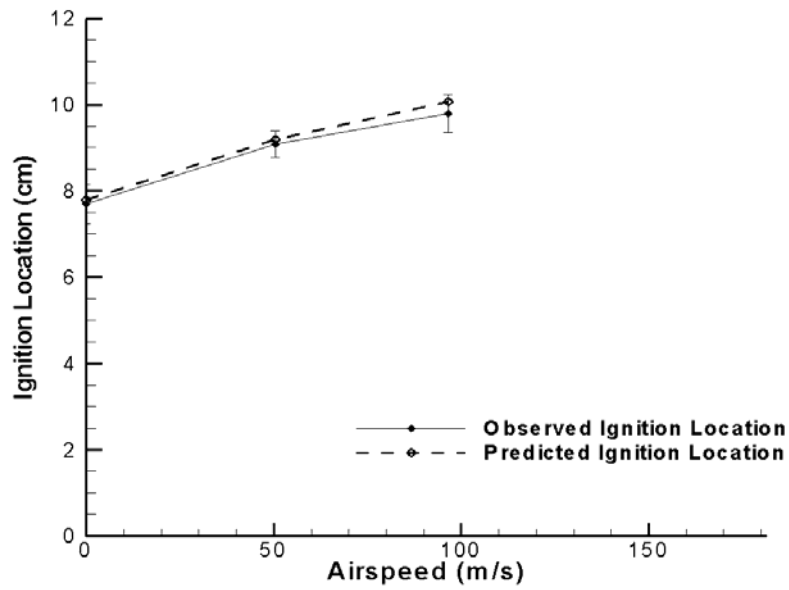
Figure 37.   Model Performance: 17.1% Ethanol Film Cooling

2. Ignition Location Using Intensified Camera

The intensified camera was used in conjunction with a CH* filter to record digital images of the CH* emissions with increased spatial resolution. The images allowed for very fast shutter speeds resulting in near stop-action imaging of the CH* distribution. The increased spatial resolution resulting from the optics used, resulted in a field of view of 81.3 mm cross stream by 121.9 mm axially , with 0.2 mm resolution. The field of view started at about 20 mm downstream from the exit plane of the rocket nozzle. The images, shown in Figures 38 and 39, show ignition locations within the range of those observed in the video.
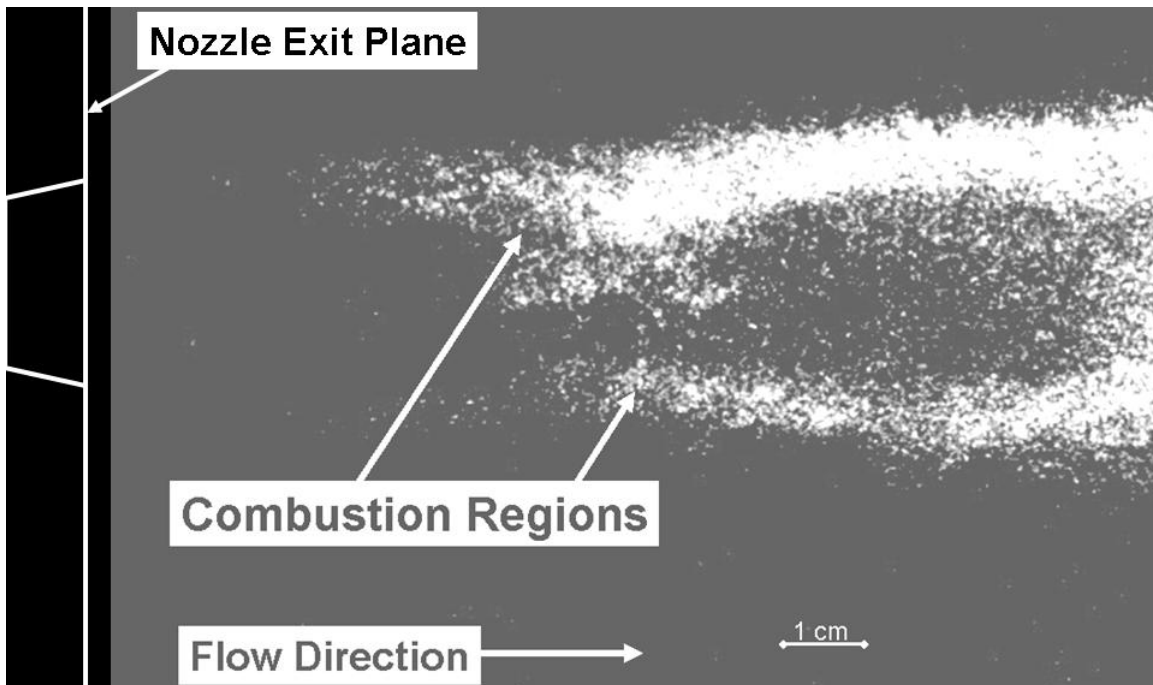
Figure 38.   CH* Images of 9.9% Kerosene Film Cooling, 0 m/s Co-flow air velocity
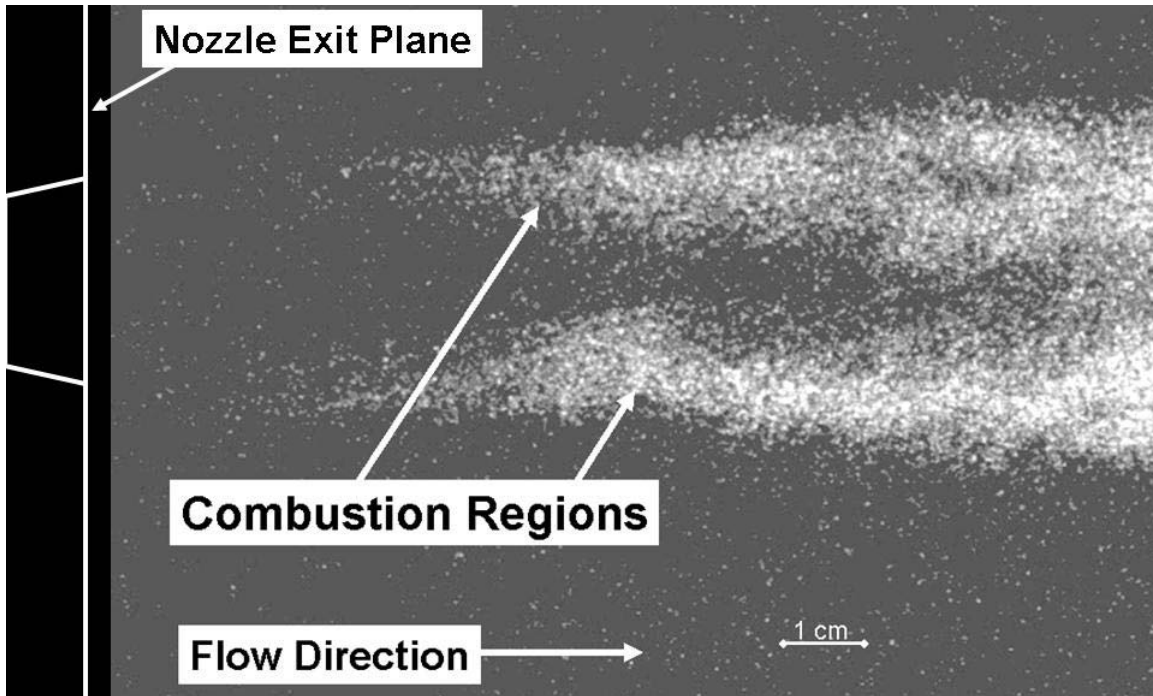
Figure 39.   CH* Images of 8.4% Kerosene Film Cooling, 0 m/s Co-flow air velocity

C.   HELICAL MIXING MODE VERIFICATION

Previous research [9] on axisymetric supersonic jets indicates that a helical mixing mode must exist within the shear layer to permit subsonic effective convective Mach numbers. However, previous verification of the existence of the helical mode was achieved through acoustical data, which represents an indirect verification of this mixing mode. Direct visual verification of the helical mixing existing in a rocket exhaust plume was desired.

Smoke lines were injected around the rocket without airflow to directly image the helical mixing mode. By measuring axial and radial distances on the images of the helical vortex structure, the helical pitch angle of the mixing structure could be estimated. A typical frame is shown in Figure 40. The 531.5 nm bandpass filter used for the laser sheet imaging was used on the video camera to limit the intensity to prevent the video camera from saturating. Time constraints and short run durations allowed only a few frames on each run to be inspected. The convective Mach number was estimated using Equation 20 for the "low" mode results are tabulated in Table 12. However the convective Mach

number was previously calculated to be 1.85 for the zero co-flow air velocity case, using equations 9 and 10. One source for the discrepancy comes from the derivation of the relations in equation 20, which assumed that the convective Mach number was one half the jet Mach number. Regardless of the validity of that assumption in the research of Keefe and Nixon [9], it is clearly not the case for the conditions existing in the rocket exhaust plume. Due to the large difference in speed, composition, and temperature, the convective Mach number is around 70-75% of the supersonic jet Mach number for the zero co-flow air velocity case. The discrepancy in the convective Mach number might indicate that the actual convective Mach number would be about 50% higher than calculated using the Keefe and Nixon relationships. A 50% increase in convective Mach number would produce a mean convective Mach number estimate, from the helical angle, of 1.55, with a 0.26 standard deviation. A convective Mach number range of 1.3-1.9 would encompass the calculated convective Mach number of 1.85. Due to the dependence on acoustical wavelength data in the derivation, an indirect source of the helical angle, direct observation of the helical structure may have produced different pitch angles. Smoke trails were entrained to the vortex structure upstream of the nozzle exit, and the field of view was limited to areas near the nozzle exit. It is likely both that the helical structure was not yet fully developed and that the axial velocity decreased radially as the smoke was entrained and accelerated. A lower axial velocity near the outer, denser regions of the smoke would have lead to slightly lower observed angles than the theory would predict. The method of determining the helical angle was also sensitive to the measurement of the radius of the plume at the point where the helix is observed to wrap around the side of the plume. This is also the element with the greatest uncertainty in measurement. Accurate mapping of the helical mode angle would require additional test cases with more discrete smoke trails and greater ability to vary the convective Mach number while still visualizing the flow.

Table 12.   Helical Mixing Mode Data

Run	Time	Δ x	Δ y	Θ (degrees)	M_c
1215r5	19.9078	38	109	61.29	1.08
	20.1090	35	115	64.45	1.27
	20.4089	35	95	59.94	1.01
	20.4751	35	123	65.92	1.37
1215r6	4.7975	40	88	54.47	0.77
	4.8309	38	102	59.66	0.99
	4.9310	37	102	60.33	1.03
	4.9643	37	107	61.49	1.09
	5.1645	39	122	63.34	1.20
	6.0988	28	67	56.72	0.86
Average/ Standard Deviation (σ)				60.76/ 3.43	1.065/ 0.18

Figure 40.   Helical Mixing Mode

D.   SPATIAL MAKEUP OF AFTERBURNING PLUMES

Figure 41 reveals that the combustion is taking place well inside the visible plume. The dotted lines encompass identical areas of the visible and CH* images, and the difference in width between the two images is clear. Clearly the CH* emissions are coming from the region near the core, rather than near the outside of the mixing layer. Note the clear core structure in the CH* image, while the visible plume image grows wider steadily, with the broadband emission from soot and other particles in the mixing

68

layer masking all of the core structure. The location of the reactions support the conclusion that the afterburning ignition is initiated by contact between the flammable mixture and the hot core.
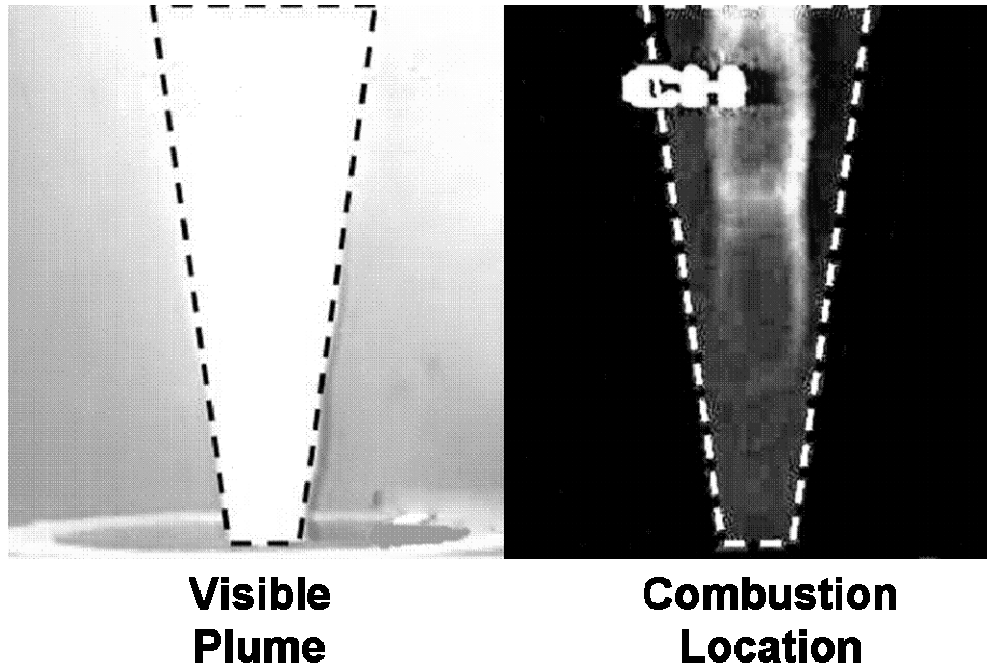
Figure 41.   Comparison of Combustion Location and Visible Plume

E.   APPLICATION OF MODEL TO LARGE SCALE ENGINES

As a preliminary check against the scalability of the semi-empirical model for afterburning ignition location, data from Sutton and Biblarz [19] for an RP1/O_2 rocket was used to develop predictions of the afterburning ignition location for a static firing of a 1.1 MN (250,000 lb) thrust engine, with three percent film cooling, a 2.6 core mass ratio of oxygen to fuel, chamber pressure of 4.48 MPa (650 psia), a throat diameter of 0.21 m, and a 15:1 area ratio between the exit plane and nozzle throat. These conditions match the NASA FASTRAC engine, shown in Figure 42 [20].

Since only a limited number of images were available, a temporal mean afterburning ignition location, such as was used for the experimental data in this research, was impractical. Instead, a spatial mean afterburning ignition location was estimated. To form an estimate of the mean afterburning ignition location, the nozzle lip was estimated

69

using a line from the upper to lower apparent inside edges of the nozzle. Afterburning locations were estimated, from the visual yellow/orange visibly opaque combustion regions at 41 locations in the plume, and a distance calculated from the afterburning location to the line approximating the nozzle lip. In this manner, a somewhat conservative estimate of the mean afterburning ignition location and a standard deviation was determined. The mean afterburning ignition distance was calculated to be 0.32 m, with a standard deviation of 0.17 m. The model prediction for this condition was 0.30 m, very close to the spatial mean afterburning location in the image, and well within the standard deviation of the afterburning locations. The FASTRAC engine has a nozzle exit diameter of about 0.8 m, so the mean afterburning location is about 0.4 nozzle diameters back in the image, while the model prediction would be 0.38 nozzle diameters. The model apparently produces a reasonably accurate prediction of the mean afterburning ignition location for this relatively large engine, as well as the small engine used in this research. Comparable CH* images would be required to improve the comparison of the model predictions.
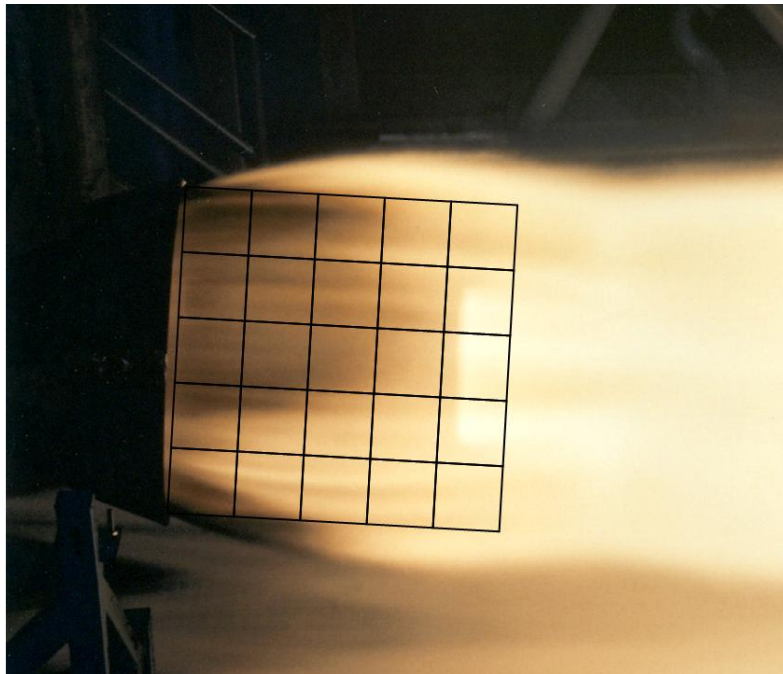
Figure 42.   NASA FASTRAC RP1/Oxygen Engine Plume Closeup (From Ref. [20])

VI.   CONCLUSIONS

The first objective of this research was to develop a mathematical model relating exhaust characteristics of the rocket engine and the properties of the surrounding airflow to the location where combustion would be initiated in the plume. A semi-empirical mathematical model was developed for predicting the mixing behavior and ignition location, specifically for the problem of a reactive shear layer as exists in film-cooled liquid rocket engine exhaust plumes. The model incorporates two components to predict the afterburning ignition location. The first component is the distance required to entrain sufficient air to produce a combustible mixture with the film cooling layer around the rocket exhaust core. The length required to produce the combustible mixture is a function of the mixing layer growth rate, the mass flow of film coolant, the size of the rocket engine, the chemical composition of the film coolant, and the properties of the airstream around the rocket plume. The mixing layer growth rate model was modified from existing planar mixing models to represent the axisymetric mixing case. The planar mixing layer model was altered by changing the dependency of the shear layer growth on the the ratio of the airstream velocity to the rocket core velocity. A correction factor for the effects of compressibility on the mixing layer growth was determined from previous experimental results related to compressible axisymmetric shear layer growth. The second component of the ignition location is the distance traveled by the combustible mixture during the ignition delay. This component depends on the chemical composition of the film coolant and the characteristic convective velocity of the shear layer, determined from the rocket core velocity and airstream velocity. Unlike the first component, the chemical reaction distance is unrelated to the size of the rocket engine, and for larger rocket engines may become negligible. Using the experimental results to determine the empirical constants in the model led to some conclusions about the relative contributions of the two components to the observed afterburning locations. For both reactive film coolants, the reaction component of the distance was indicated by the model to be a significant contribution to the offset from the nozzle lip, with the longer autoignition time of the ethanol leading to

71

distances approximately twice those associated with the kerosene film coolant. The model indicates that the mixing component was significantly dependent on both the film coolant mass flow and the velocity of the airstream.

The semi-empirical model has been validated using a small, laboratory scale kerosene/oxygen liquid rocket engine of approximately 440 N thrust, and airflow velocities from 0 to 182 m/s. While the model has not been compared to data for higher airflow velocities, larger engines, or higher altitude/lower pressure conditions, there are no inherent limitations to the model approach that would prevent its application to those conditions.

Comparison of visible images and images of the afterburning ignition indicate that the ignition reaction is initiated by contact with the hot exhaust core gases, rather than by hot particulate soot present in the shear layer. The ignition is clearly initiated at the interior side of the mixing layer, where hot soot as an ignition source would most likely initiate combustion towards the outside of the shear layer where the mixture would reach the rich limit sooner.

A.   SUGGESTIONS FOR FURTHER RESEARCH

Imaging and spectroscopic data from operational rocket launches could be analyzed to evaluate the applicability of this model in environments that could not be realized in the laboratory. Specifically, the effects of increasing altitude and higher air velocity. The experimental apparatus could also be used with particle image velocimetry techniques to more accurately map the helical vortex structure pitch angle variation with convective Mach number. Additionally, the use of gaseous fuel film components, such as hydrogen or methane, would further allow the assessment of this afterburning ignition model due to their simpler combustion chemistry.

APPENDIX A. COMPUTATIONAL DOMAIN IMAGES
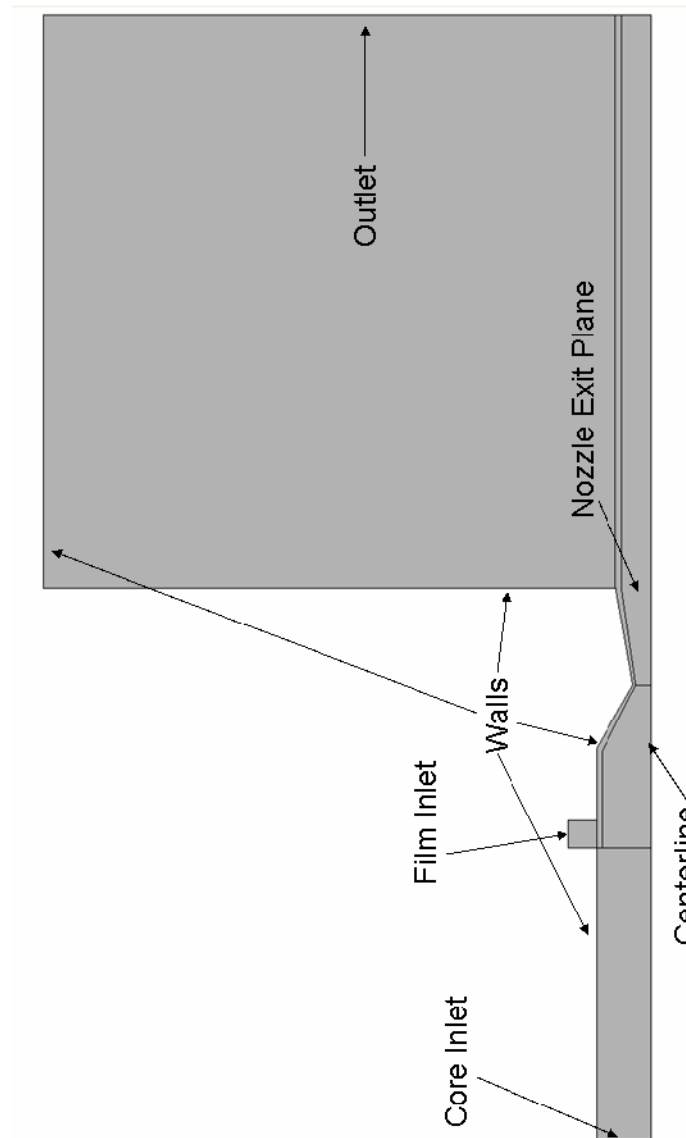
Figure 43.   Computational Domain for Internal Simulations: Overall Domain

The computational domain featured inlets for the hot core gas mixture and the cool gaseous film, and a converging/diverging nozzle which dumps into a large chamber that serves to keep boundary conditions well away from the nozzle exit plane. Since the nozzle exit plane was the primary region of interest for these simulations.
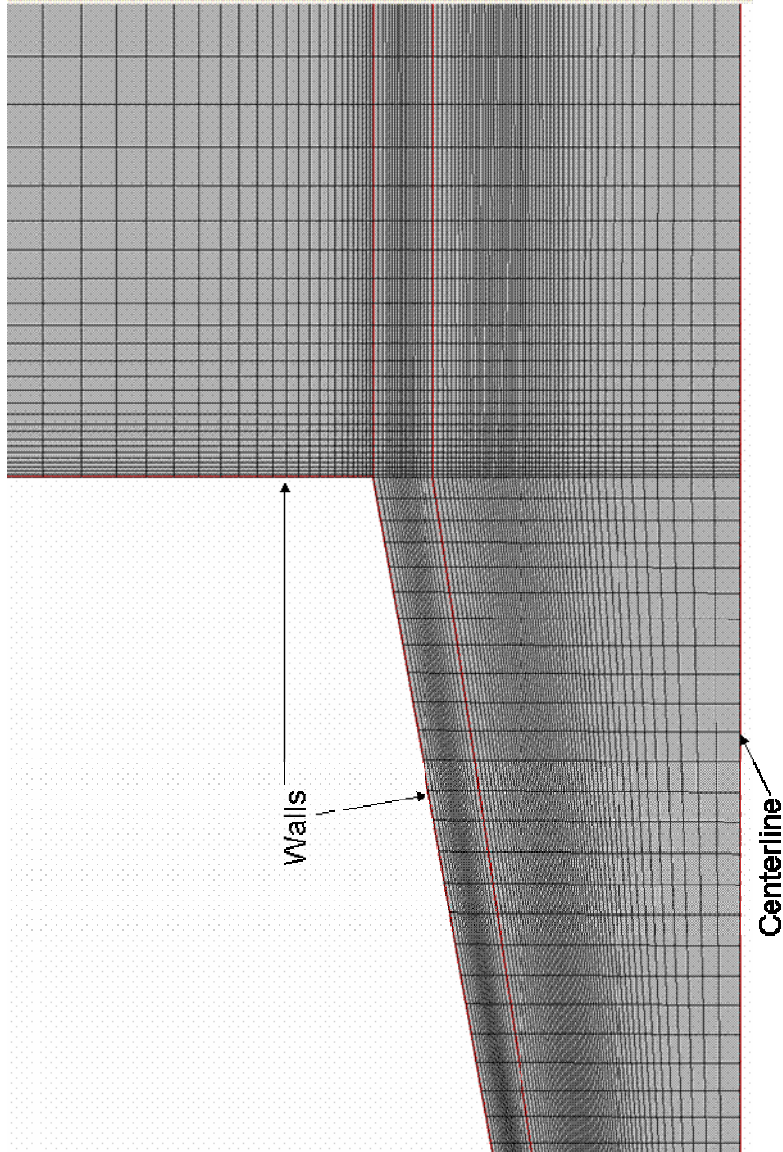
Figure 44.   Computational Grid for Internal Simulations: Grid Near Nozzle Exit

Grid spacing dimensions were much smaller near the walls and near the nozzle exit, logarithmically expanding in regions away from the walls or nozzle exit.
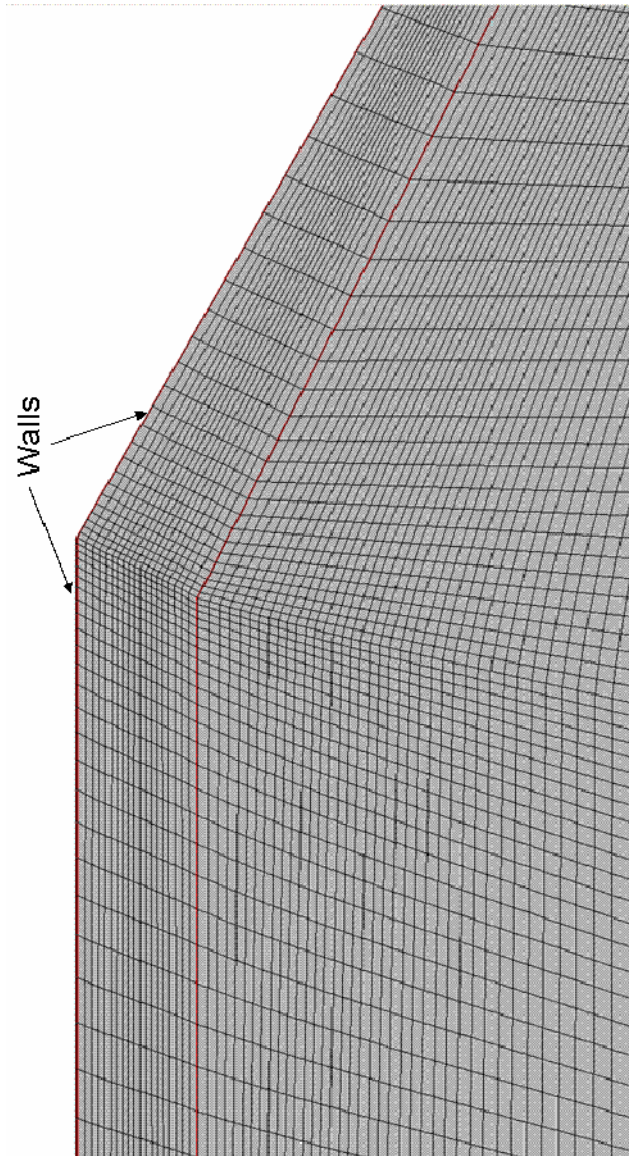
Figure 45.   Computational Grid for Internal Simulations: Grid at Converging Turn

Grid spacing was also reduced near the chamber walls and near the beginning of the converging section of the nozzle.
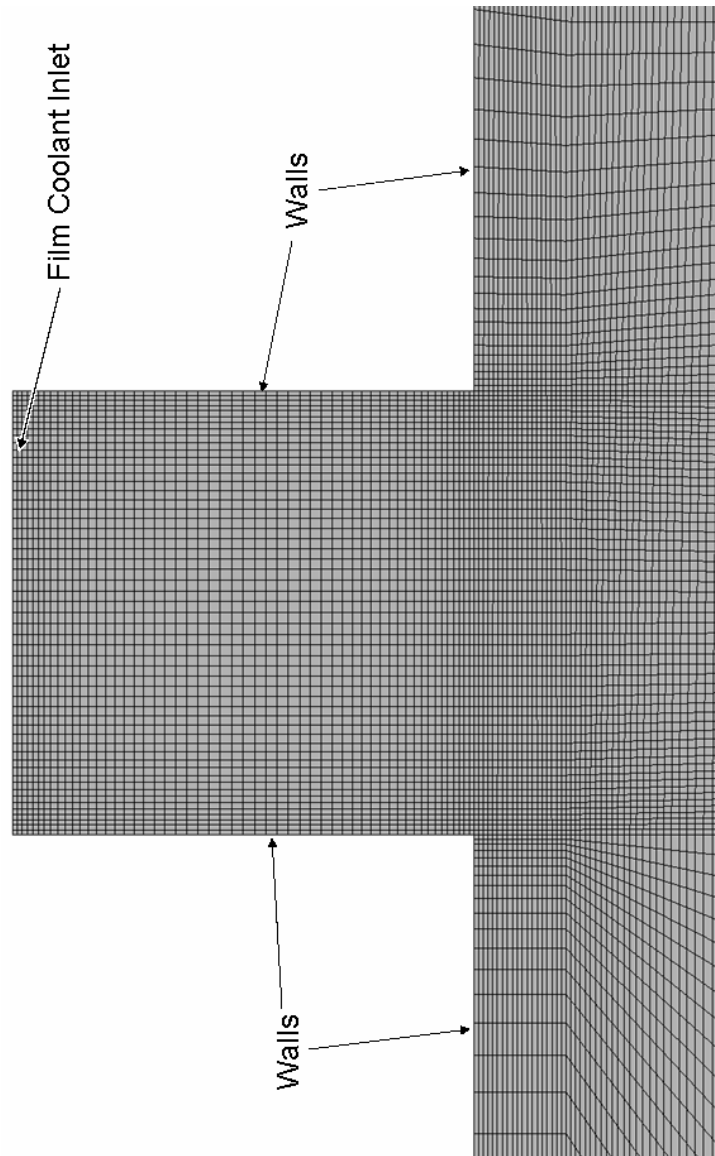
Figure 46.   Computational Grid for Internal Simulations: Grid at Film Inlet
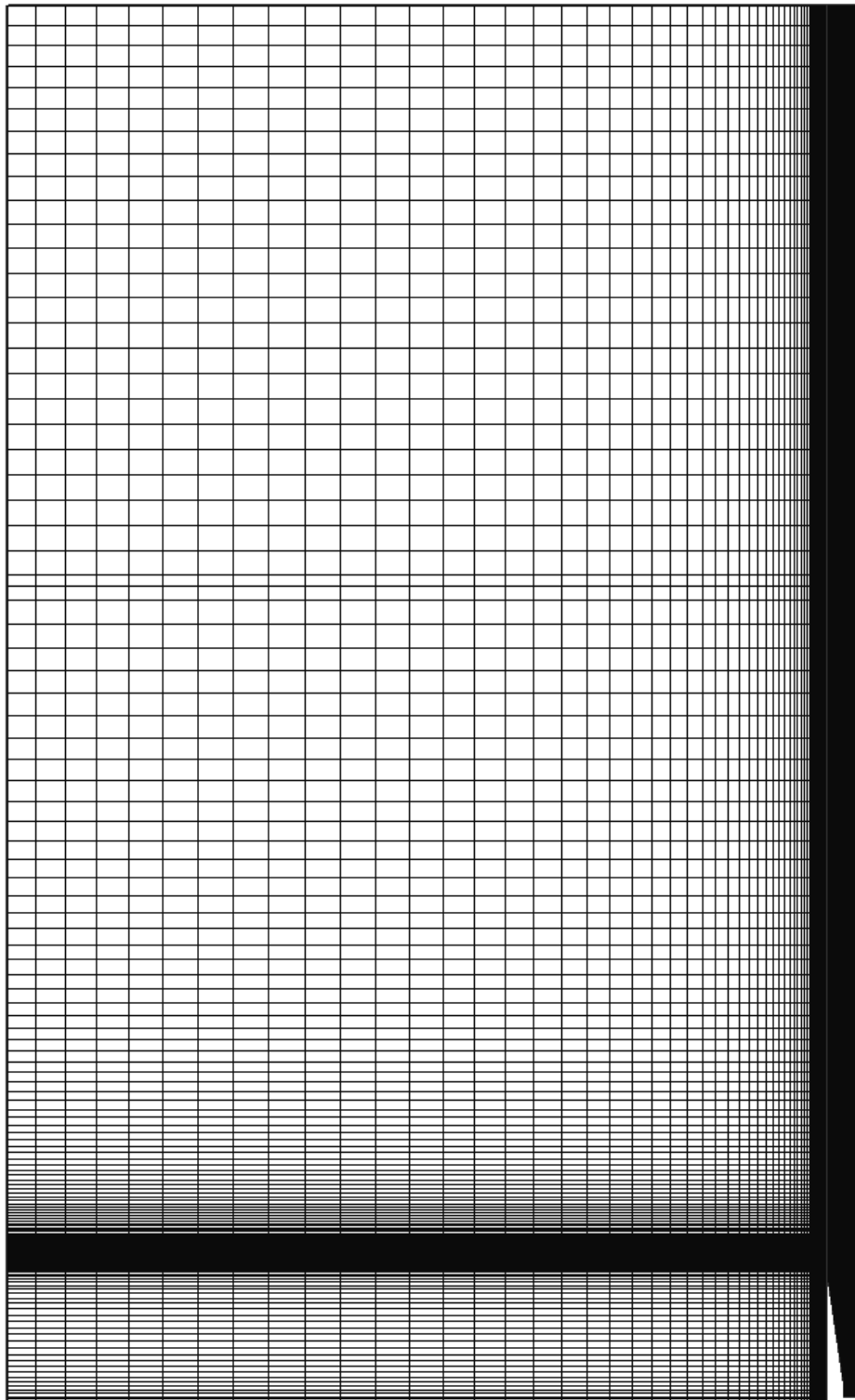
Figure 47.   Computational Domain for External Simulations
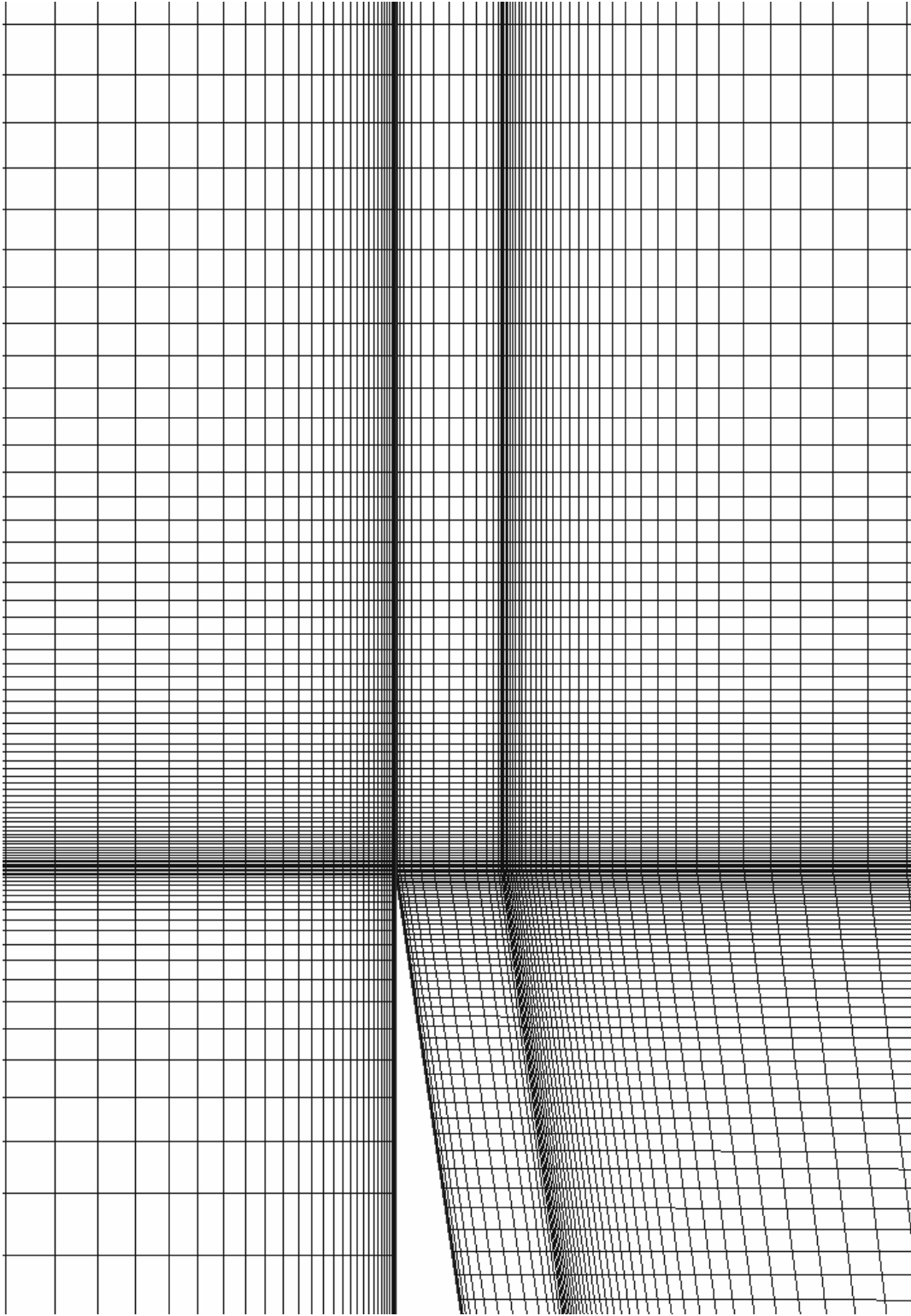
Figure 48.   Computational Grid for External Simulations: Near Nozzle Lip
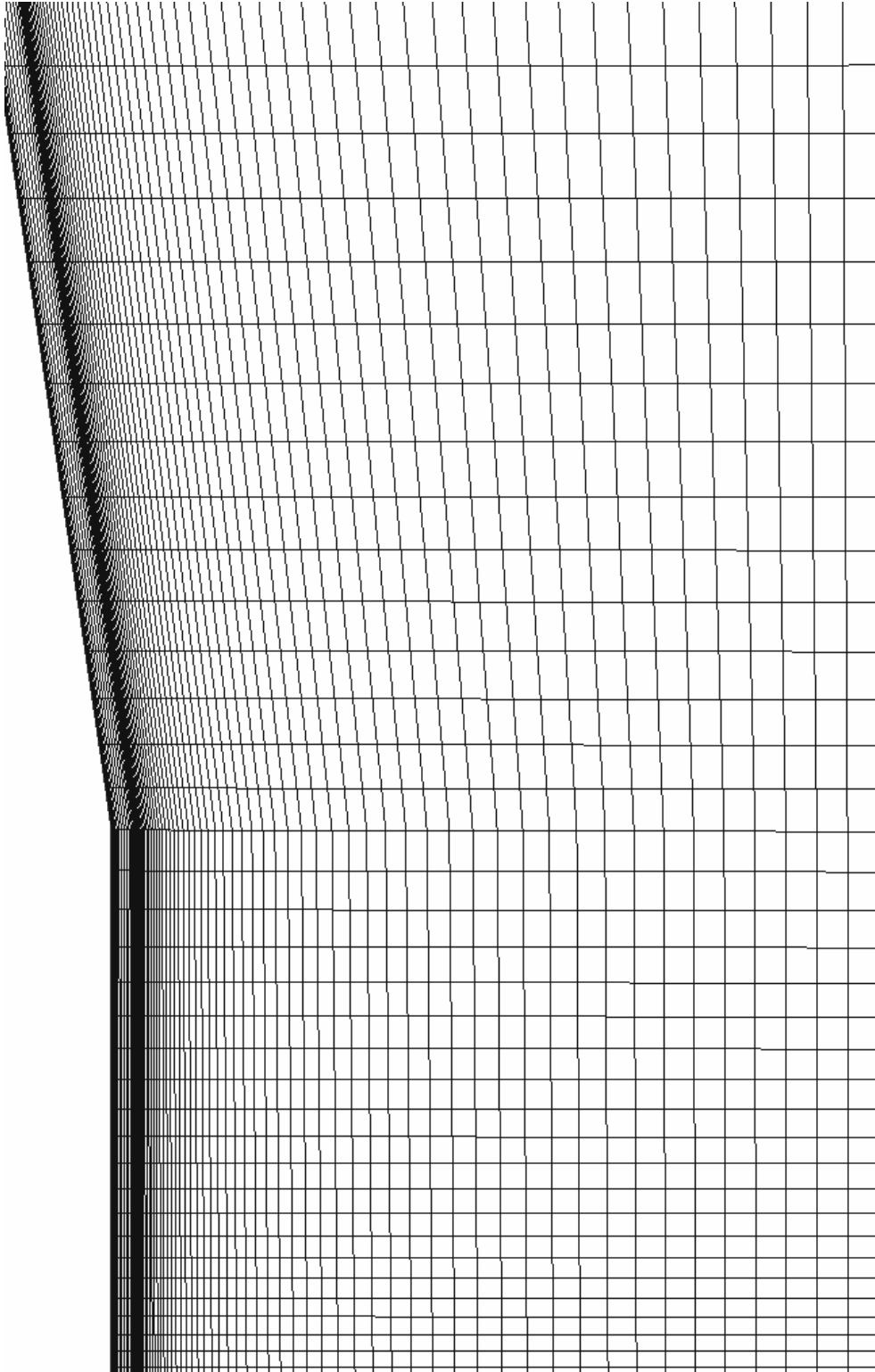
Figure 49.   Computational Grid for External Simulations: Nozzle Throat

THIS PAGE INTENTIONALLY LEFT BLANK

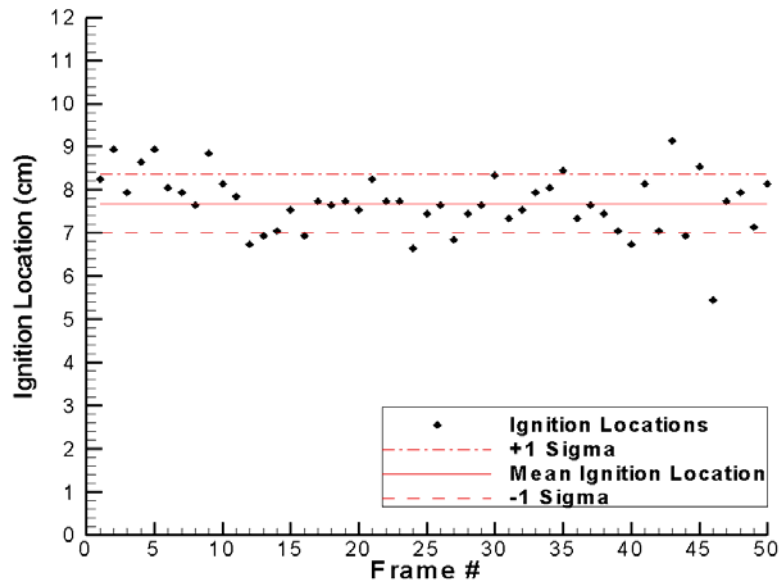# APPENDIX B. IGNITION LOCATION DATA

A.   KEROSENE FILM COOLING
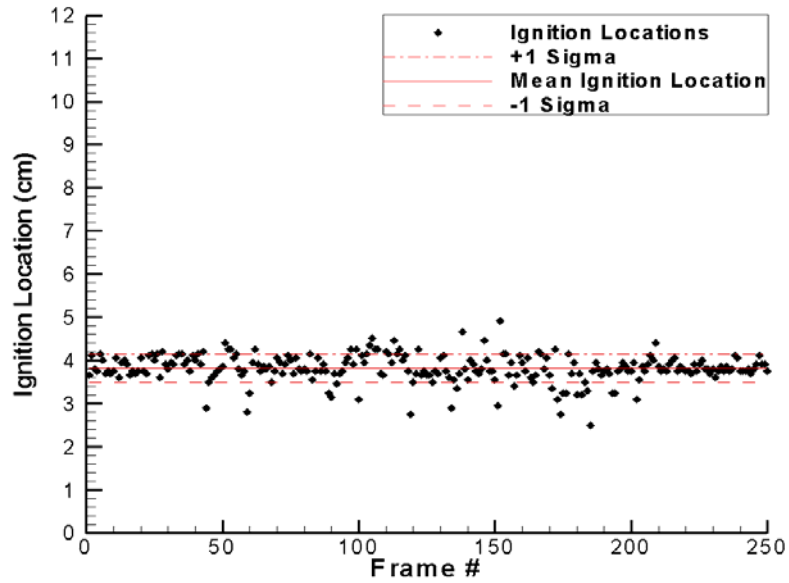
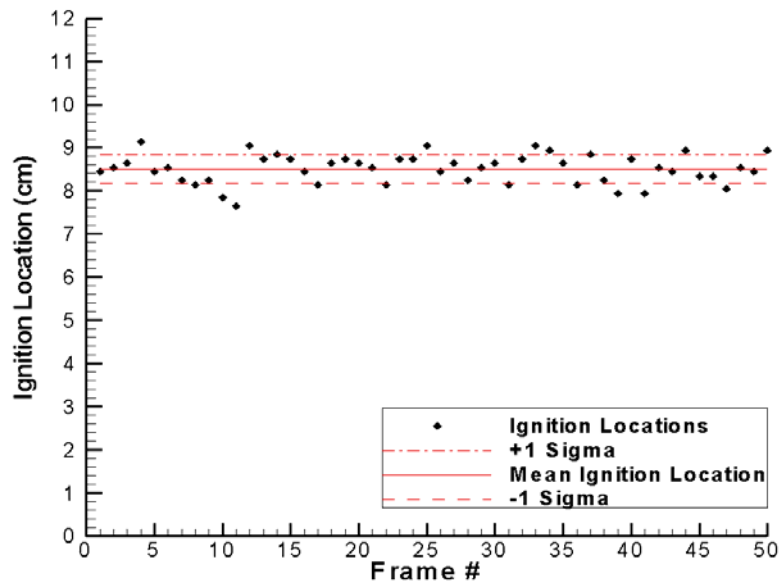Figure 50.   Ignition Locations: 0 m/s Air Velocity at 8.4% Kerosene Film Cooling
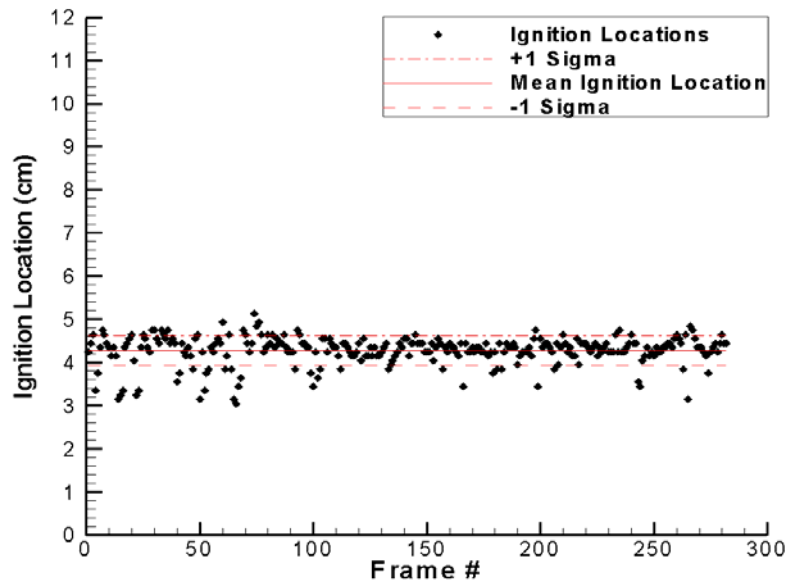
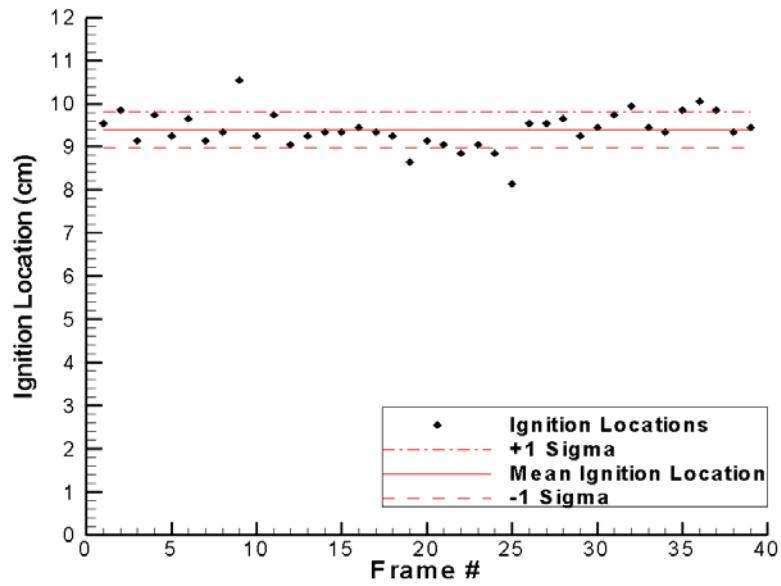Figure 51.   Ignition Locations: 50 m/s Air Velocity at 8.4% Kerosene Film Cooling
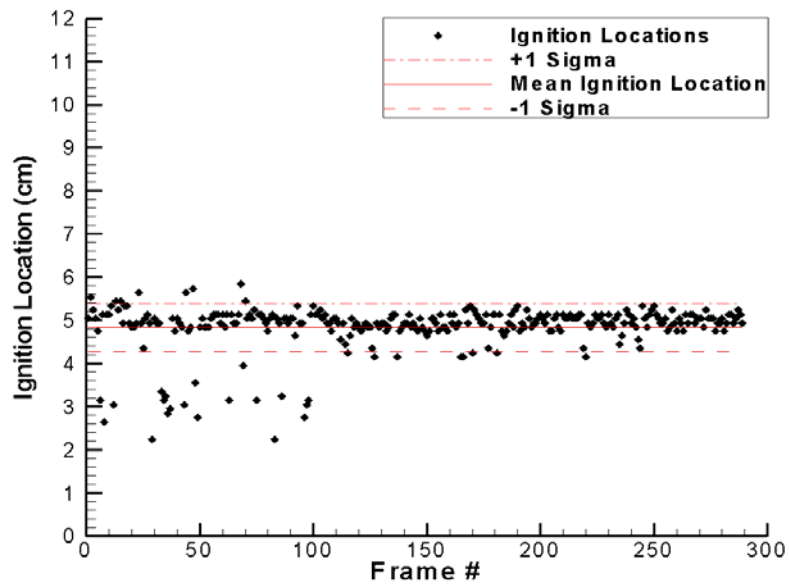
Figure 52.   Ignition Locations: 96 m/s Air Velocity at 8.4% Kerosene Film Cooling
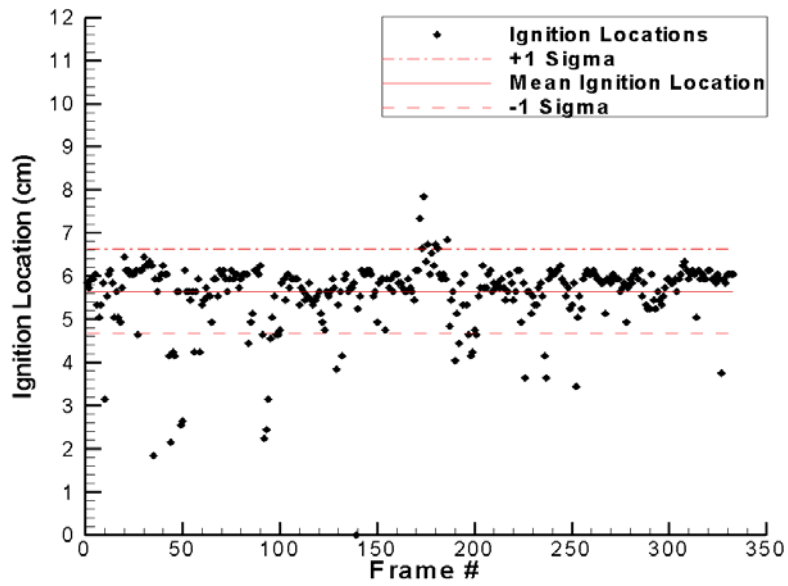
Figure 53.   Ignition Locations: 182 m/s Air Velocity at 8.4% Kerosene Film Cooling
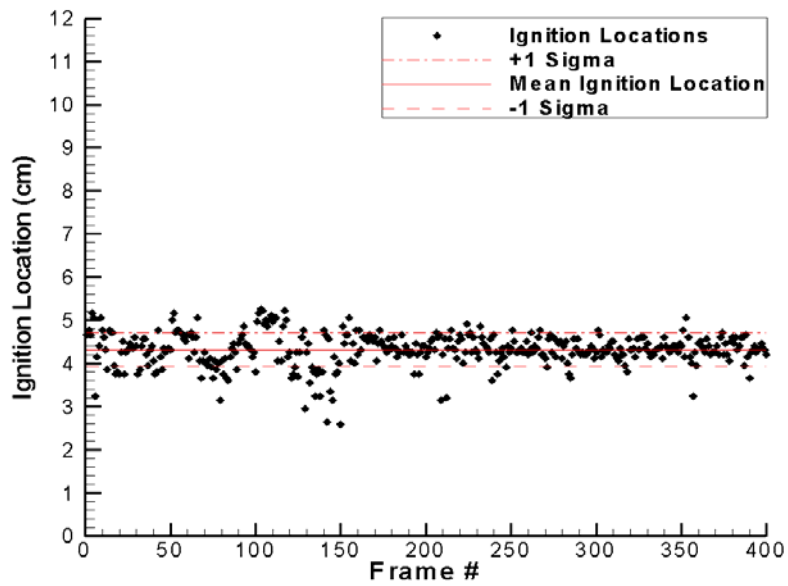
Figure 54.   Ignition Locations: 0 m/s Air Velocity at 10% Kerosene Film Cooling
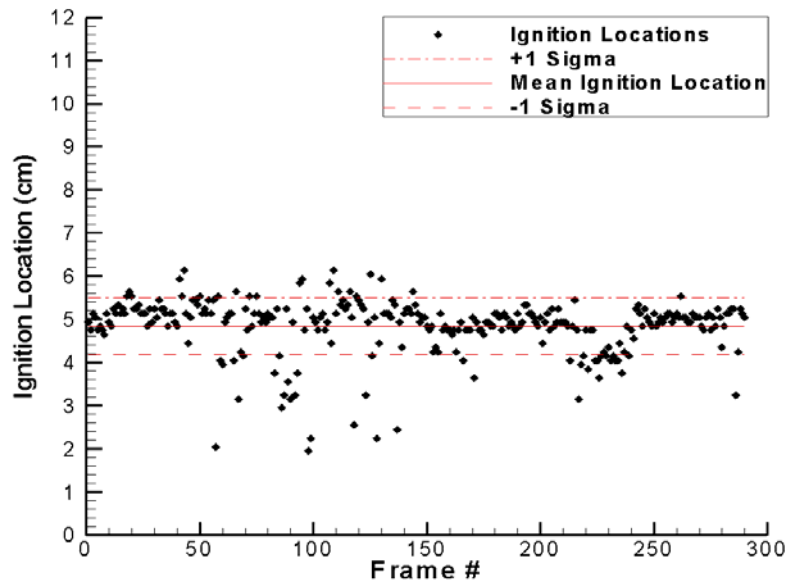
Figure 55.   Ignition Locations: 50 m/s Air Velocity at 10% Kerosene Film Cooling
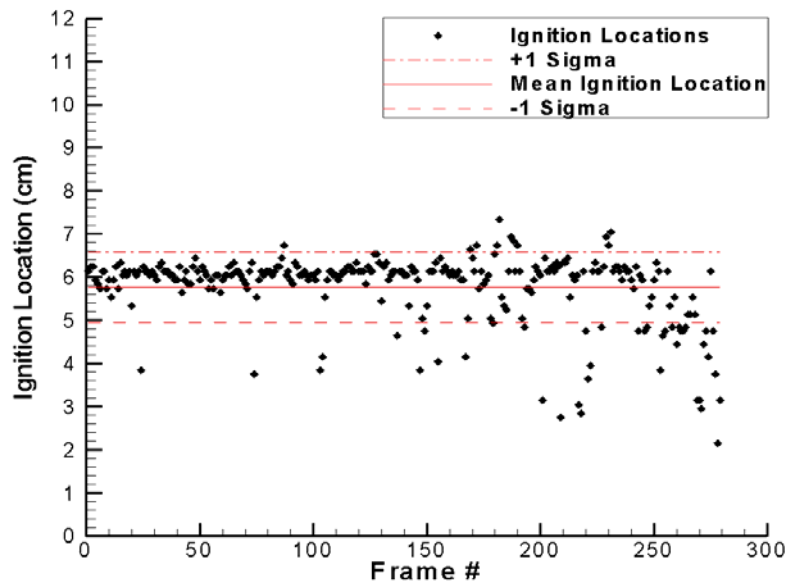
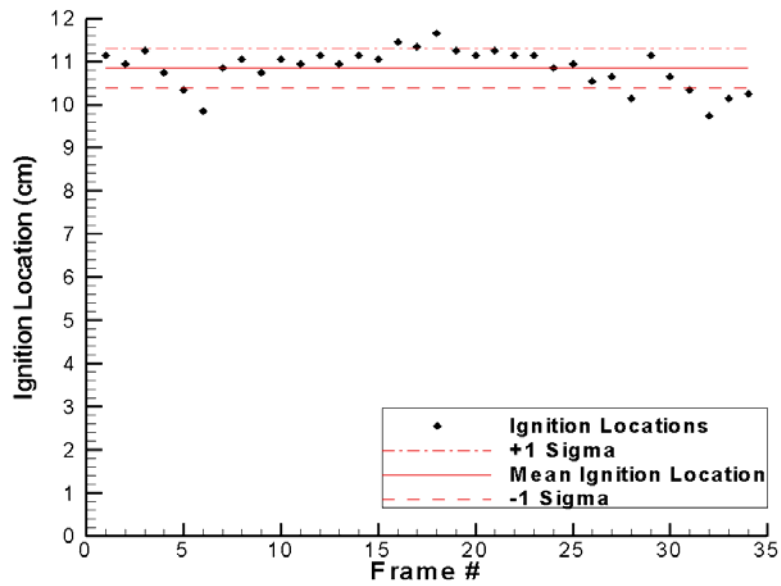Figure 56.   Ignition Locations: 96 m/s Air Velocity at 10% Kerosene Film Cooling
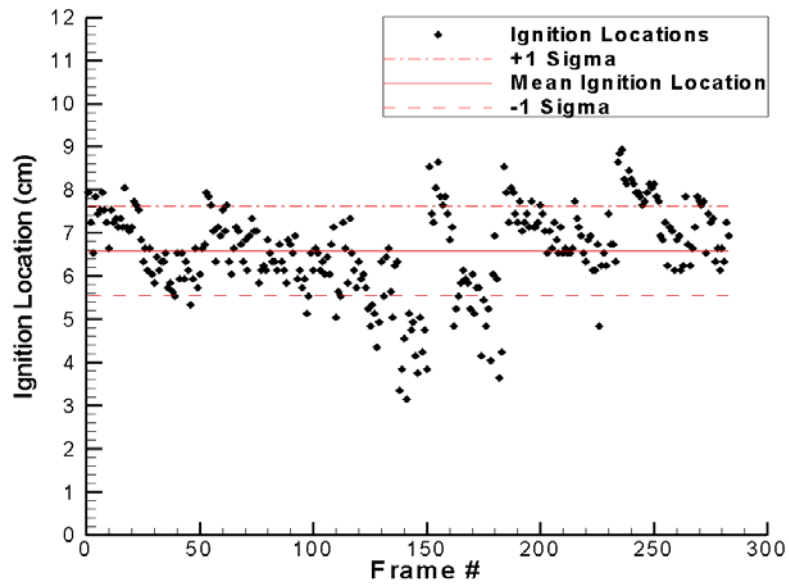
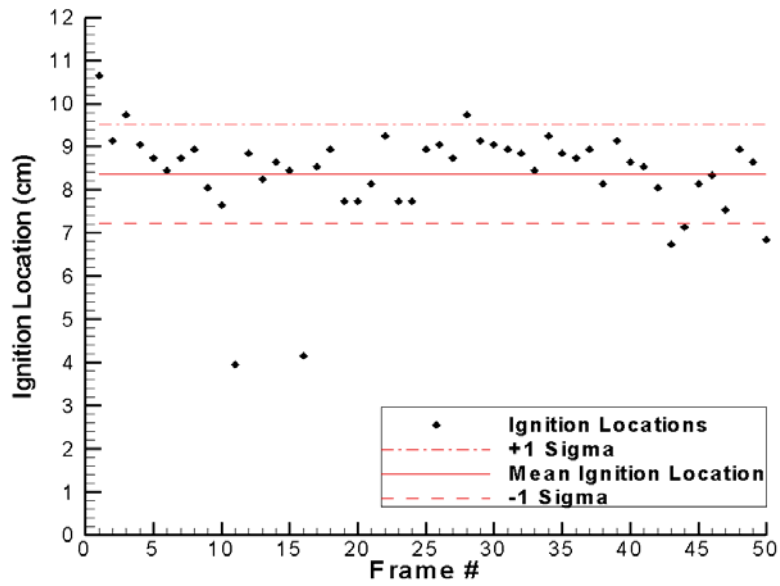Figure 57.   Ignition Locations: 182 m/s Air Velocity at 10% Kerosene Film Cooling
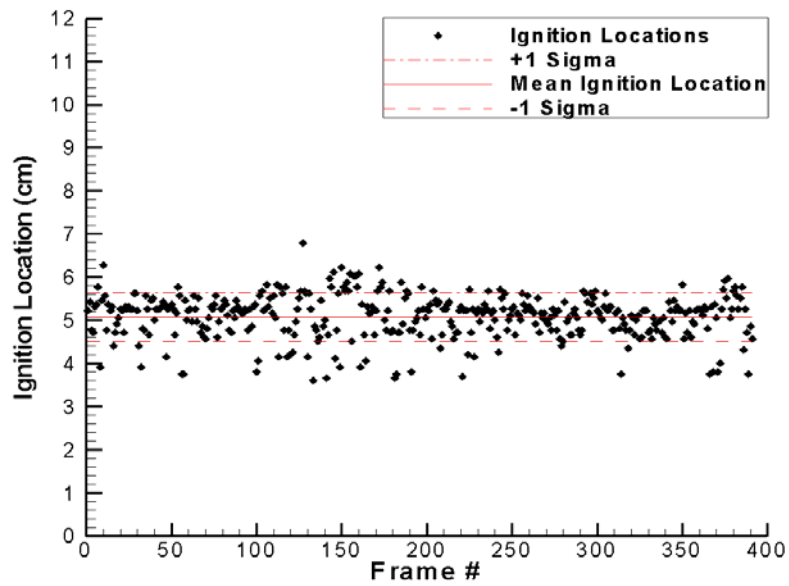
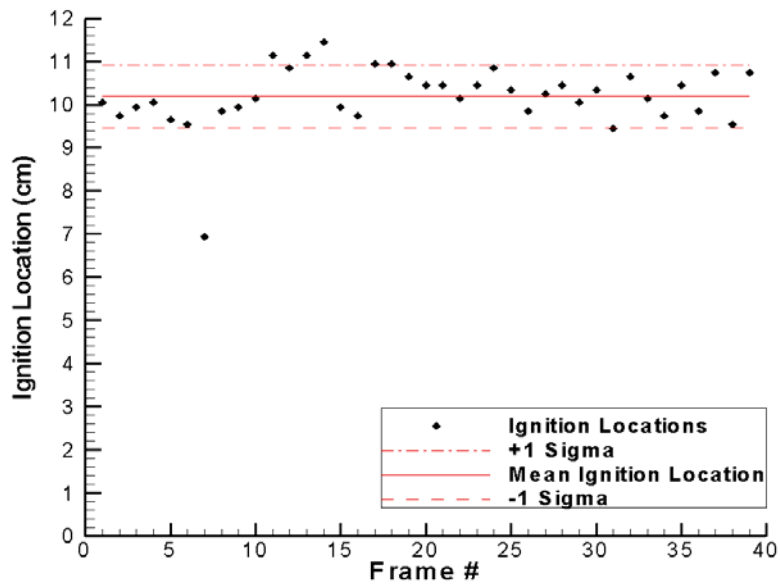Figure 58.   Ignition Locations: 0 m/s Air Velocity at 16% Kerosene Film Cooling

85
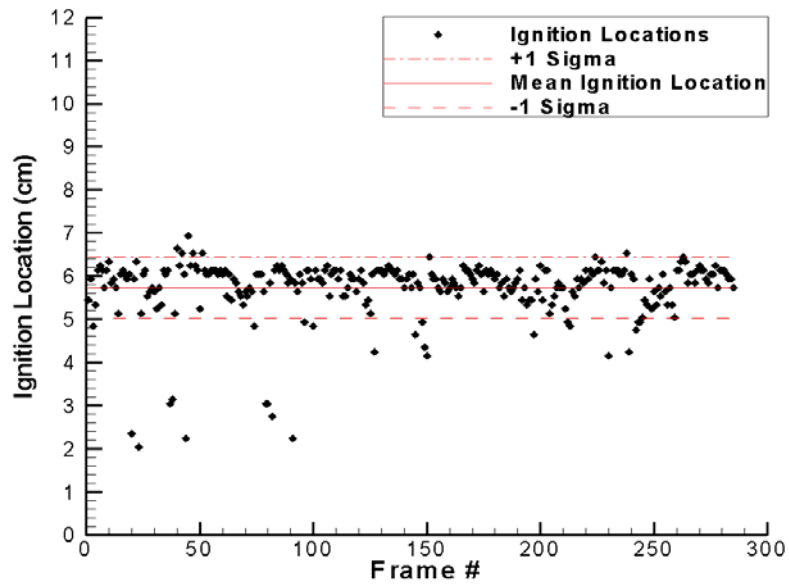
Figure 59.   Ignition Locations: 50 m/s Air Velocity at 16% Kerosene Film Cooling
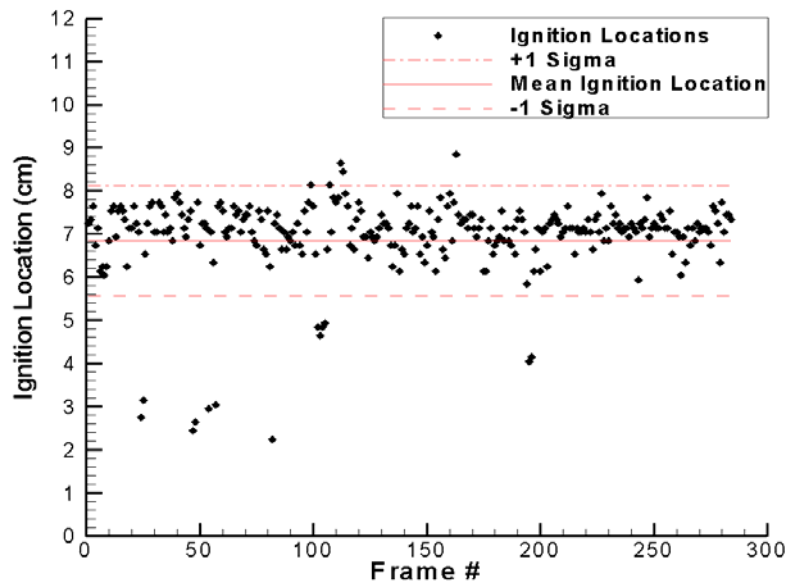
Figure 60.   Ignition Locations: 96 m/s Air Velocity at 16% Kerosene Film Cooling

B. ETHANOL FILM COOLING
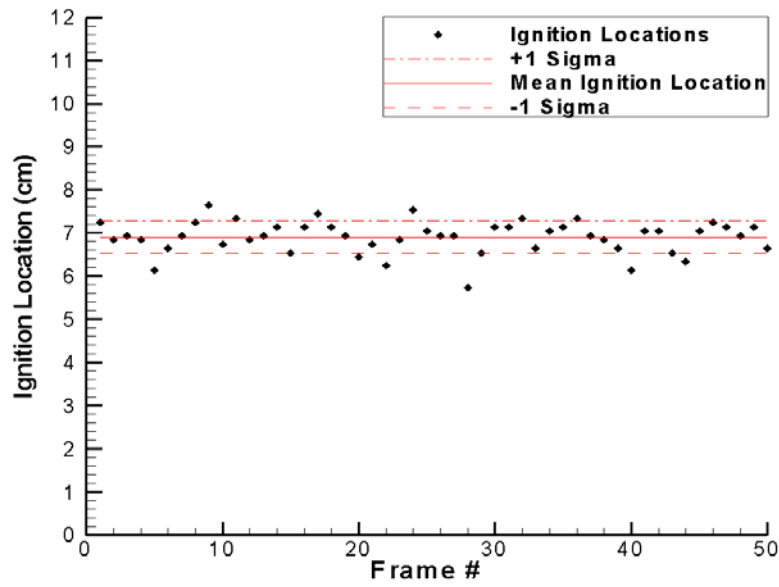
Figure 61.   Ignition Locations: 0 m/s Air Velocity at 9.0% Ethanol Film Cooling
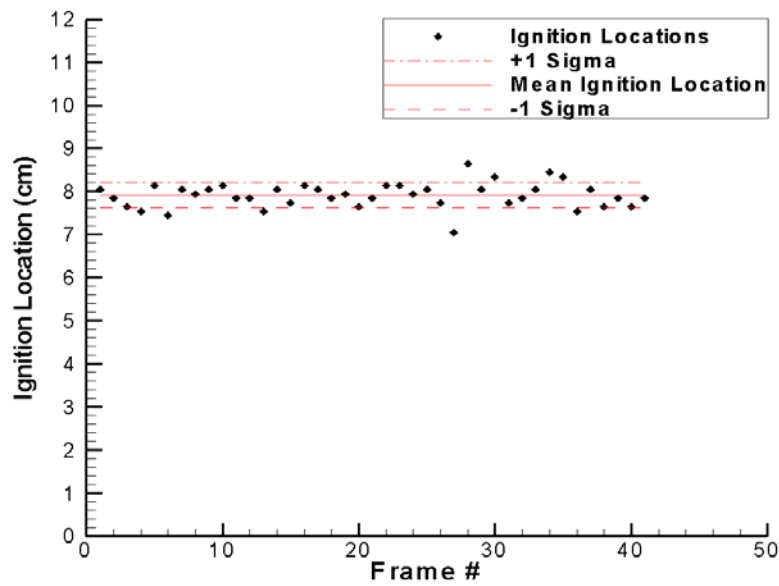
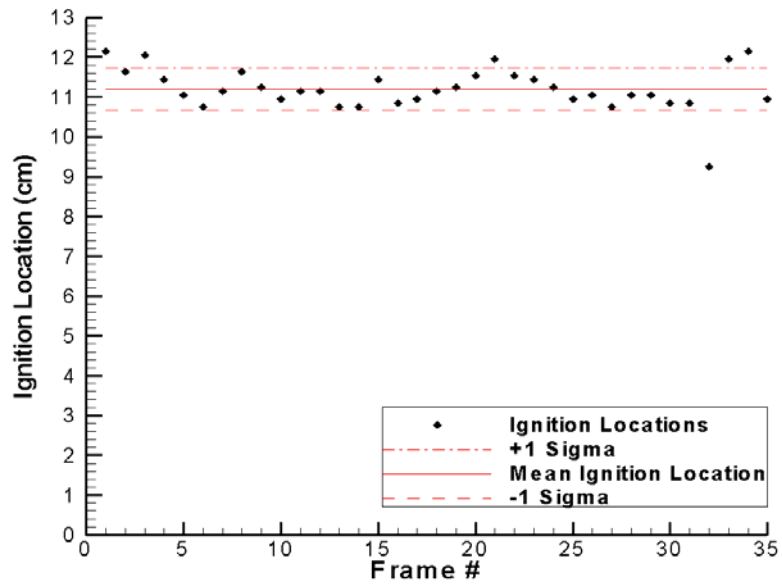Figure 62.   Ignition Locations: 50 m/s Air Velocity at 9.0% Ethanol Film Cooling
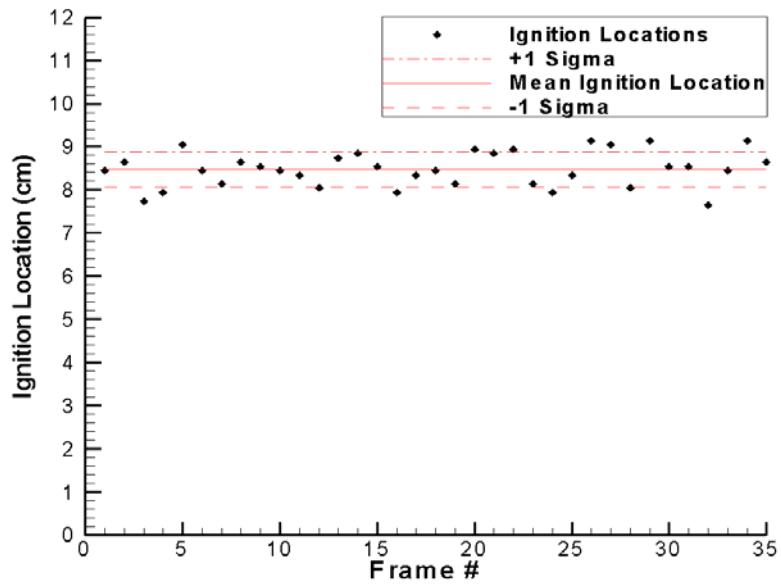
Figure 63.   Ignition Locations: 96 m/s Air Velocity at 9.0% Ethanol Film Cooling
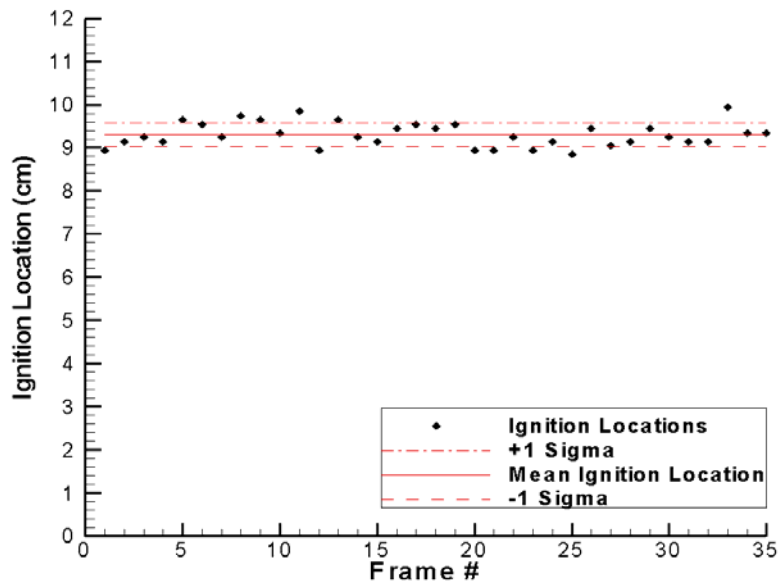
Figure 64.   Ignition Locations: 182 m/s Air Velocity at 9.0% Ethanol Film Cooling
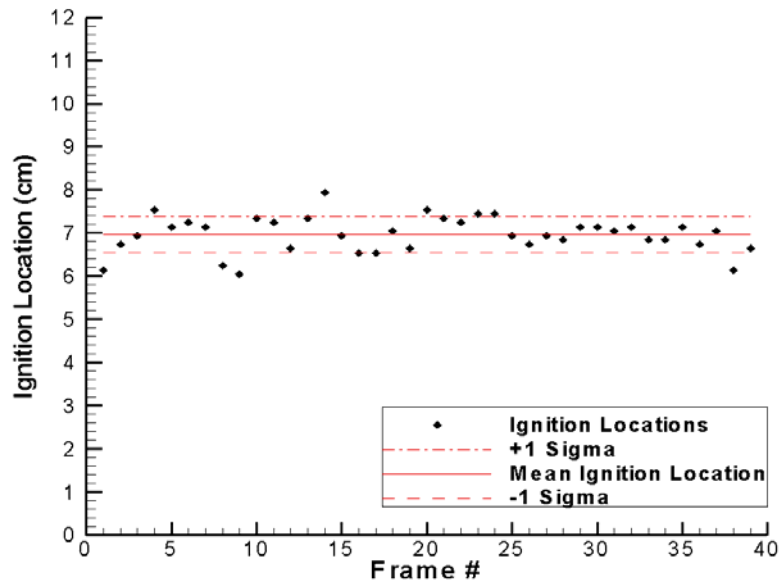
Figure 65.   Ignition Locations: 0 m/s Air Velocity at 11% Ethanol Film Cooling
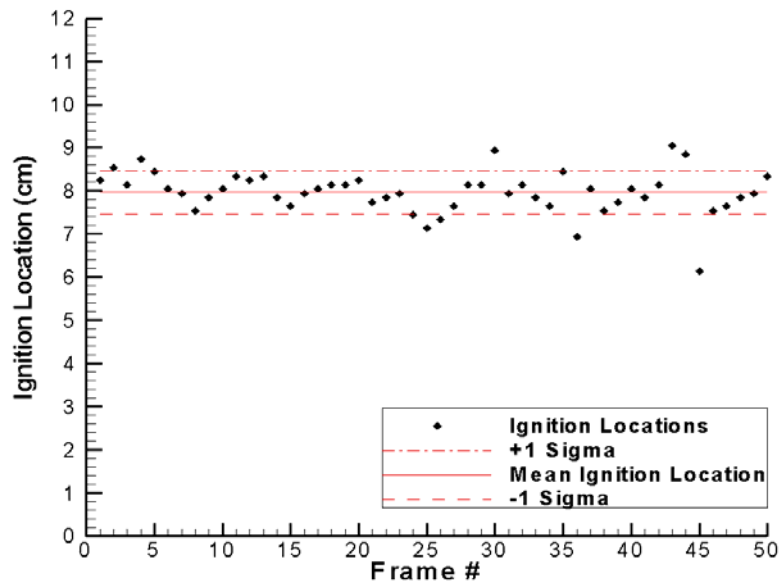
Figure 66.   Ignition Locations: 50 m/s Air Velocity at 11% Ethanol Film Cooling
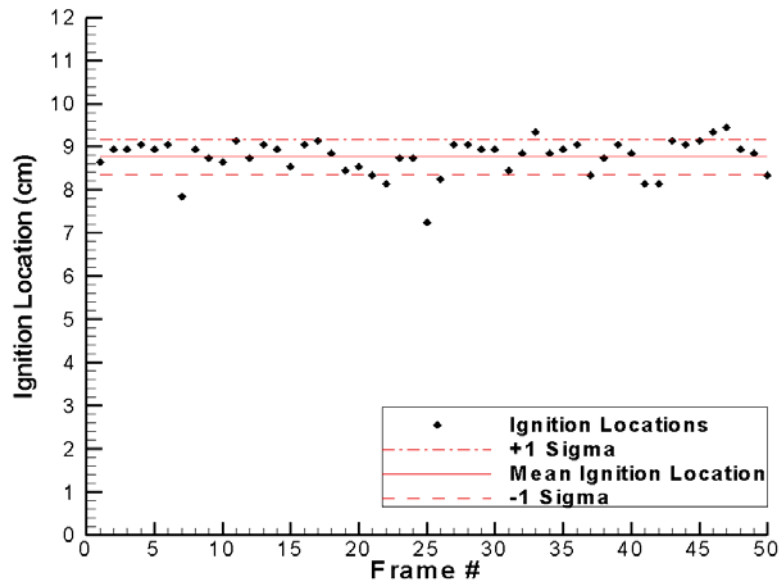
Figure 67.   Ignition Locations: 96 m/s Air Velocity at 11% Ethanol Film Cooling
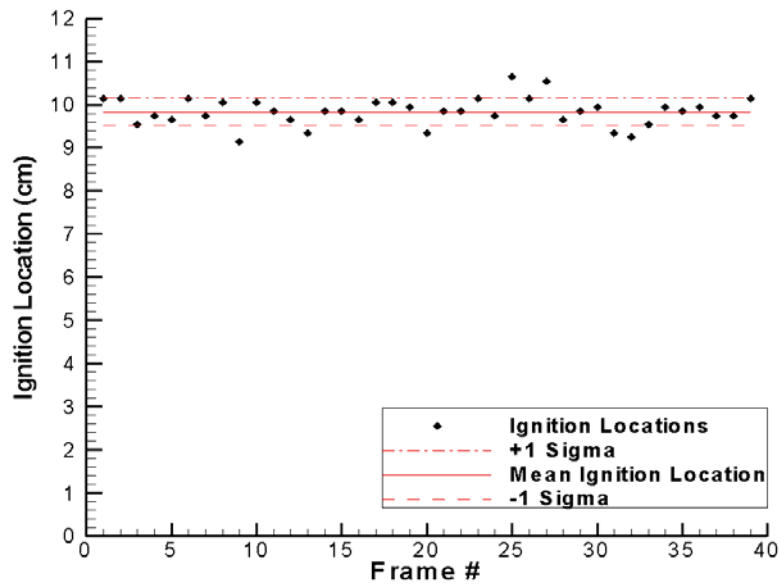
Figure 68.   Ignition Locations: 182 m/s Air Velocity at 11% Ethanol Film Cooling
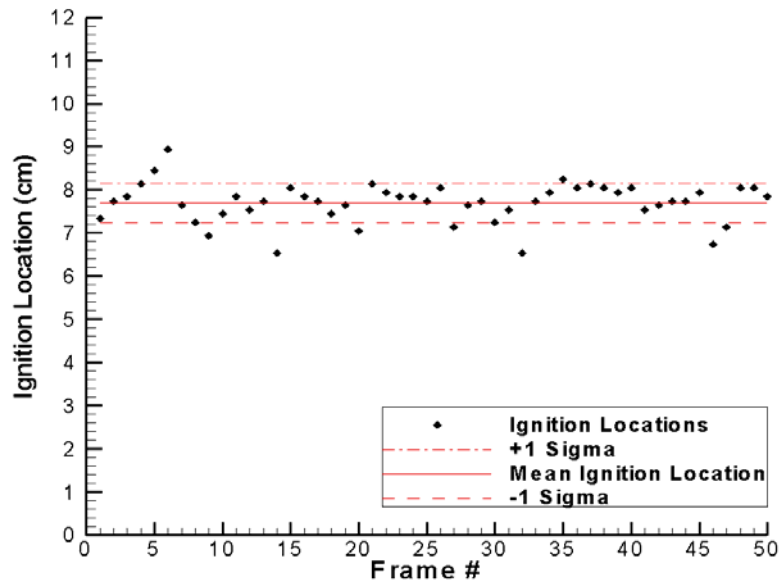
Figure 69.　Ignition Locations: 0 m/s Air Velocity at 17% Ethanol Film Cooling
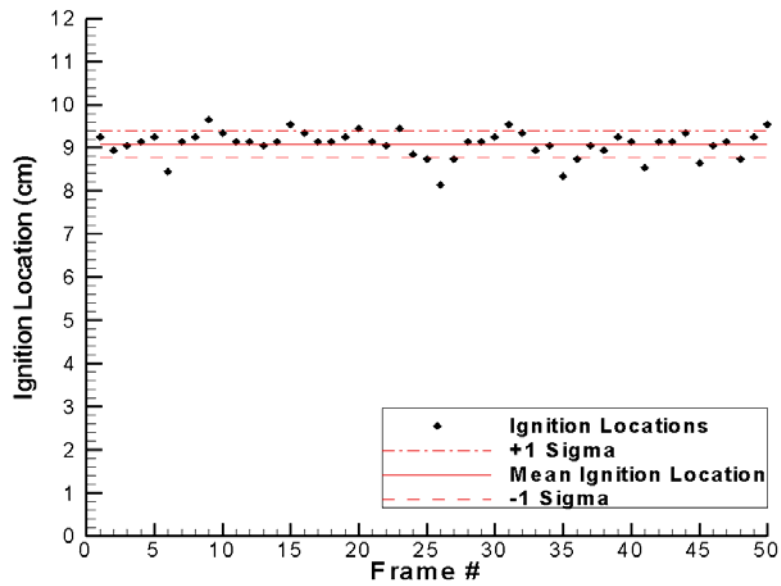
Figure 70.　Ignition Locations: 50 m/s Air Velocity at 17% Ethanol Film Cooling
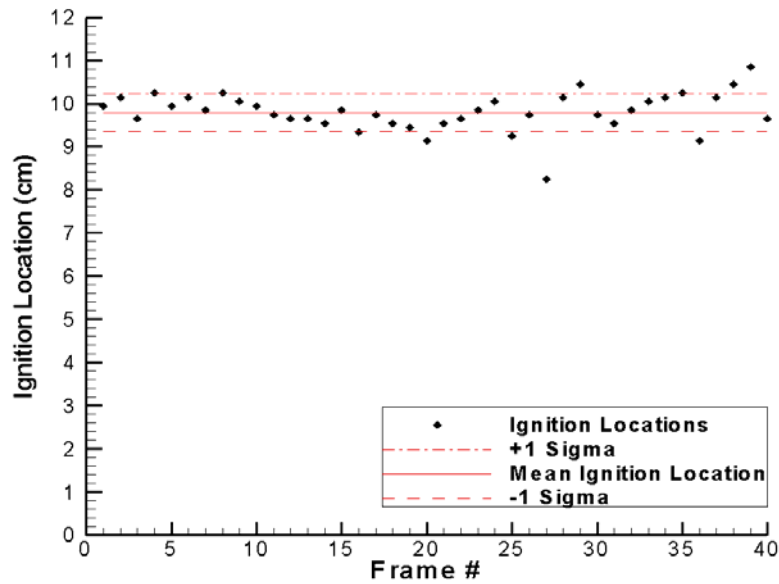
Figure 71.   Ignition Locations: 96 m/s Air Velocity at 17% Ethanol Film Cooling

C.   WATER FILM COOLING

This data is included for archival purposes only, and is not referenced in the text.

Table 13. Ignition Location Summary: Water Film Coolant				
Film Cooling Percentage	Airspeed	Mean Ignition Location (in.)	Standard Deviation (in.)	Number of Data Points
8.95%	0 m/s	2.914	0.303	50
	50.1 m/s	3.397	0.249	39
	96.5 m/s	3.511	0.193	42
	181.7 m/s	3.898	0.185	34
10.67%	0 m/s	3.027	0.272	50
	50.1 m/s	3.350	0.133	50
	96.5 m/s	3.696	0.165	39
	181.7 m/s	4.270	0.178	34
17.08%	0 m/s	3.296	0.451	50
	50.1 m/s	4.011	0.287	39
	96.5 m/s	4.407	0.209	36
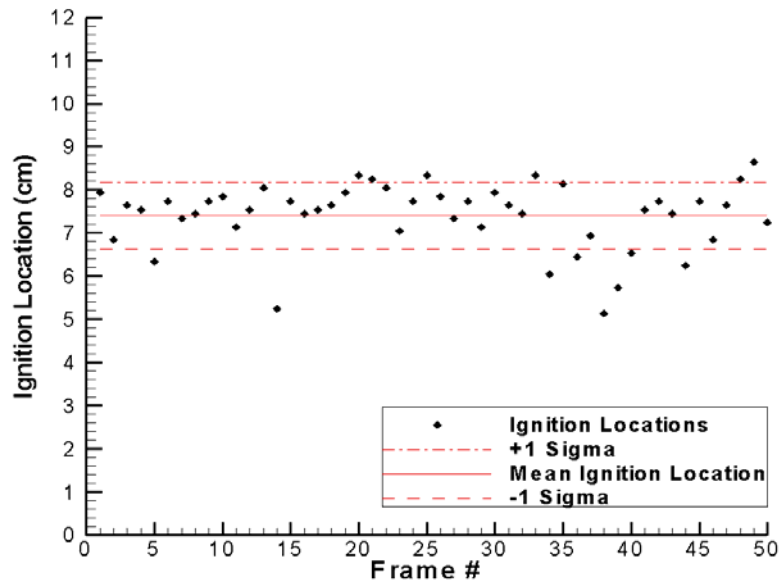
Figure 72.   Ignition Locations: 0 m/s Air Velocity at 9.0% Water Film Cooling
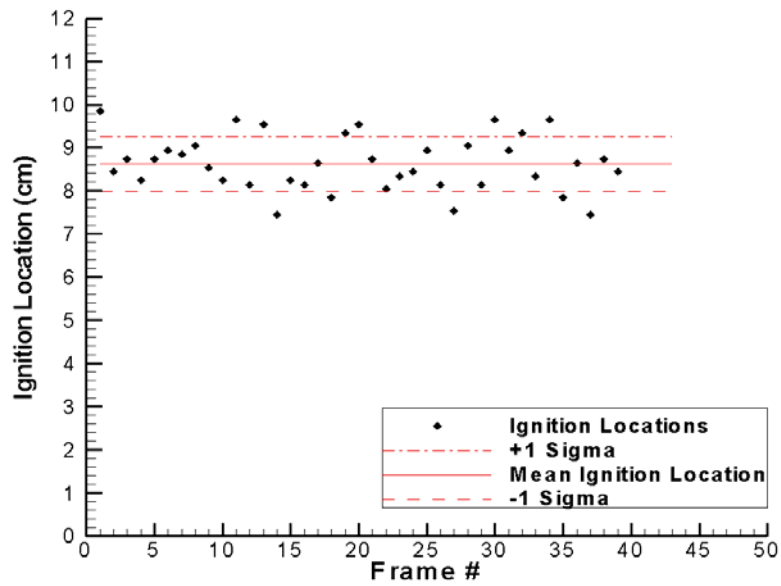
Figure 73.   Ignition Locations: 50 m/s Air Velocity at 9.0% Water Film Cooling
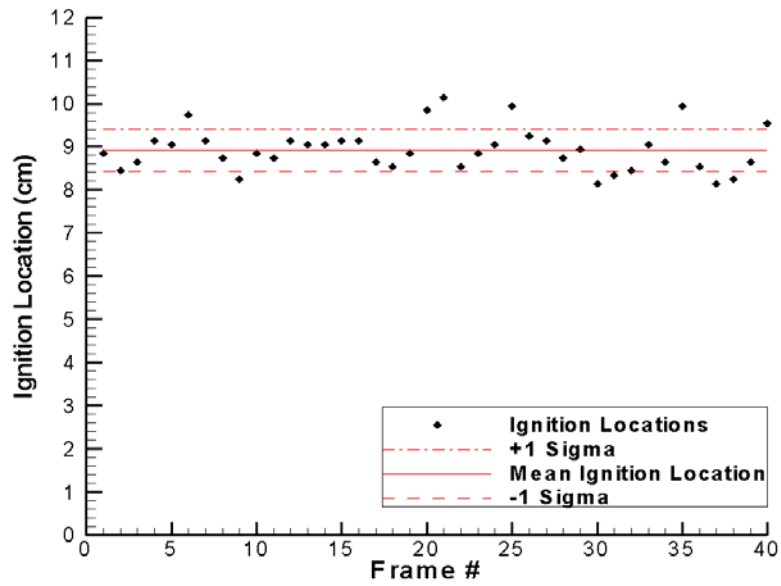
Figure 74.   Ignition Locations: 96 m/s Air Velocity at 9.0% Water Film Cooling
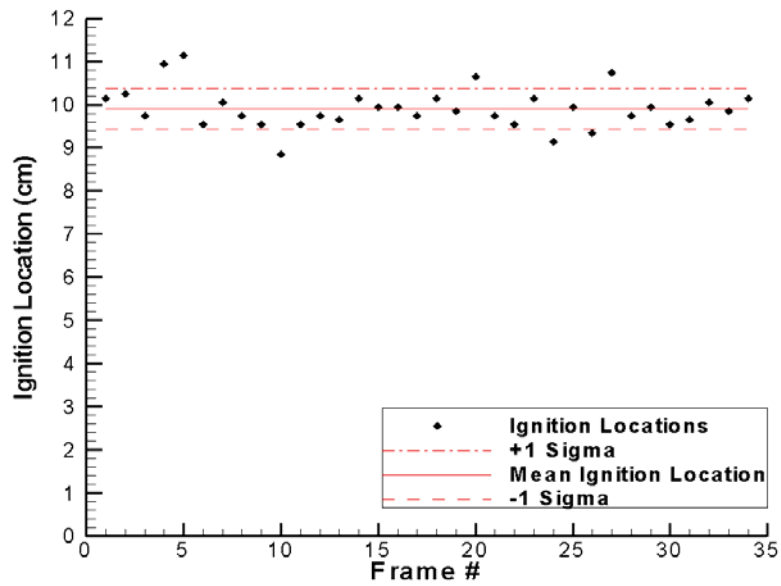
Figure 75.   Ignition Locations: 182 m/s Air Velocity at 9.0% Water Film Cooling

Figure 76.   Ignition Locations: 0 m/s Air Velocity at 11% Water Film Cooling

Figure 77.   Ignition Locations: 50 m/s Air Velocity at 11% Water Film Cooling

95

Figure 78.   Ignition Locations: 96 m/s Air Velocity at 11% Water Film Cooling

Figure 79.   Ignition Locations: 182 m/s Air Velocity at 11% Water Film Cooling

Figure 80.   Ignition Locations: 0 m/s Air Velocity at 17% Water Film Cooling

Figure 81.   Ignition Locations: 50 m/s Air Velocity at 17% Water Film Cooling

Figure 82.   Ignition Locations: 96 m/s Air Velocity at 17% Water Film Cooling

APPENDIX C. DETAIL DRAWINGS FOR EXPERIMENTAL HARDWARE
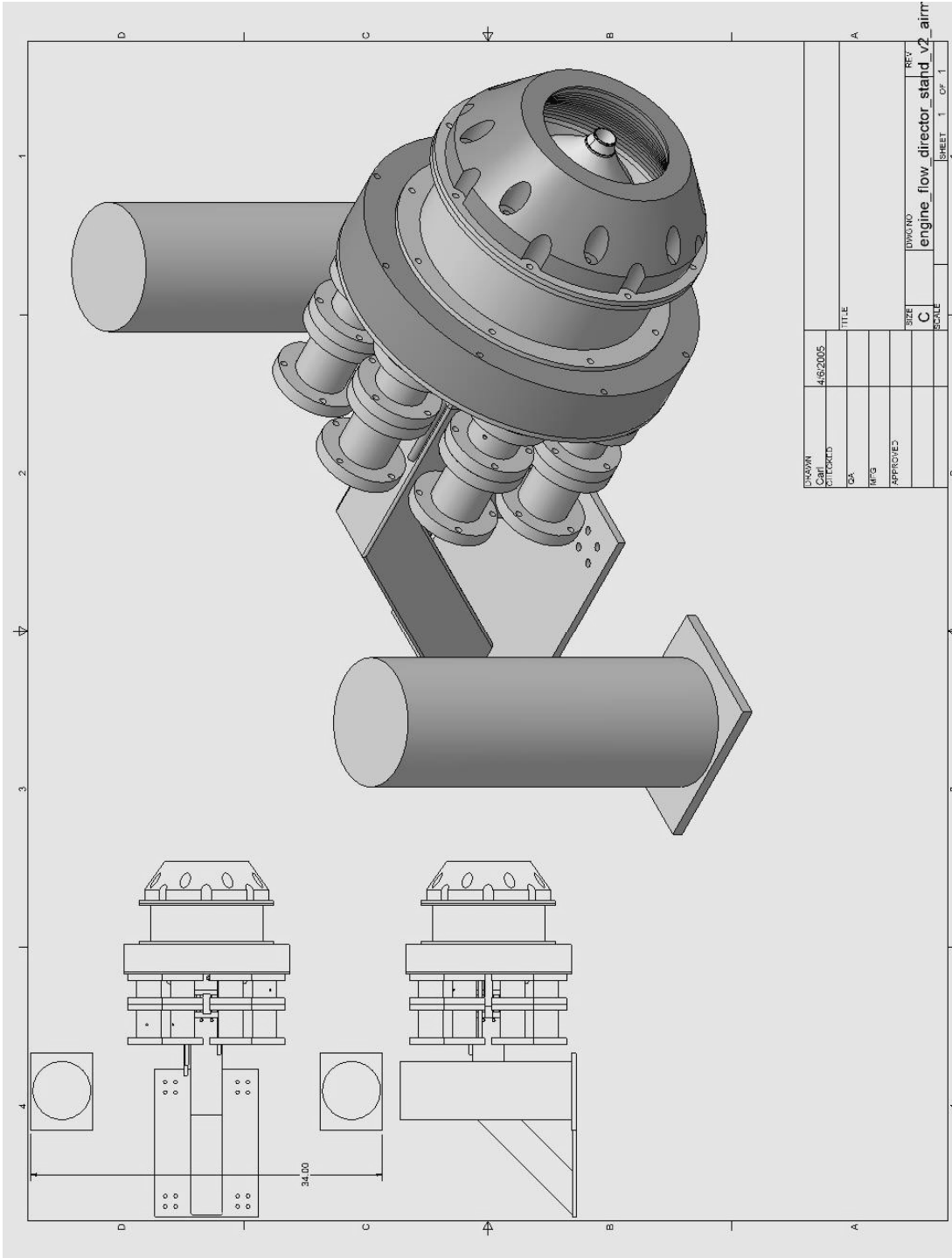
Figure 83.   Assembled View of Rocket, Stand, Airflow Director and Air Manifolds

A.   ROCKET ENGINE COMPONENTS

Figure 84.   Rocket Engine Assembly

Figure 85.   Injector Housing

101

Figure 86.   Injector (Hastelloy)

SECTION F-F
SCALE 1 / 2

.550
.500
.500
F
E
F
E
.550

VIEW E-E
SCALE 1 / 2

ø.500
.525
1.577
135.0°
ø.313
ø2.800

SECTION A-A
SCALE 1 / 2

ø3.500
ø2.123
.050
.095
.560
.200
1.000
ø2.057
2.000
.095
.560
.250
.050
ø2.002
ø2.114
ø2.254

SECTION C-C
SCALE 1 / 2
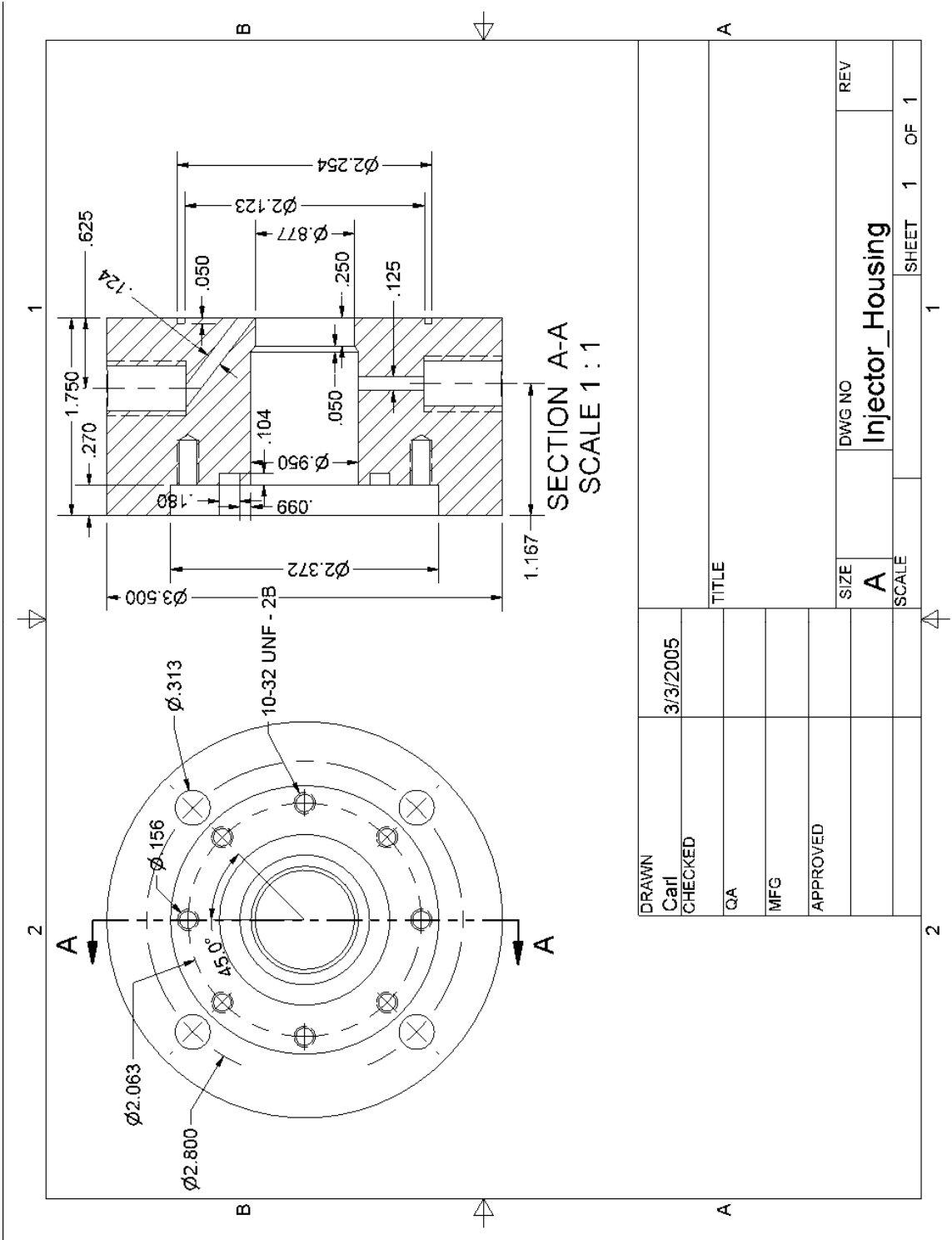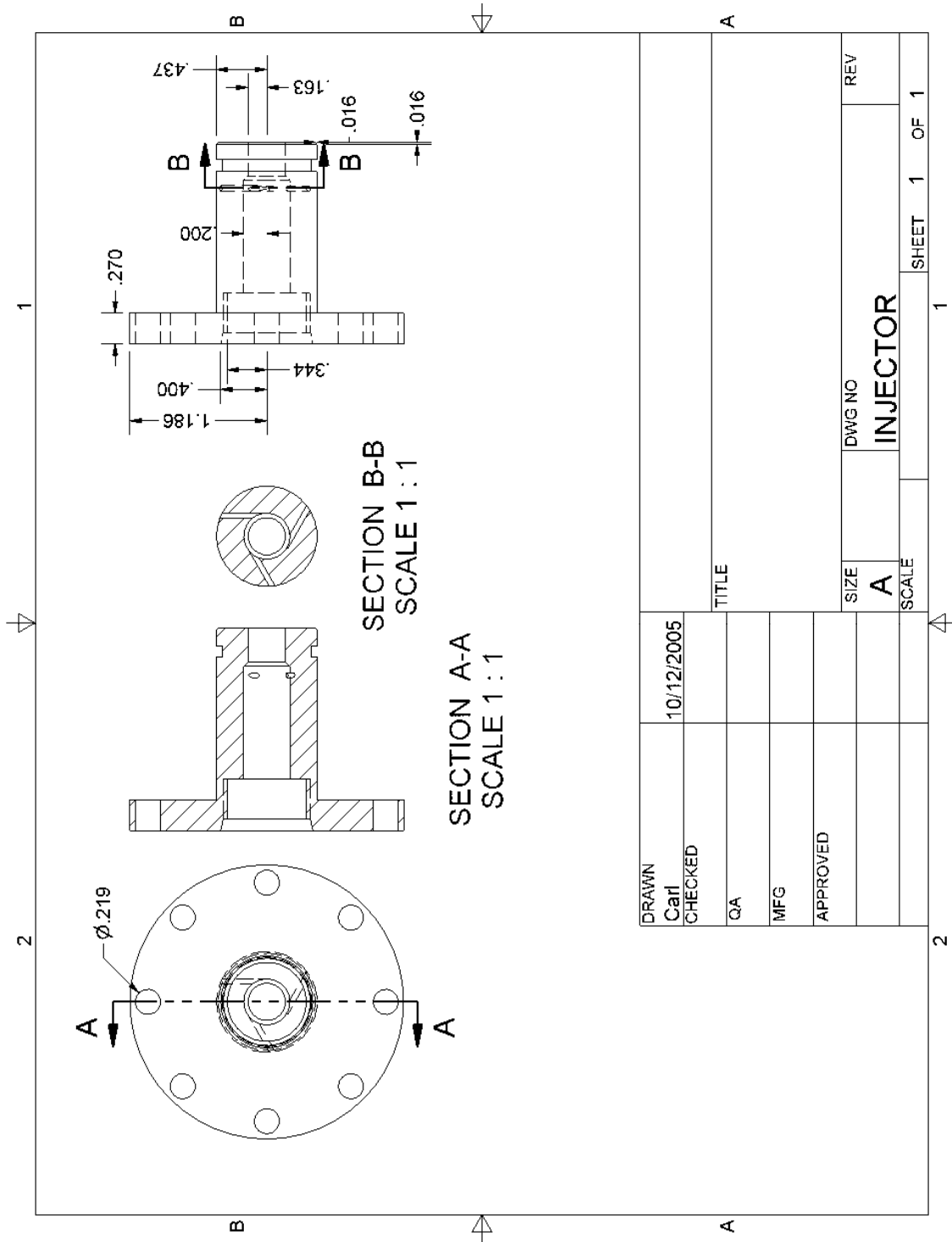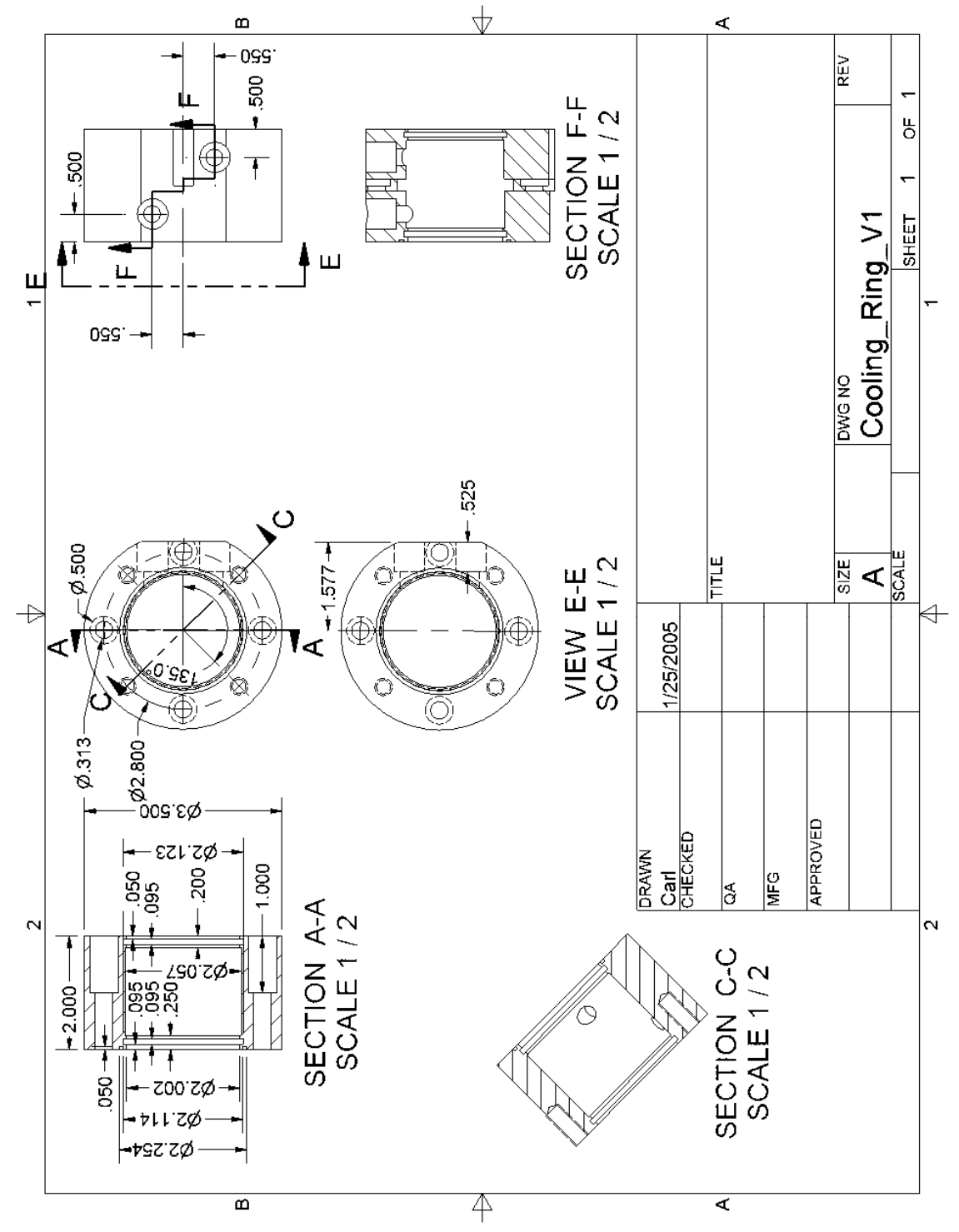
Figure 87.   Rocket Segment/Housing (View 1)

SECTION A-A
SCALE 1 : 1

Ø3.500
.050
.200
.095
.060
Ø2.057
1.000
.050
Ø2.123
.095
.060
.250
2.000
Ø2.002
Ø2.114
Ø2.254
5/16-18 UNC - 1B

Ø.500
Ø.313
Ø2.800
45.0°

A2
A

DRAWN Carl 1/31/2005
CHECKED
QA
MFG
APPROVED
TITLE
SIZE A
DWG NO Cooling_Ring_V1-1
REV
SCALE
SHEET 1 OF 1
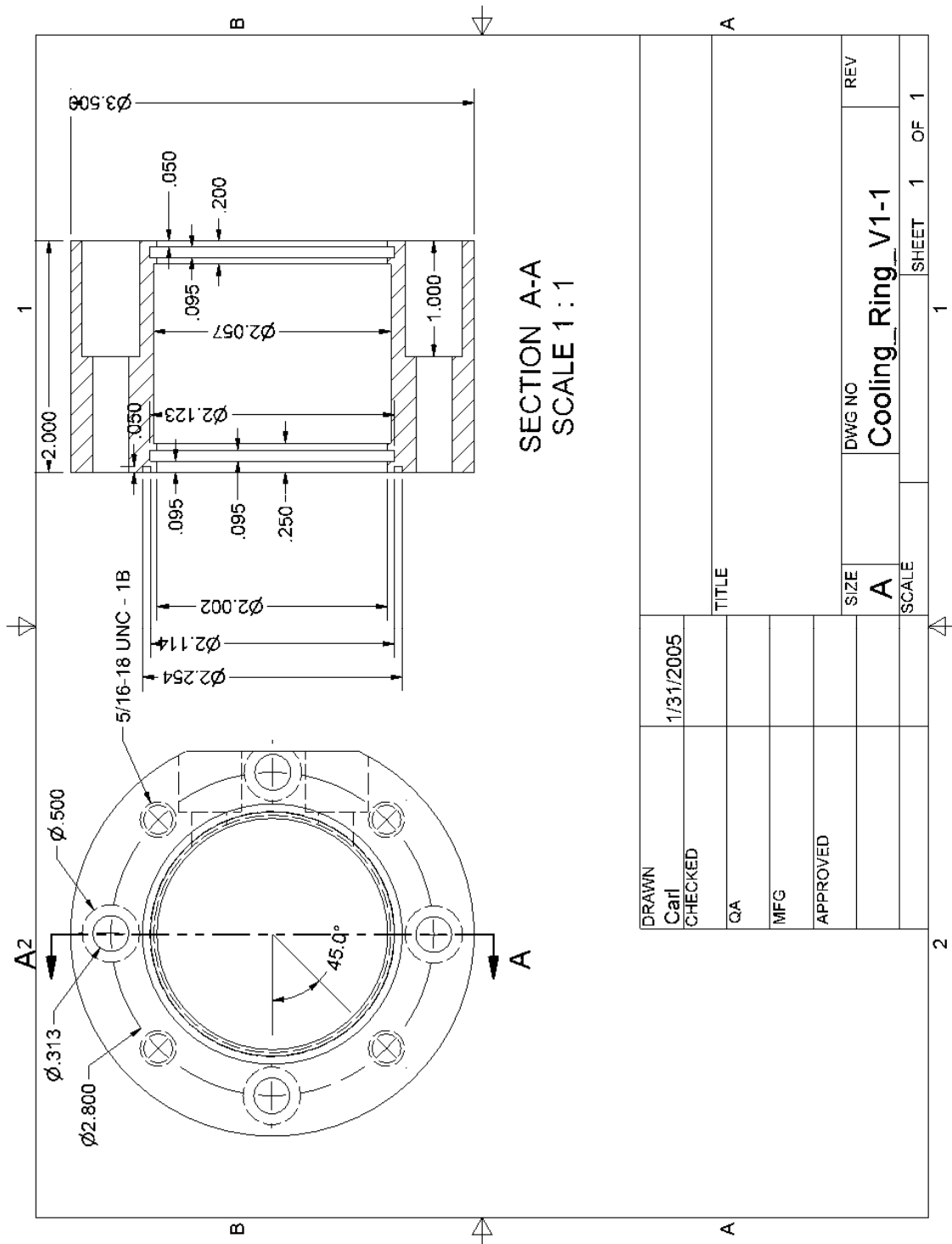
Figure 88.   Rocket Segment/Housing (View 2)

104

SECTION A-A
SCALE 1 : 1

.024

.525

.500

1.000

A

A

DRAWN Carl 1/31/2005
CHECKED
QA
MFG
APPROVED

TITLE

DWG NO Cooling_Ring_V1-2

SIZE A

SCALE

REV

SHEET 1 OF 1
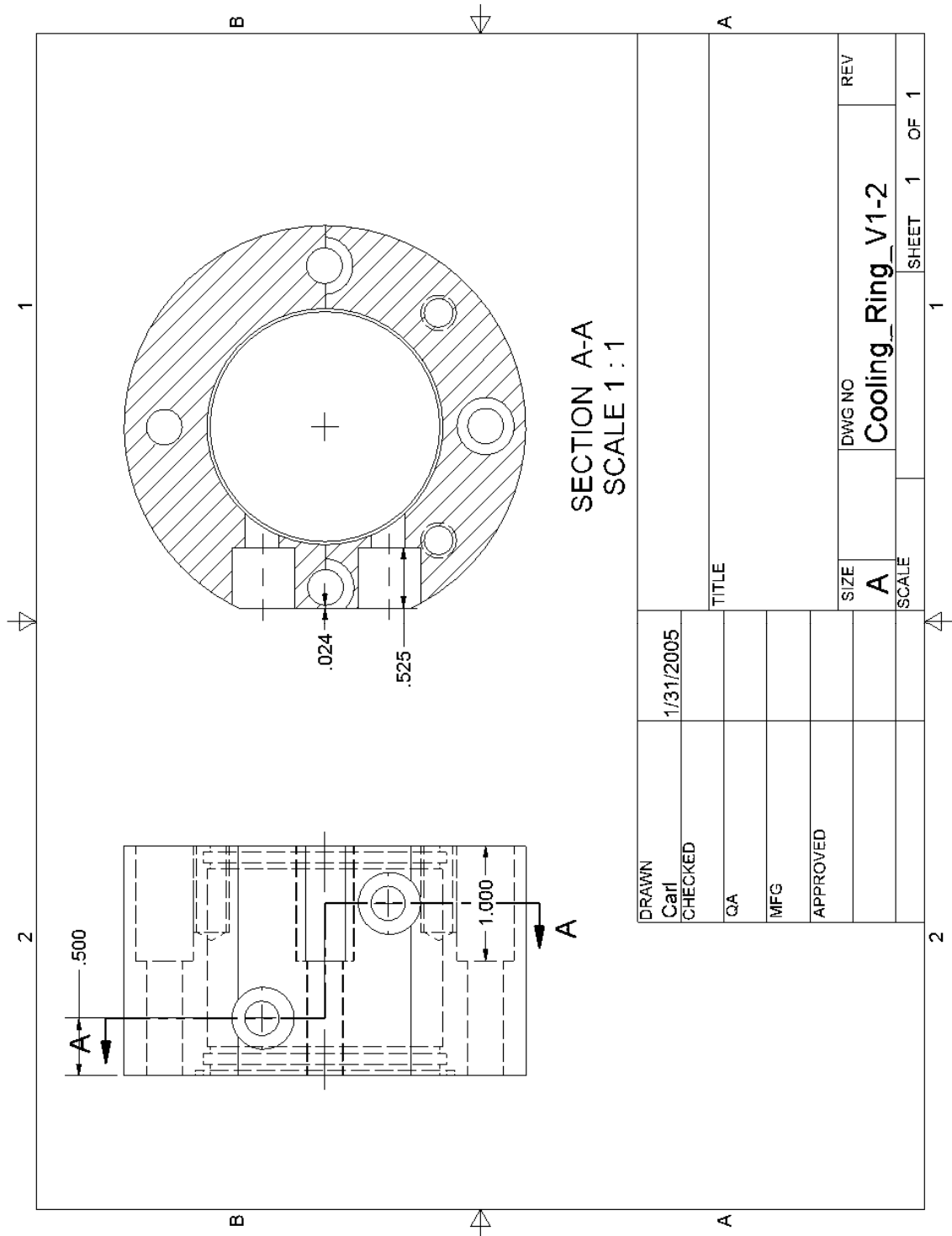
Figure 89.   Rocket Segment/Housing (View 3)

VIEW E-E
SCALE 1:1

SECTION B-B
SCALE 1:1

0.75

1.00

0.75

DRAWN Carl 2/3/2005
CHECKED
QA
MFG
APPROVED

TITLE

DWG NO Cooling_Ring_V1-3

SIZE A

SCALE

REV

SHEET 1 OF 1

Figure 90.   Rocket Segment/Housing (View 4)

106

Figure 91.   Rocket Segment/ Copper Liner

The technical drawing includes the following dimensions and title block information:

- .245
- .245
- $\varnothing 1.700$
- $\varnothing 1.500$
- 1.9900
- $\varnothing 2.0000$

Title block:
- DRAWN: Carl
- CHECKED
- QA
- MFG
- APPROVED
- 1/31/2005
- TITLE
- DWG NO: Cooling_Insert_v1
- SIZE: A
- SCALE
- REV
- SHEET 1 OF 1

SECTION A-A
SCALE 1 : 1

1.780

2.000

.170

DRAWN Carl 10/31/2005
CHECKED
QA
MFG
APPROVED

TITLE

SIZE A

DWG NO Cooling_Ring_V2

REV

SCALE

SHEET 1 OF 1

Figure 92.   Chamber Section 3

SECTION A-A
SCALE 1 : 1

Ø3.500
.25
Ø2.379
Ø2.239
Ø.500
.05
.990
Ø.700
Ø2.000
.250
R.400
Ø.313

DRAWN Carl
CHECKED
QA
MFG
APPROVED

10/31/2005

TITLE

SIZE A
SCALE

DWG NO Cooling_insert&Film_Ring_Shiel

REV

SHEET 1 OF 1

Figure 93.   Chamber Section 3 Liner & Film Cooling Interface

Figure 94.   Copper Nozzle Segment
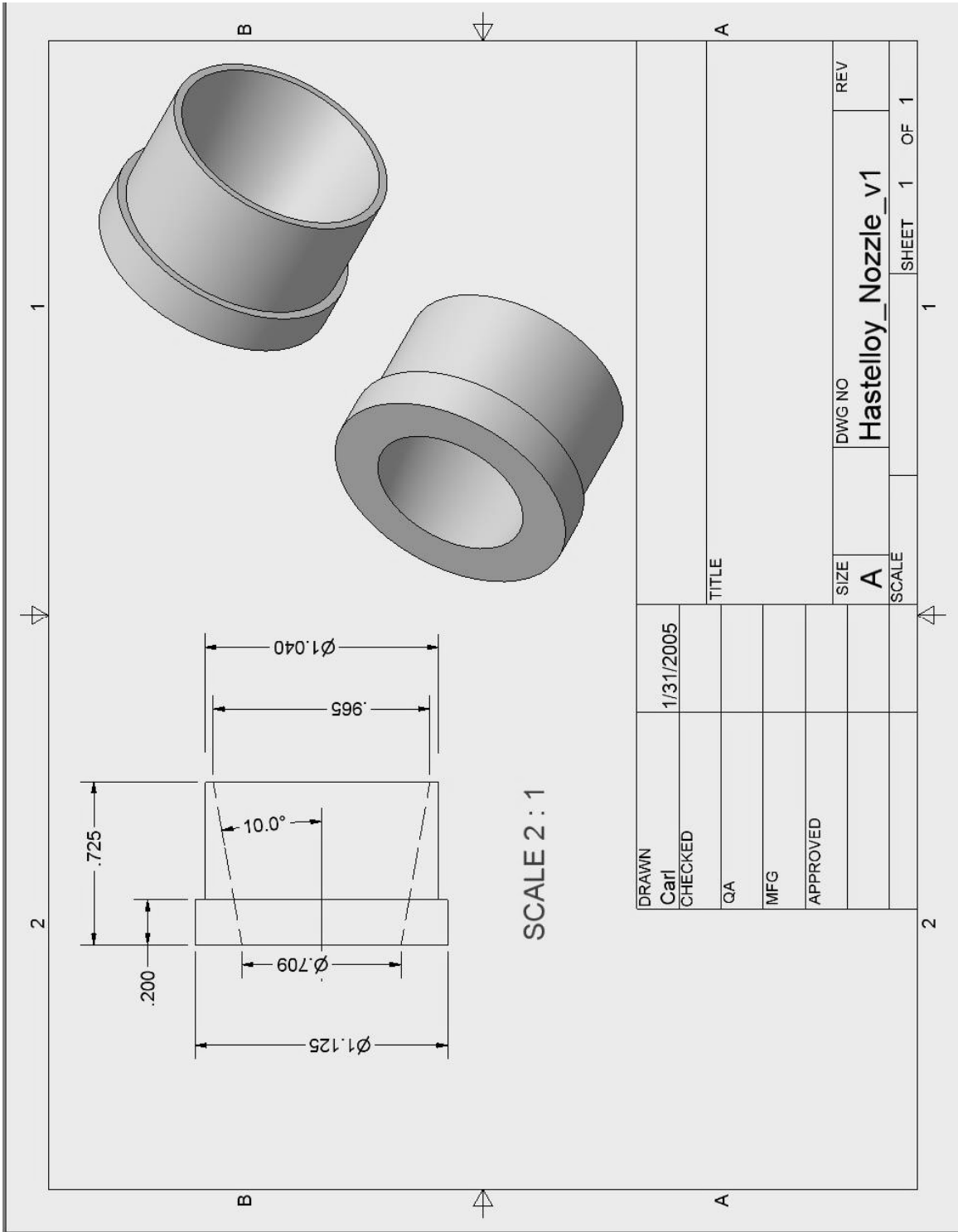
Figure 95.   Hastelloy Nozzle Segment

111
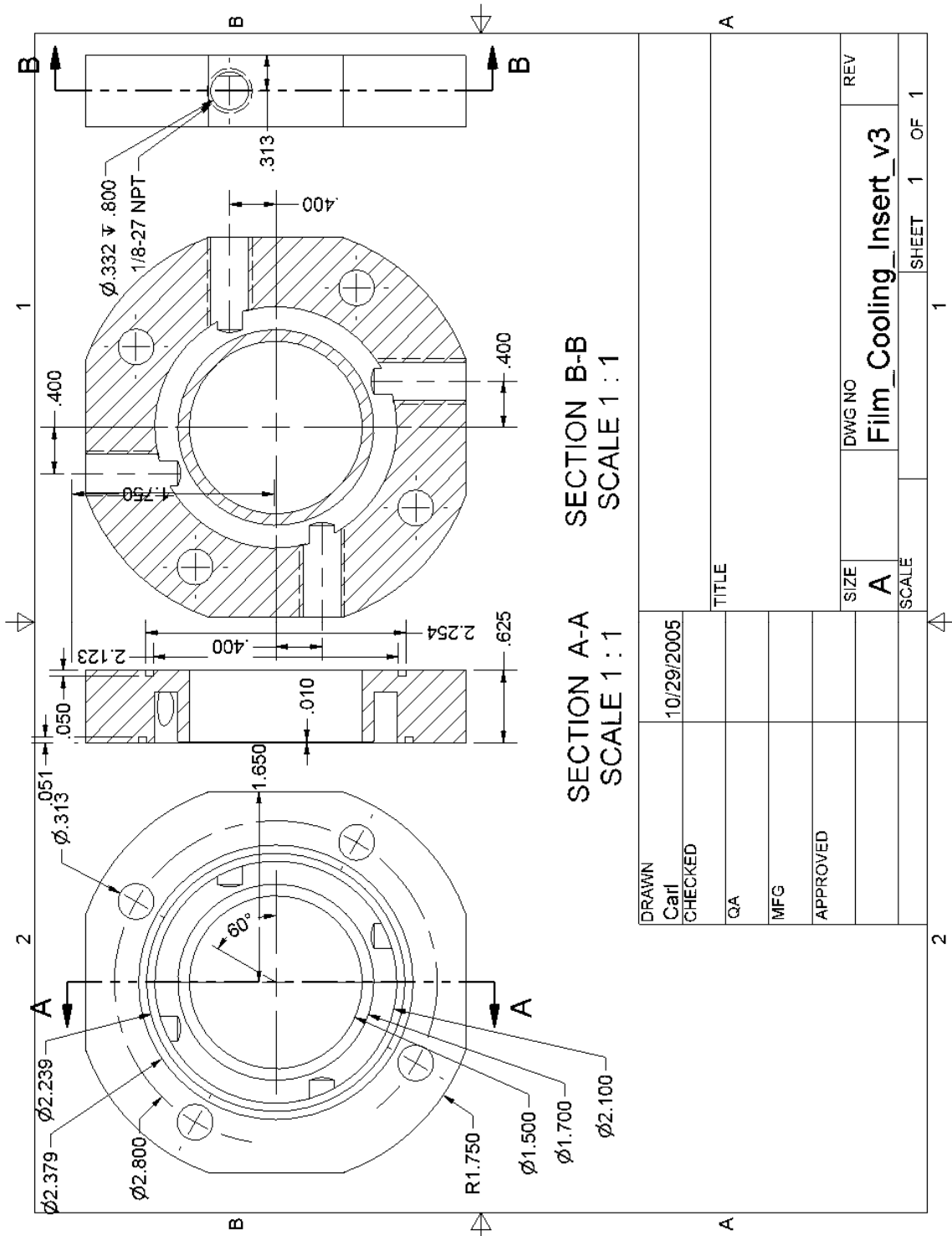
Figure 96.   Copper Film Cooling Ring Segment (View 1)
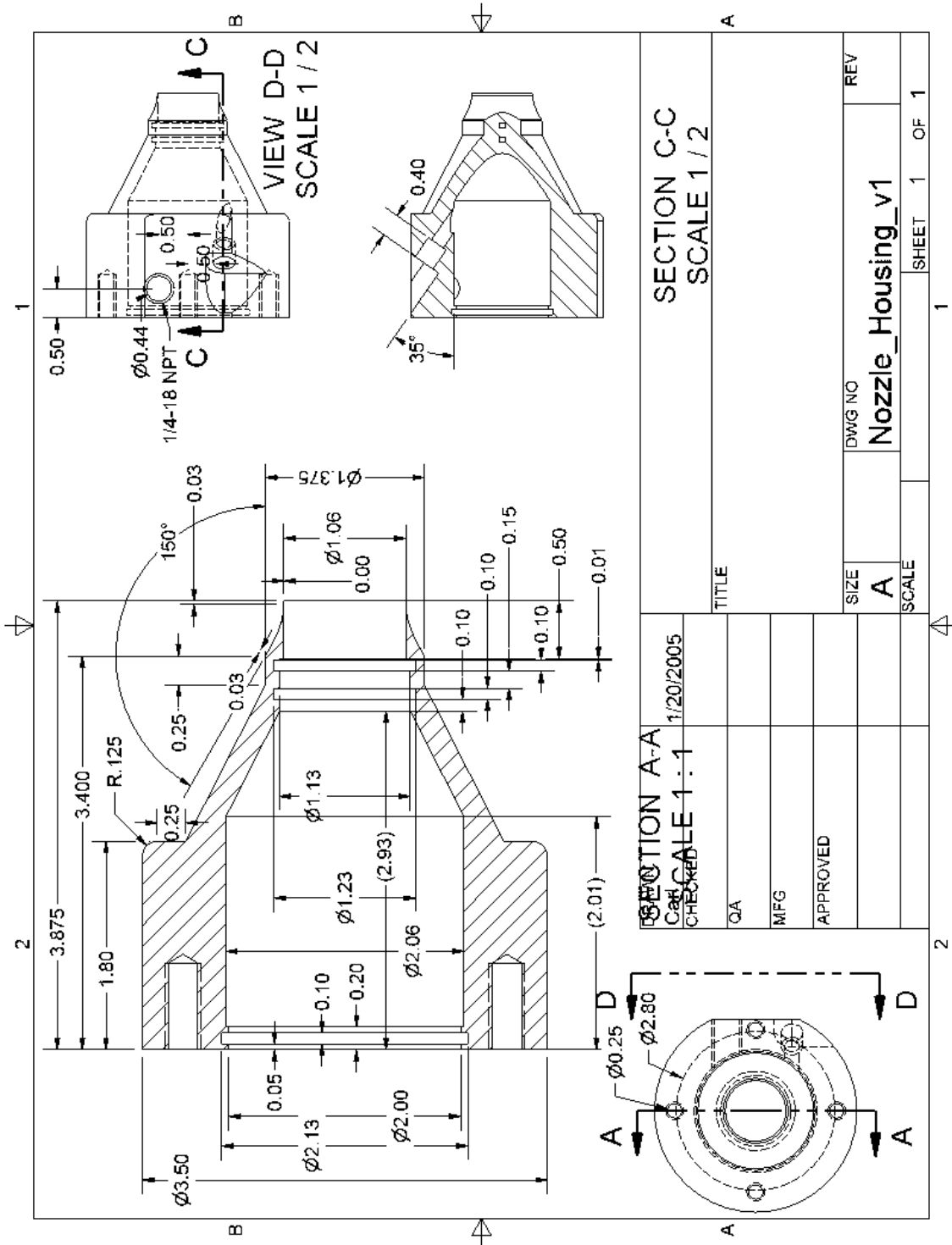
Figure 97.   Nozzle Housing (View 1)
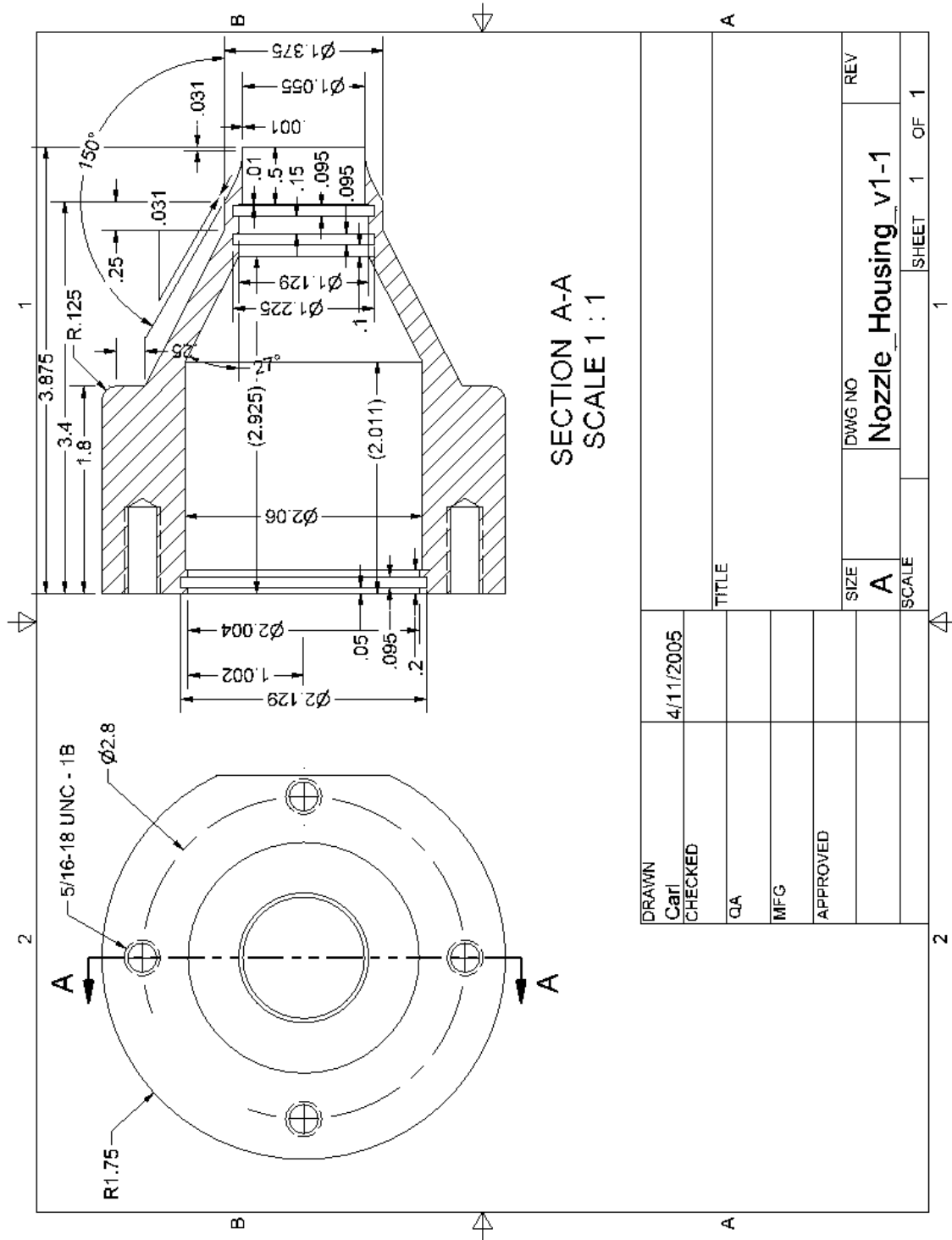
Figure 98.   Nozzle Housing (View 2)

SECTION A-A
SCALE 1 : 1

1.580

.612

55.0°

.377

.250

.400

35.0°

1.096

1.106

.767

.844

1/4-18 NPT

.500

.501

.626

.313

A

A

B

B

A

A

1

2

1

2

DRAWN
Carl
CHECKED

QA

MFG

APPROVED

4/11/2005

TITLE

SIZE
A

SCALE

DWG NO
Nozzle_Housing_v1-2

REV

SHEET   1   OF   1
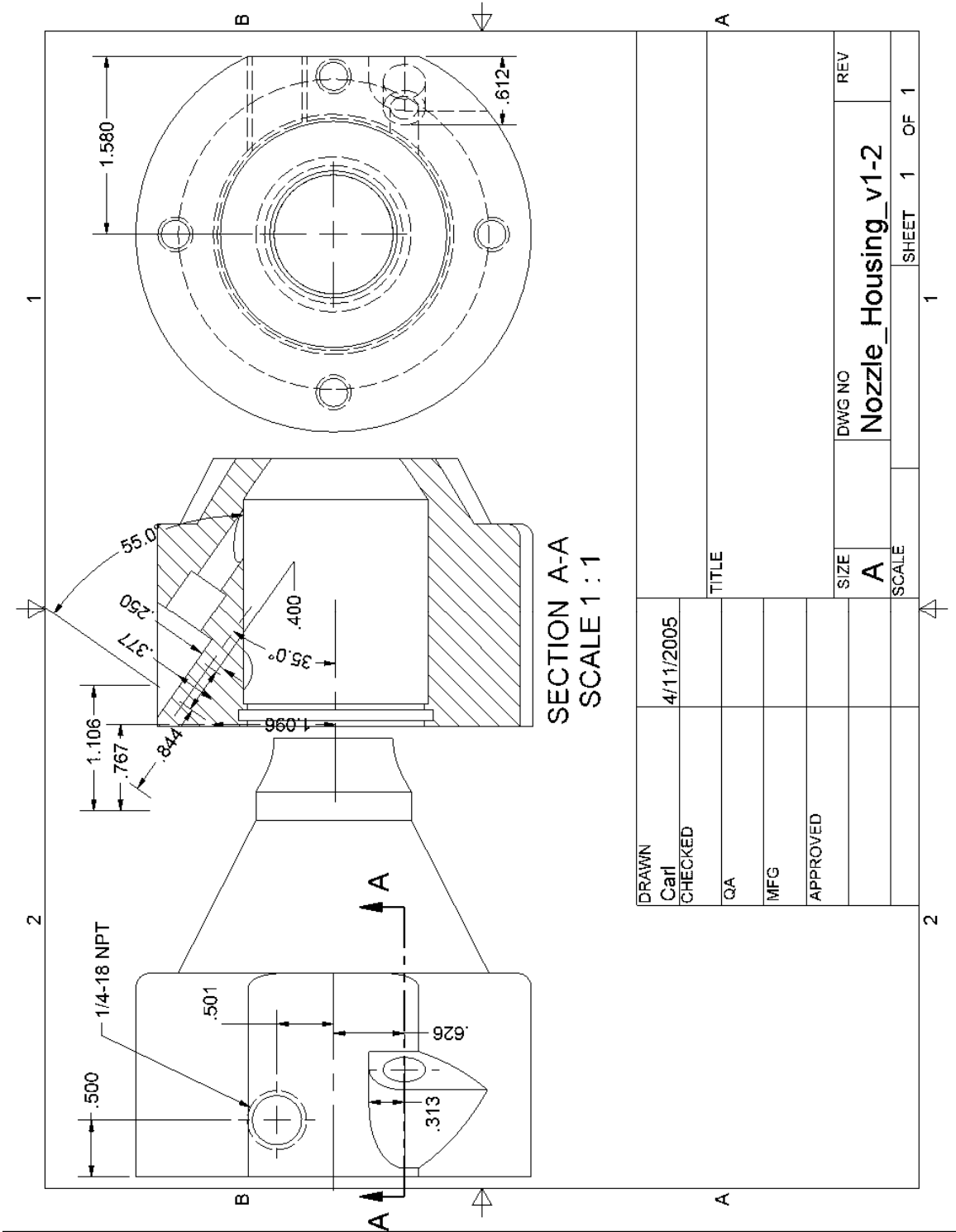
Figure 99.   Nozzle Housing (View 3)

115

SECTION A-A
SCALE 1 : 1

.568
.677
.906
.356
.313
35.0°

.313

DRAWN Carl   5/20/2005
CHECKED
QA
MFG
APPROVED

TITLE

DWG NO   Nozzle_Housing_v1-3

SIZE
A

SCALE

REV

SHEET 1 OF 1
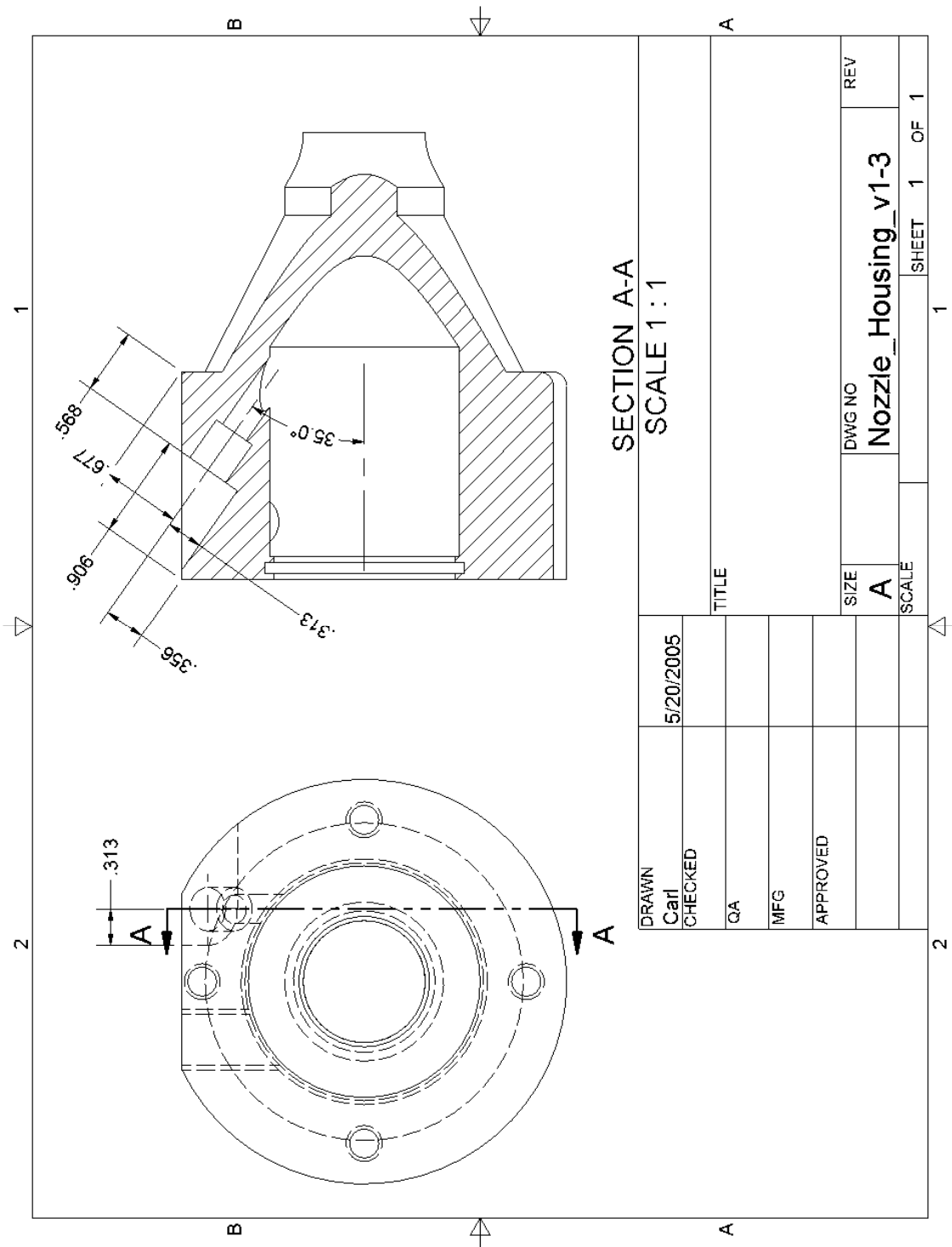
Figure 100.   Nozzle Housing (View 4)

116

B. ENGINE STAND HARDWARE
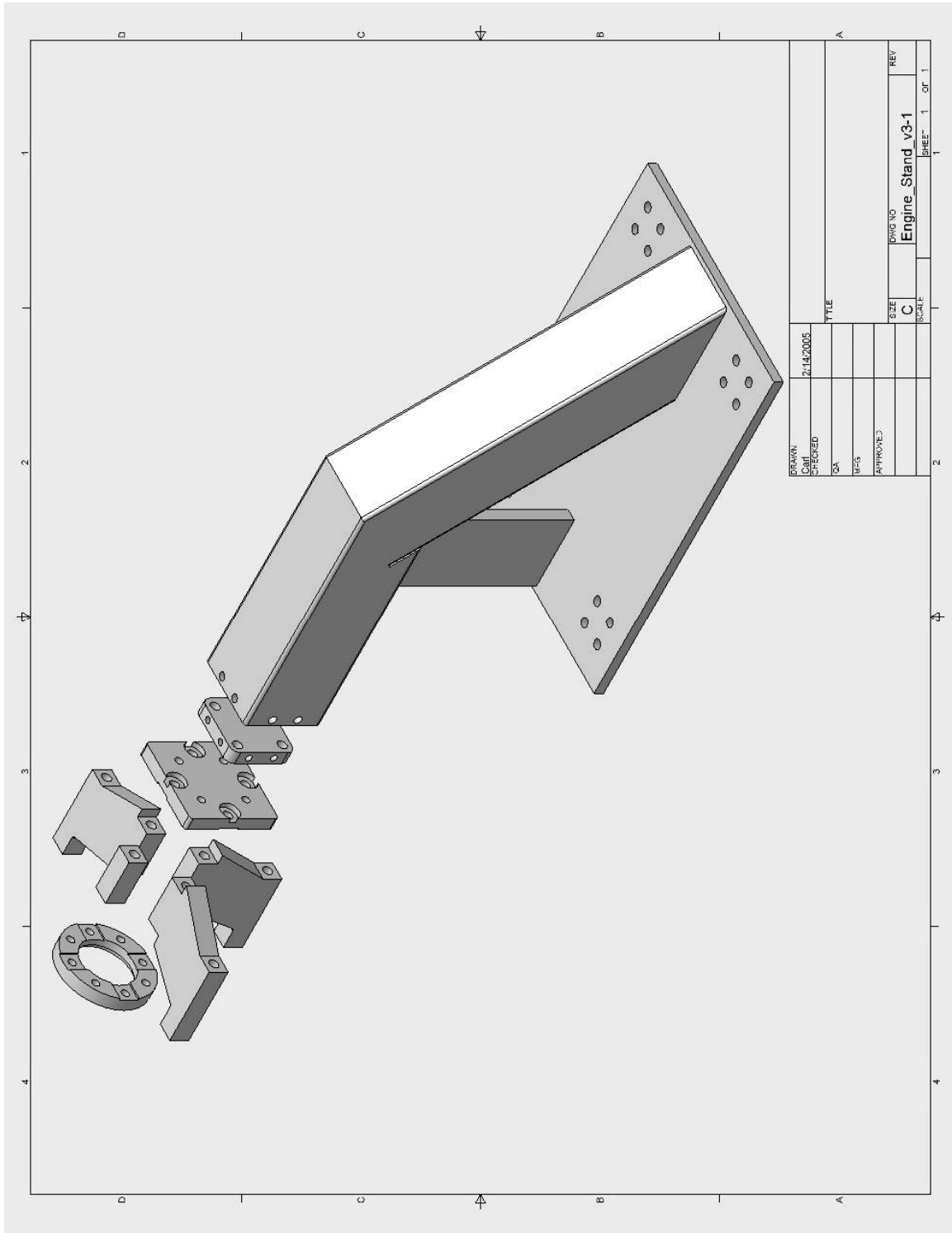
Figure 101. Engine Stand, Exploded View
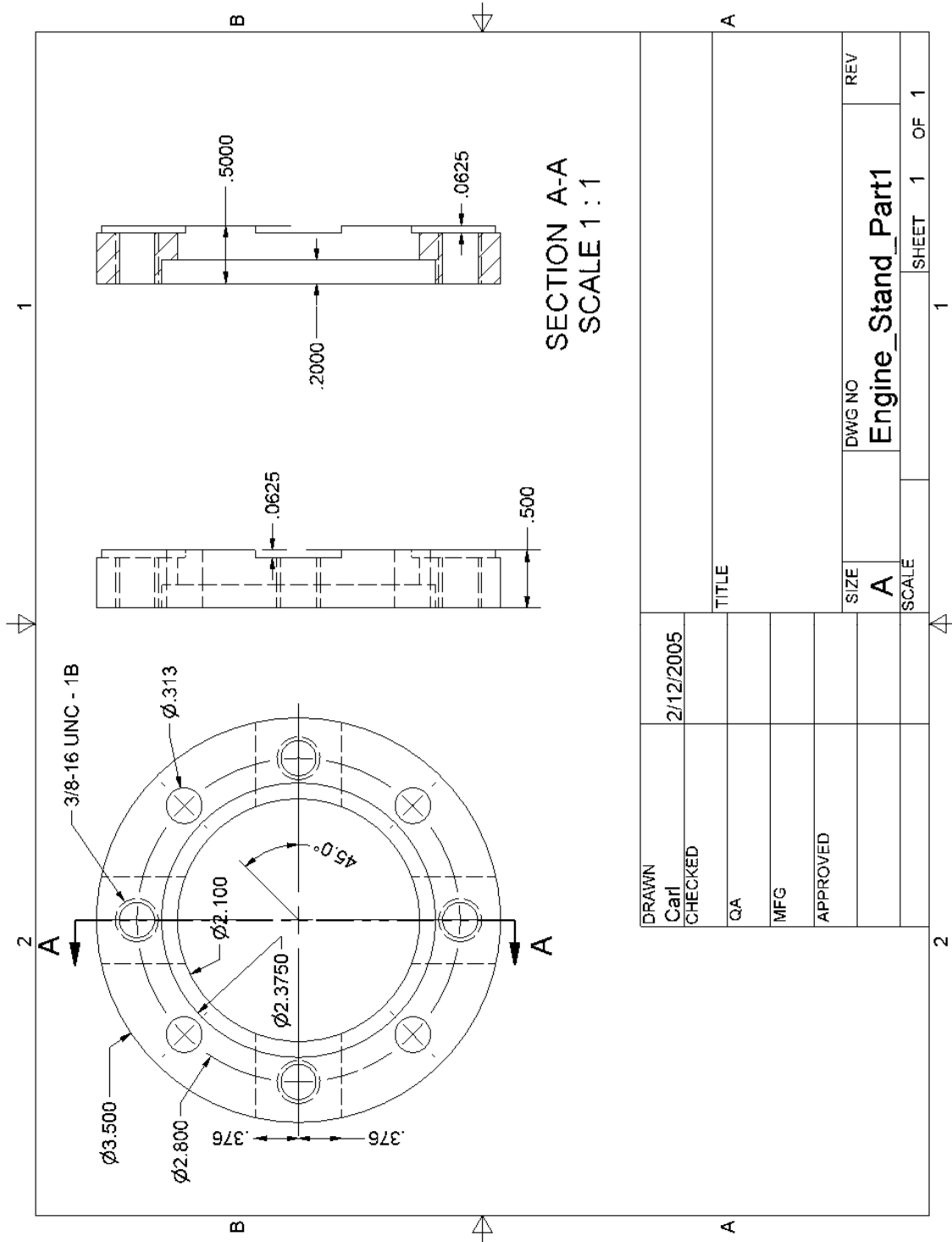
Figure 102. Engine Mounting Ring
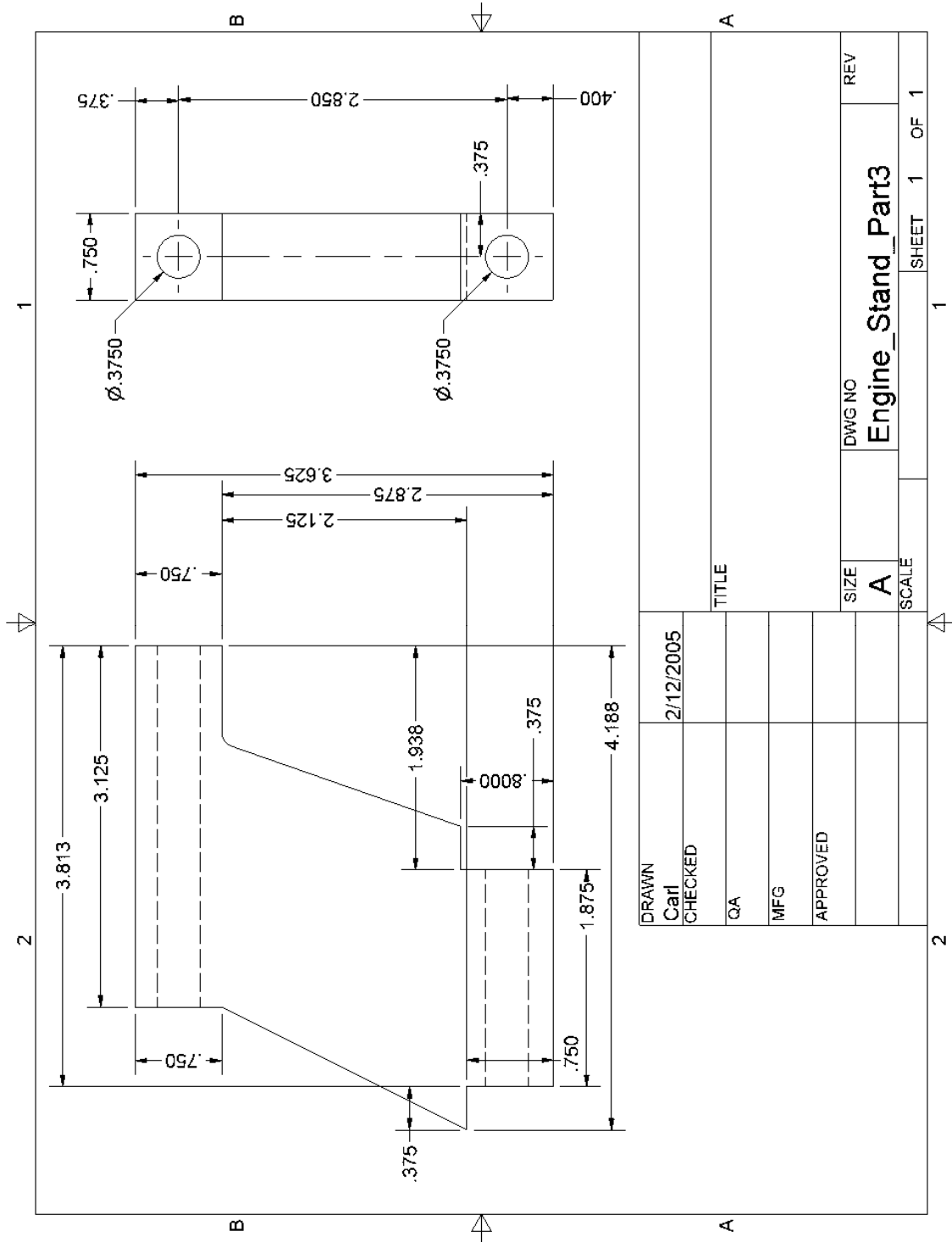
Figure 103.   Engine Mount Stand-Offs and Flow Director Supports (x3)
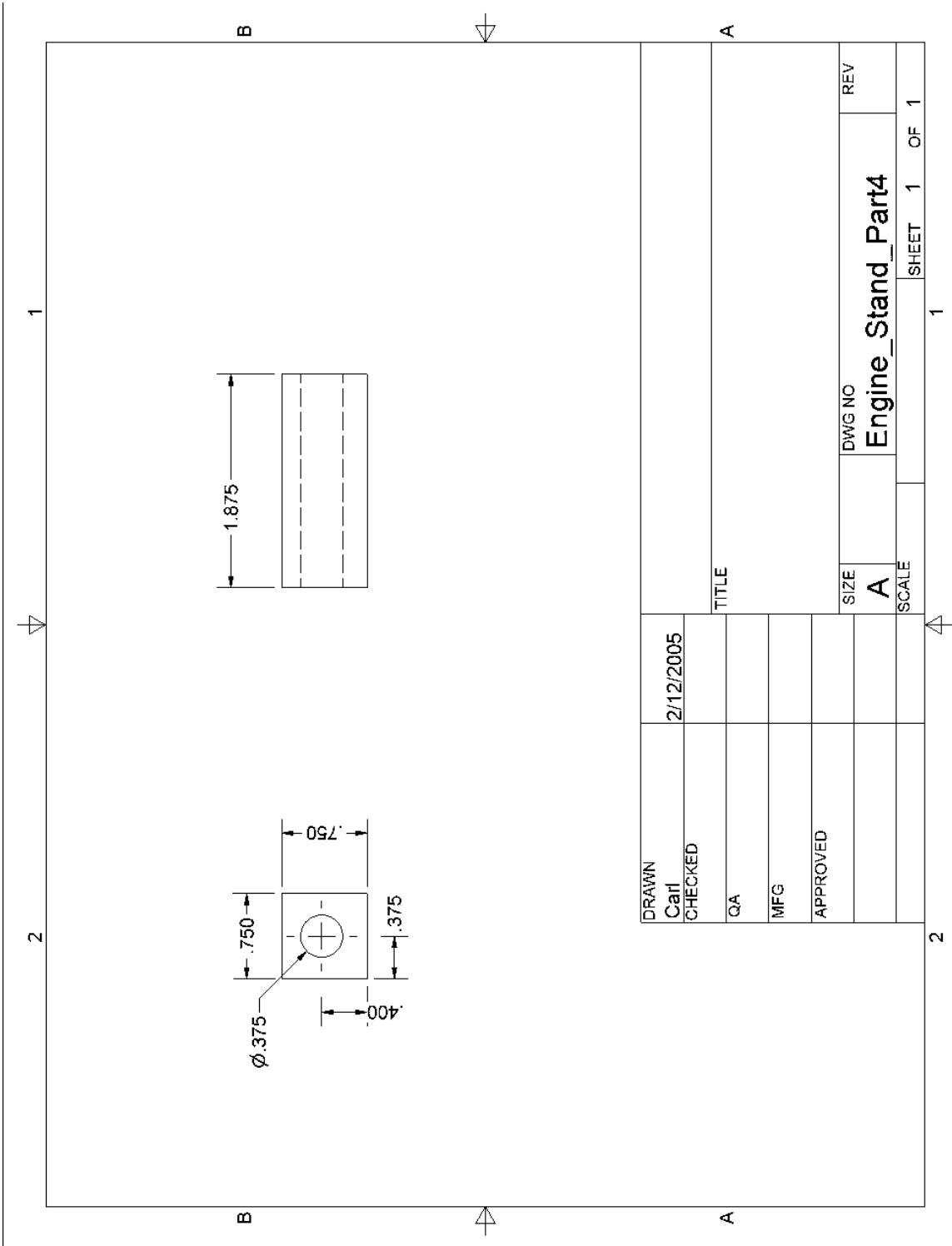
Figure 104.　Engine Mount Stand-Off (x1)
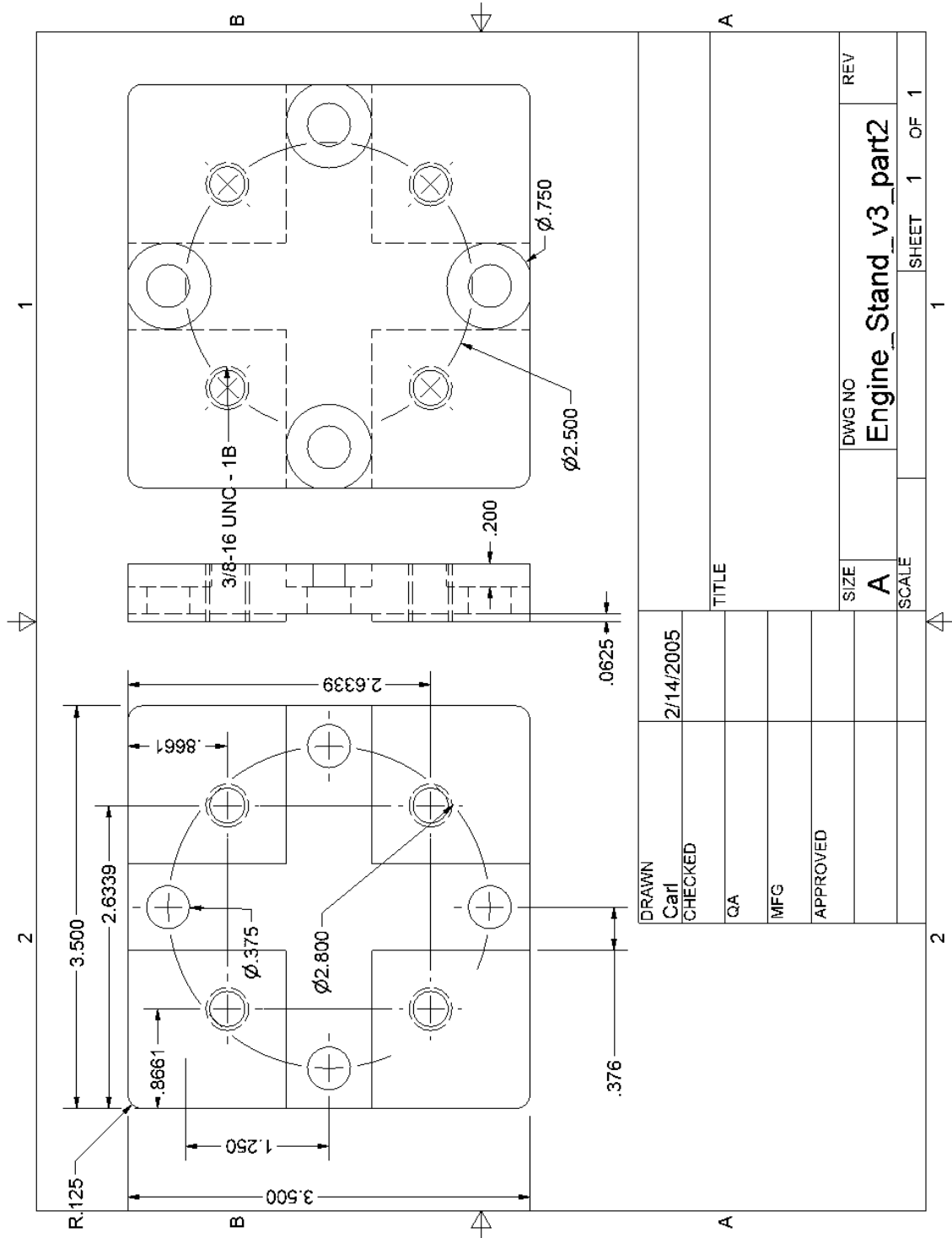
Figure 105.   Engine Stand-Off Mounting Plate
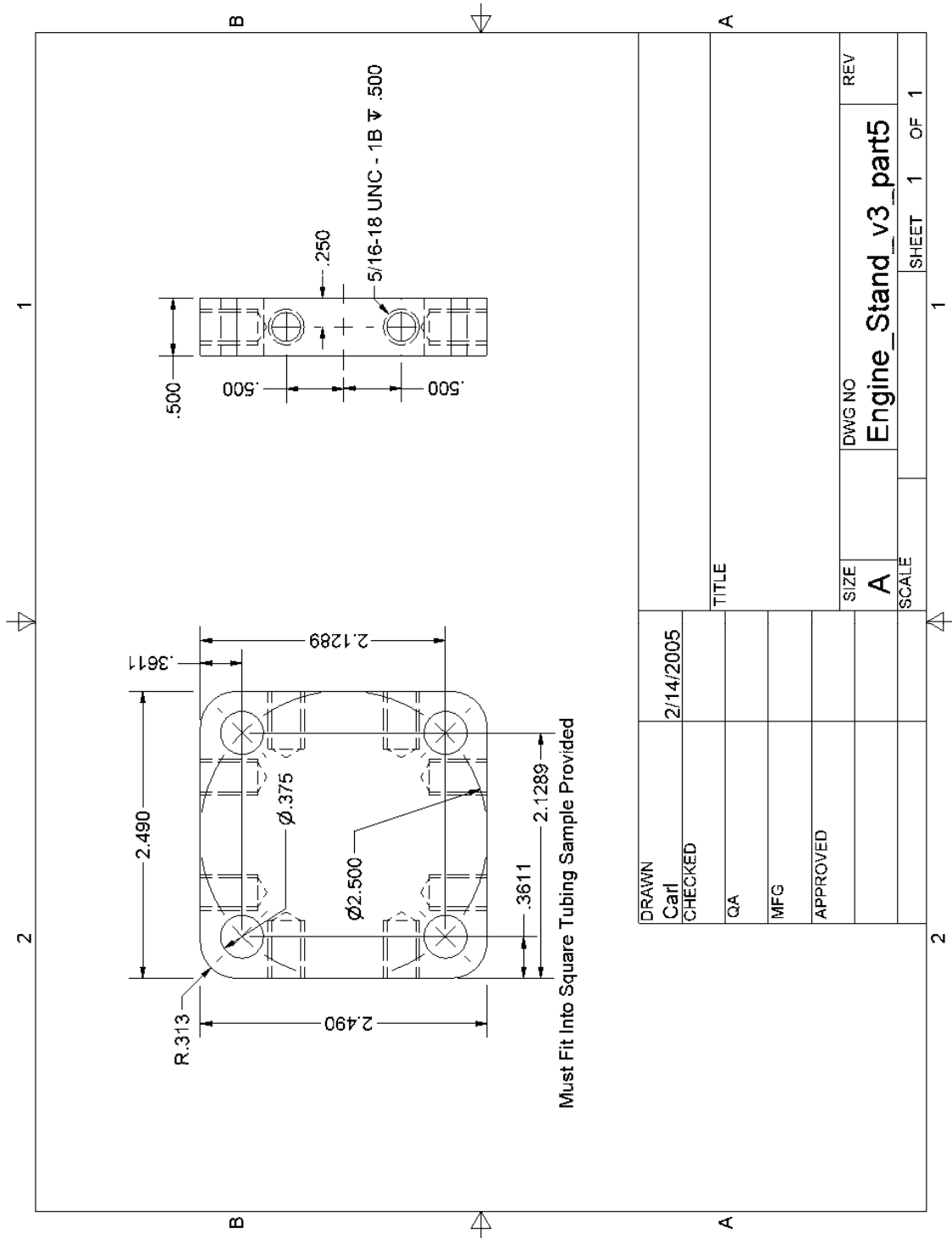
Figure 106. Engine Mount to Stand Adaptor Plate

Figure 107.   Engine and Flow Director Stand

C.   AIRFLOW DIRECTOR HARDWARE
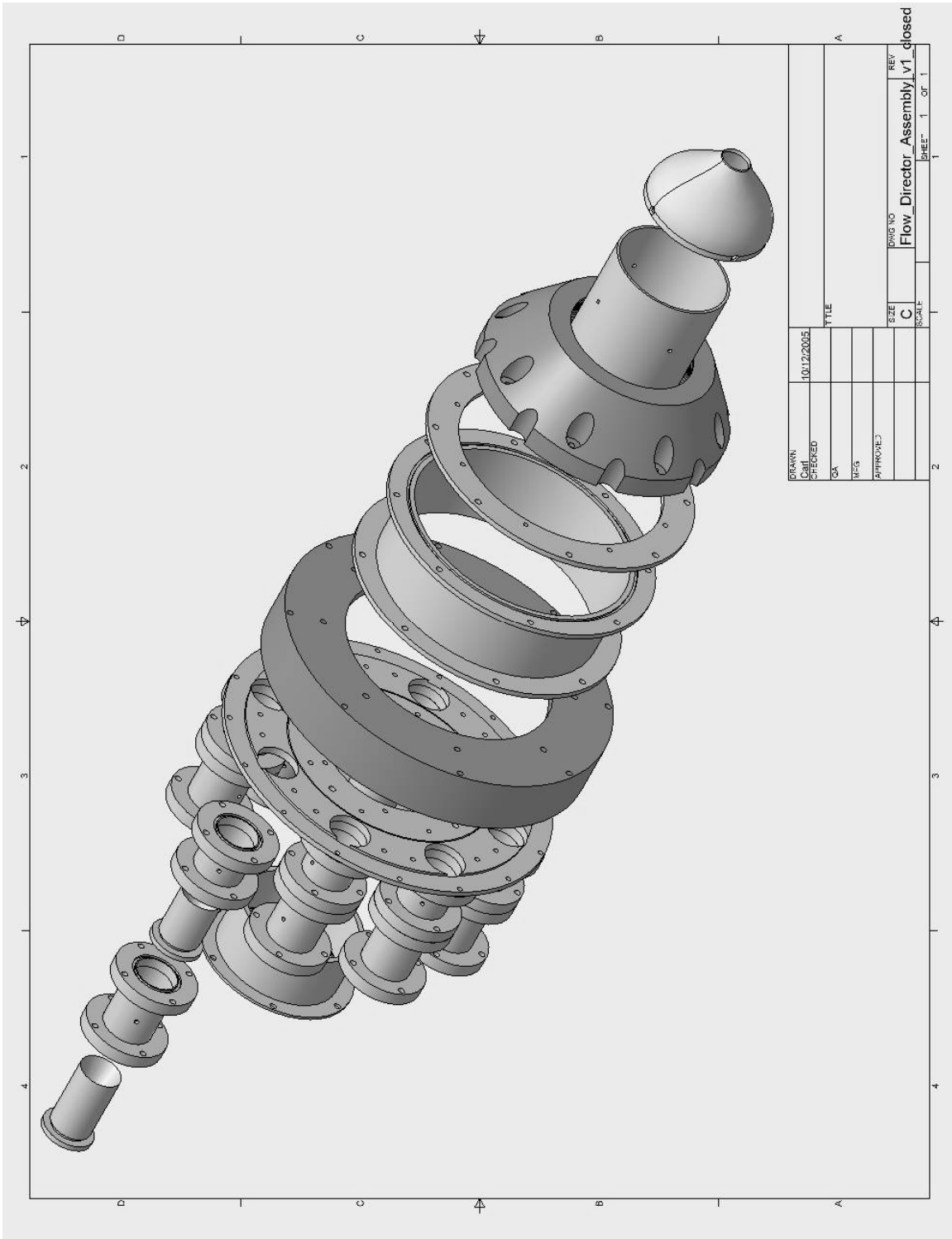
Figure 108.   Airflow Director Exploded View
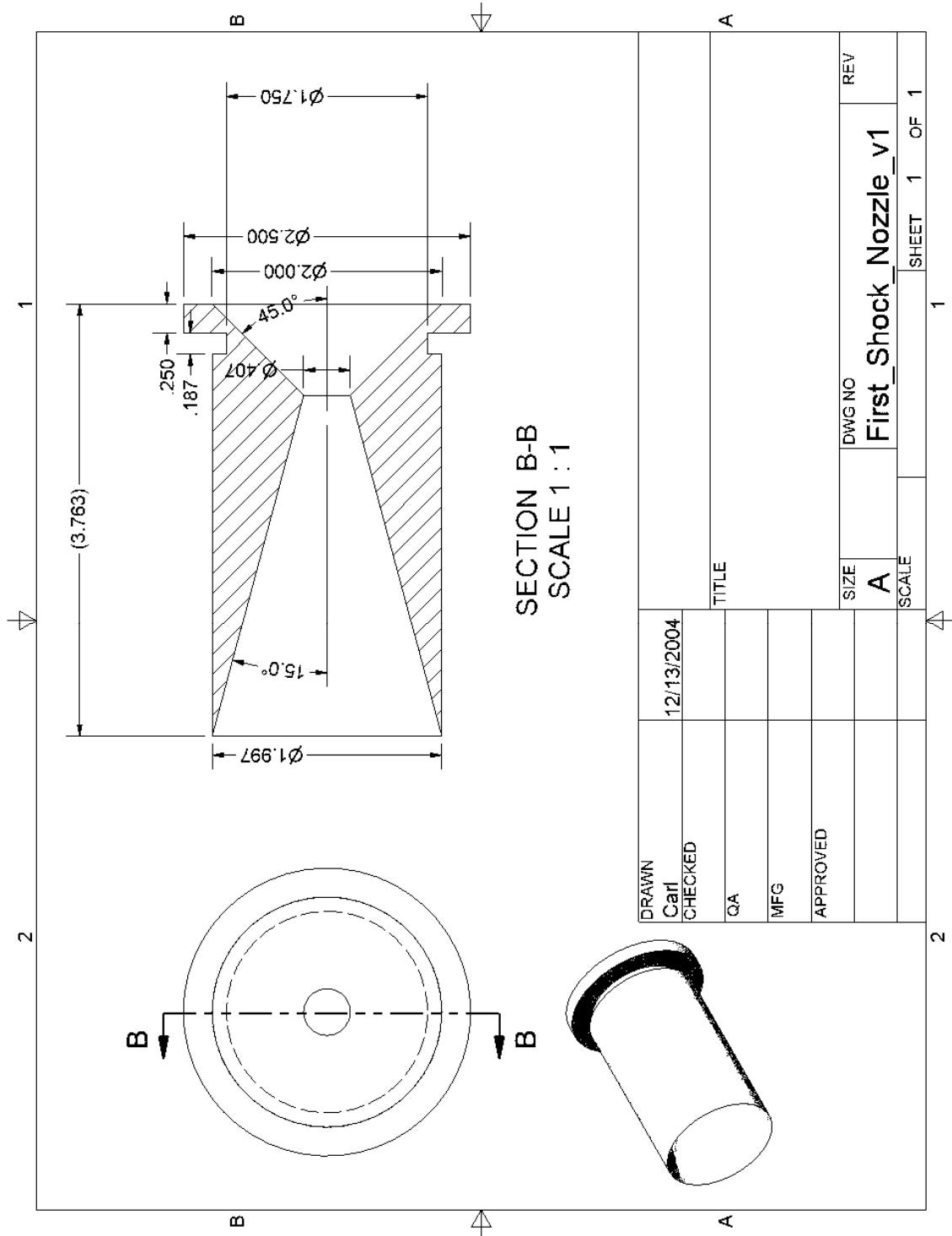
Figure 109.   First Shock Nozzle

125

Figure 110. Second Shock Nozzle
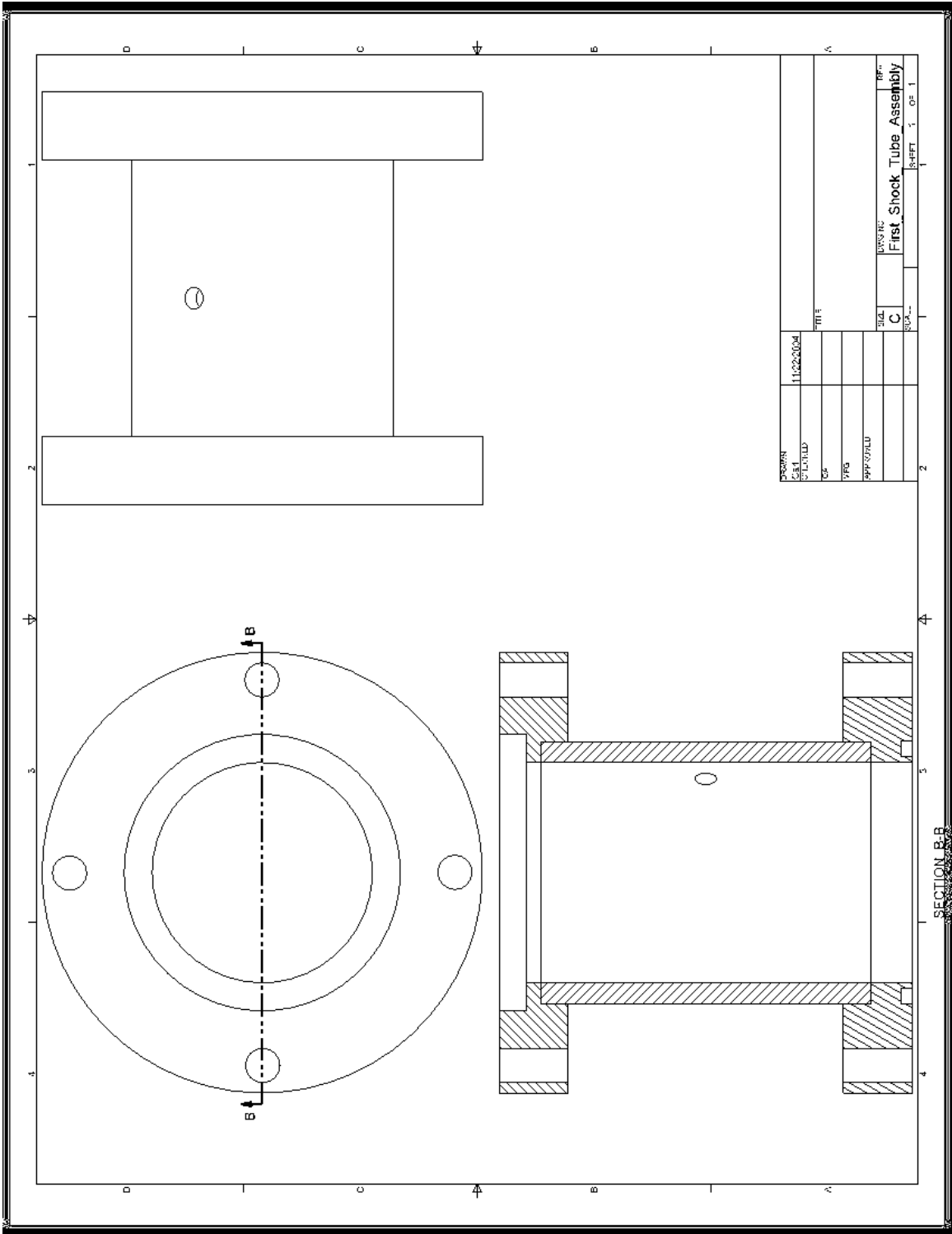
Figure 111.　First Shock Nozzle Housing (Tube, Upstream & Downstream Flanges)
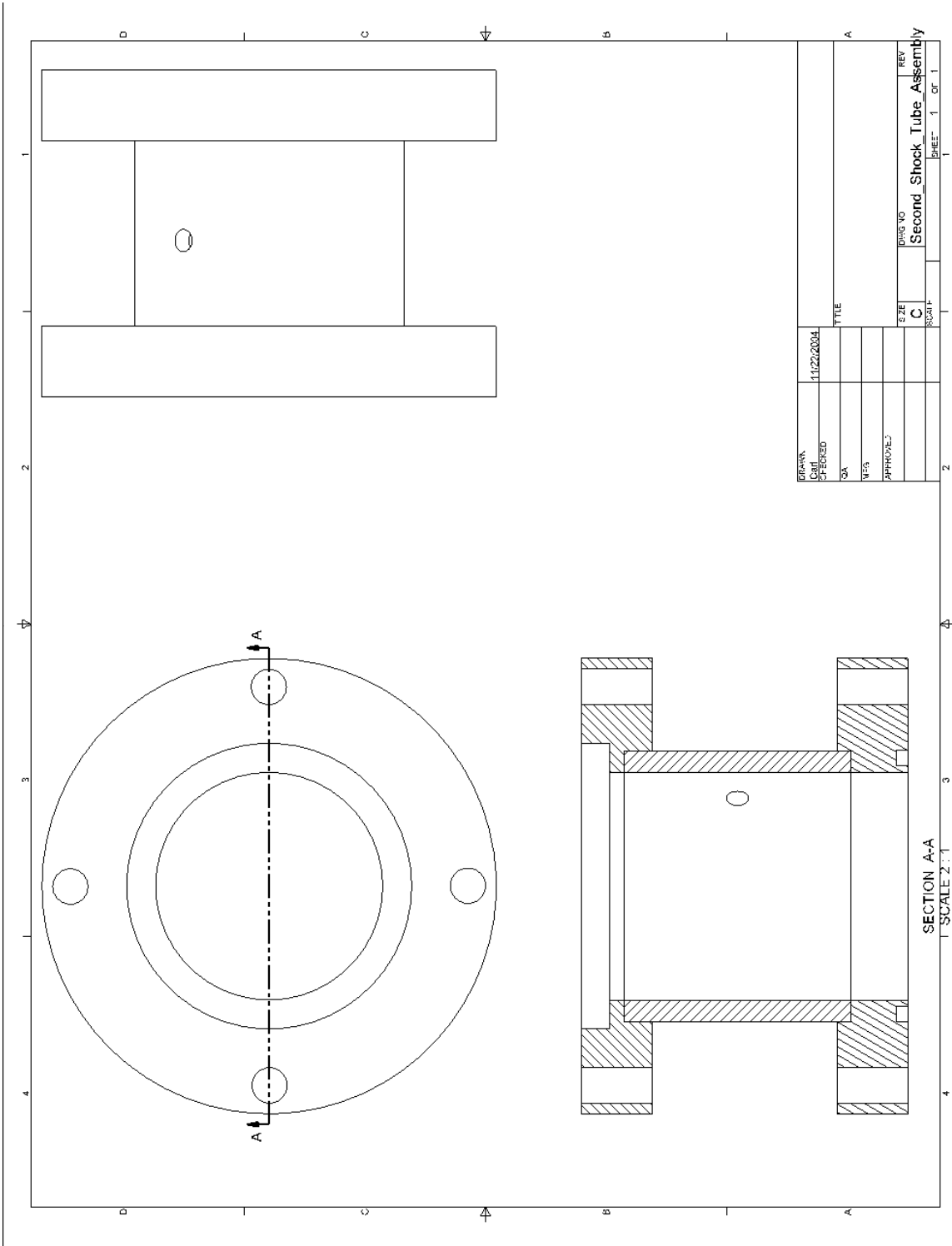
Figure 112.   Second Shock Nozzle Housing (Tube, Upstream & Downstream Flanges)
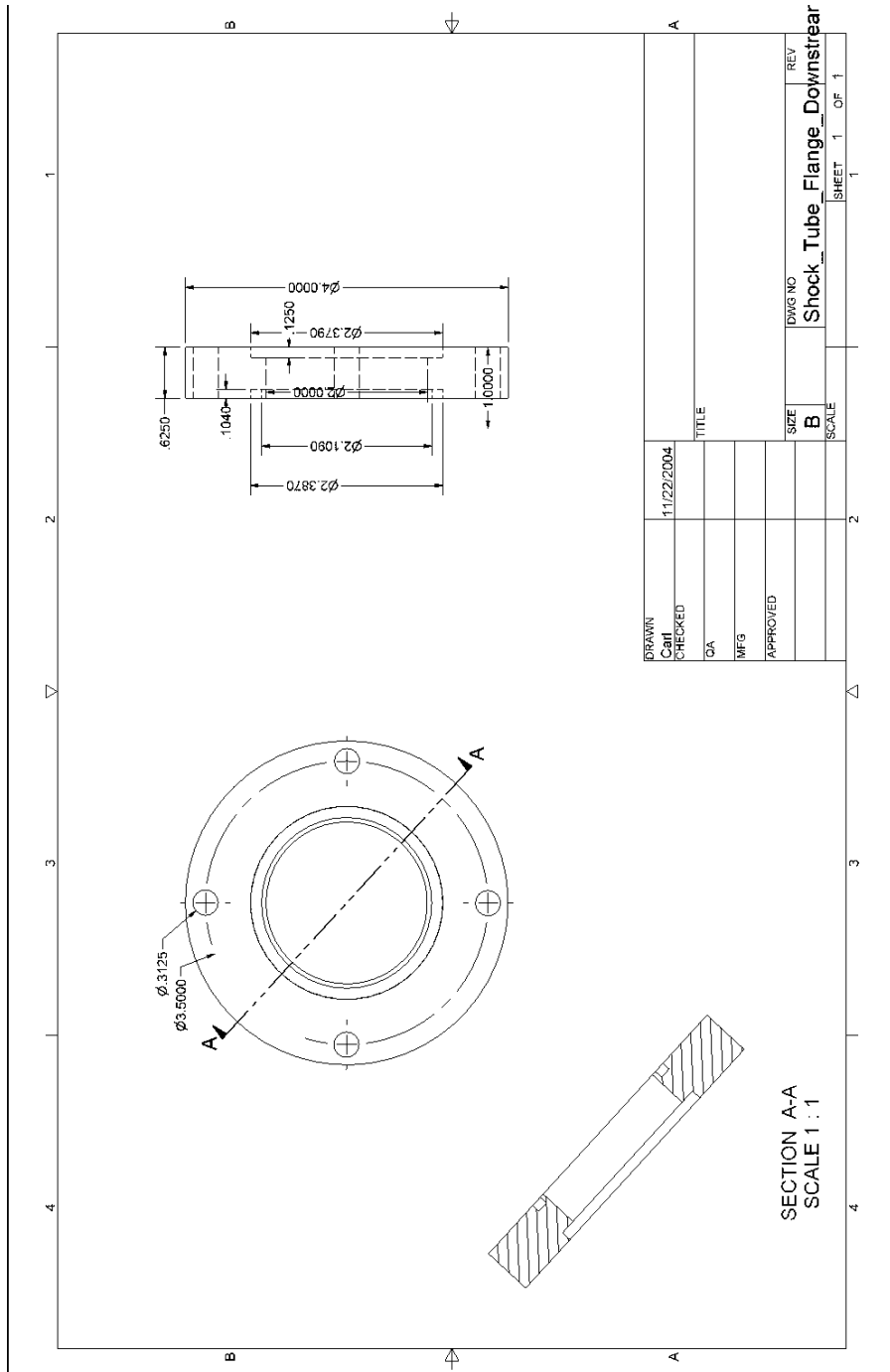
Figure 113.   Shock Nozzle Housing Downstream Flange
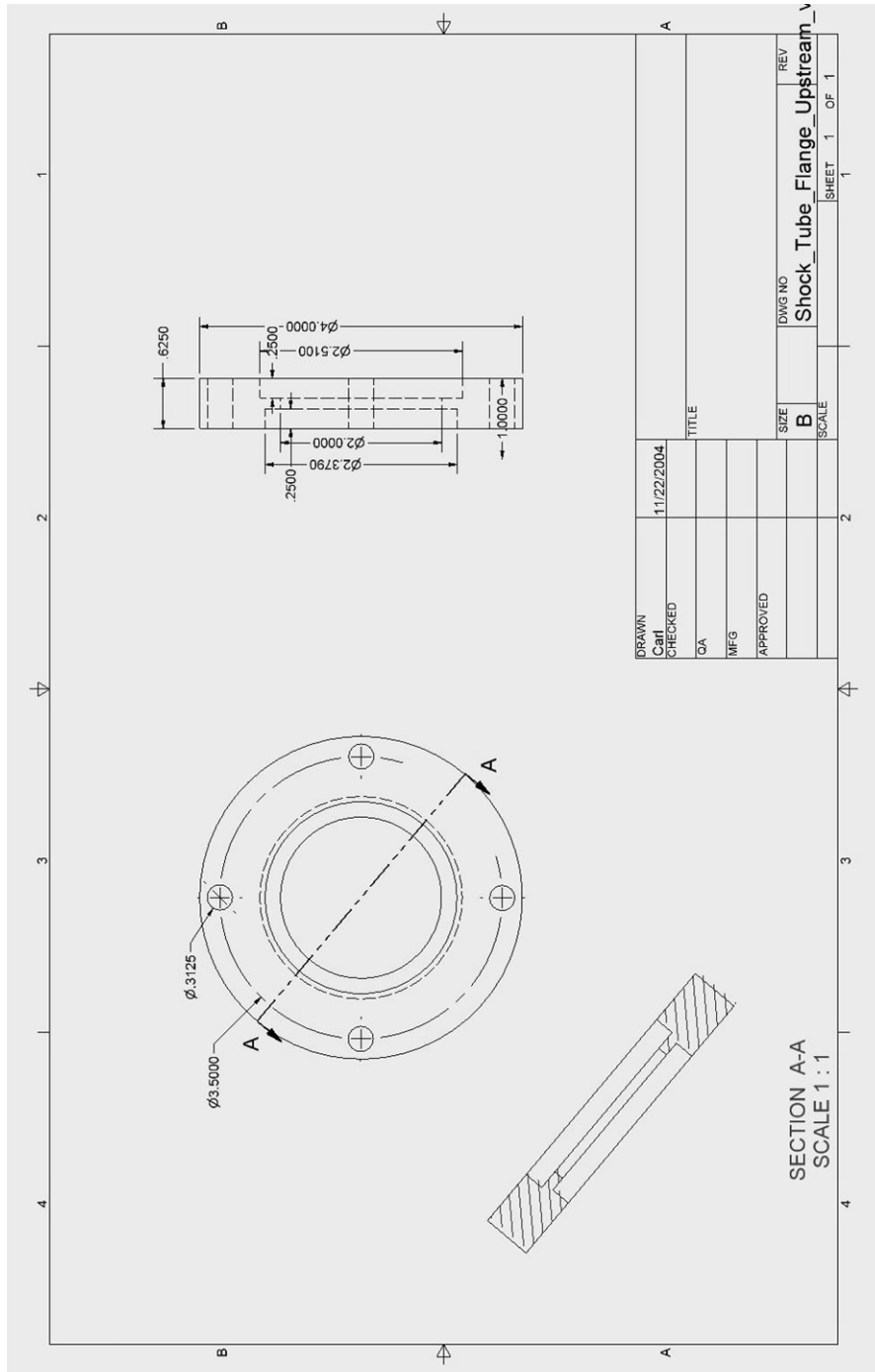
Figure 114.   Shock Nozzle Housing Upstream Flange
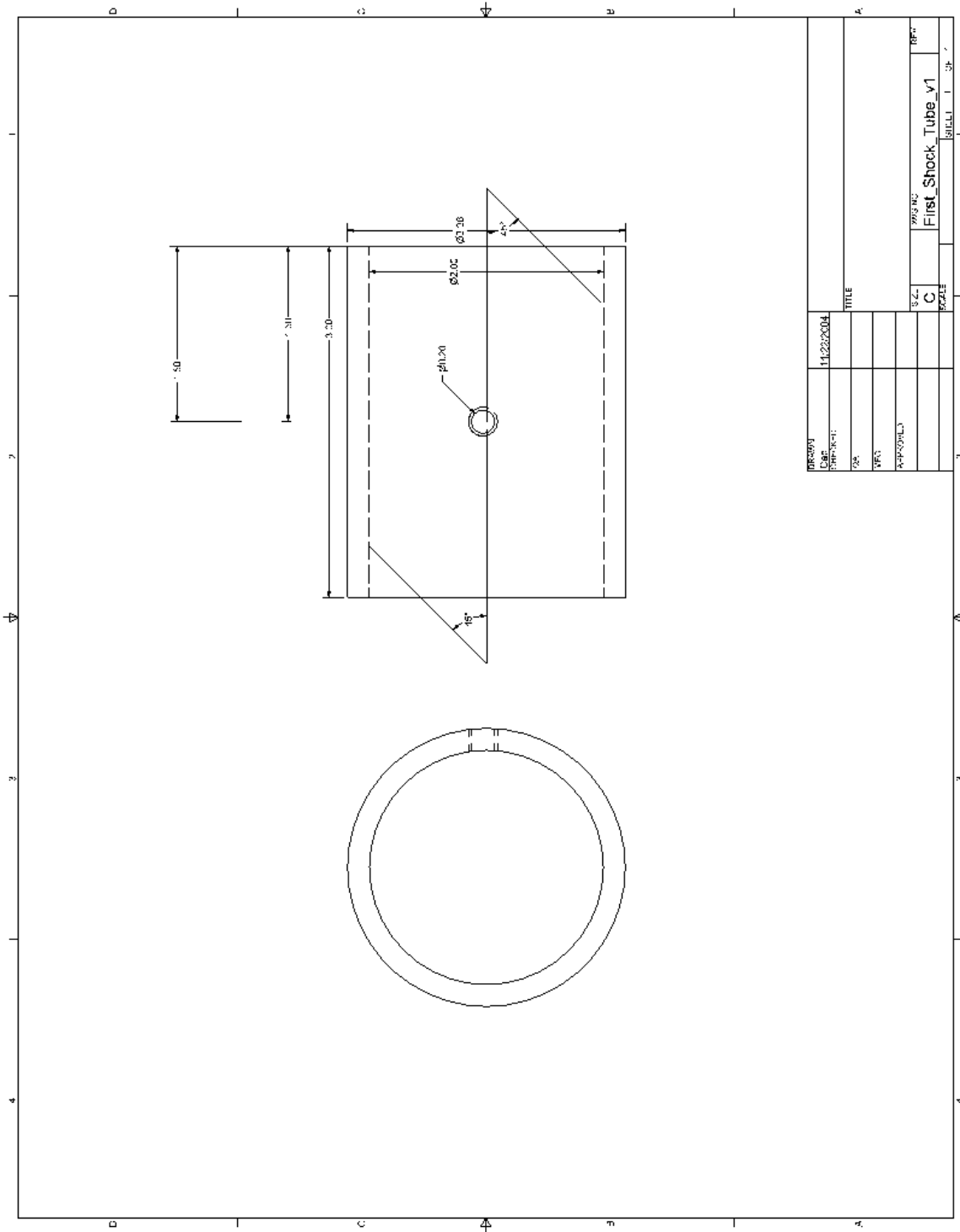
Figure 115.   First Shock Nozzle Housing Tube
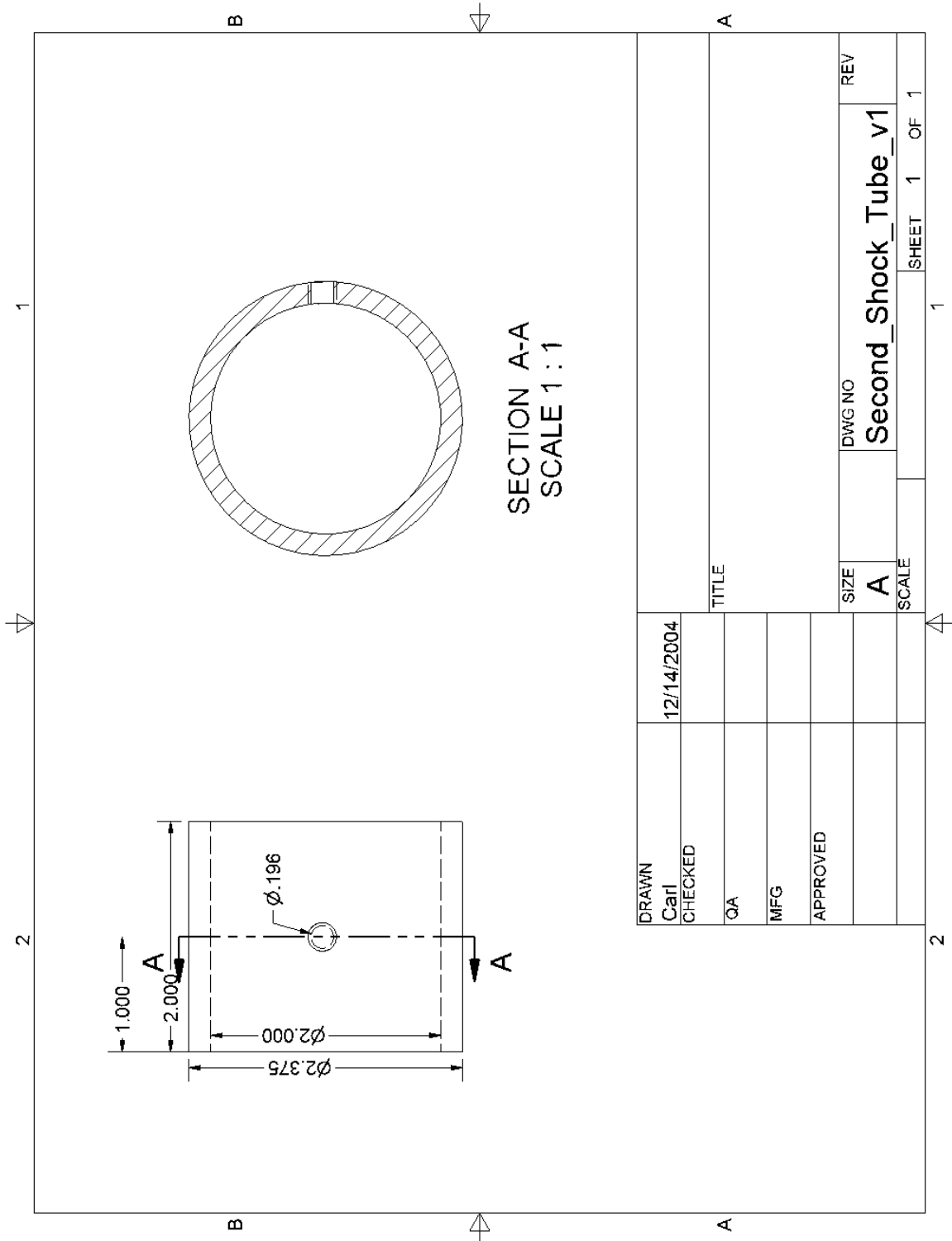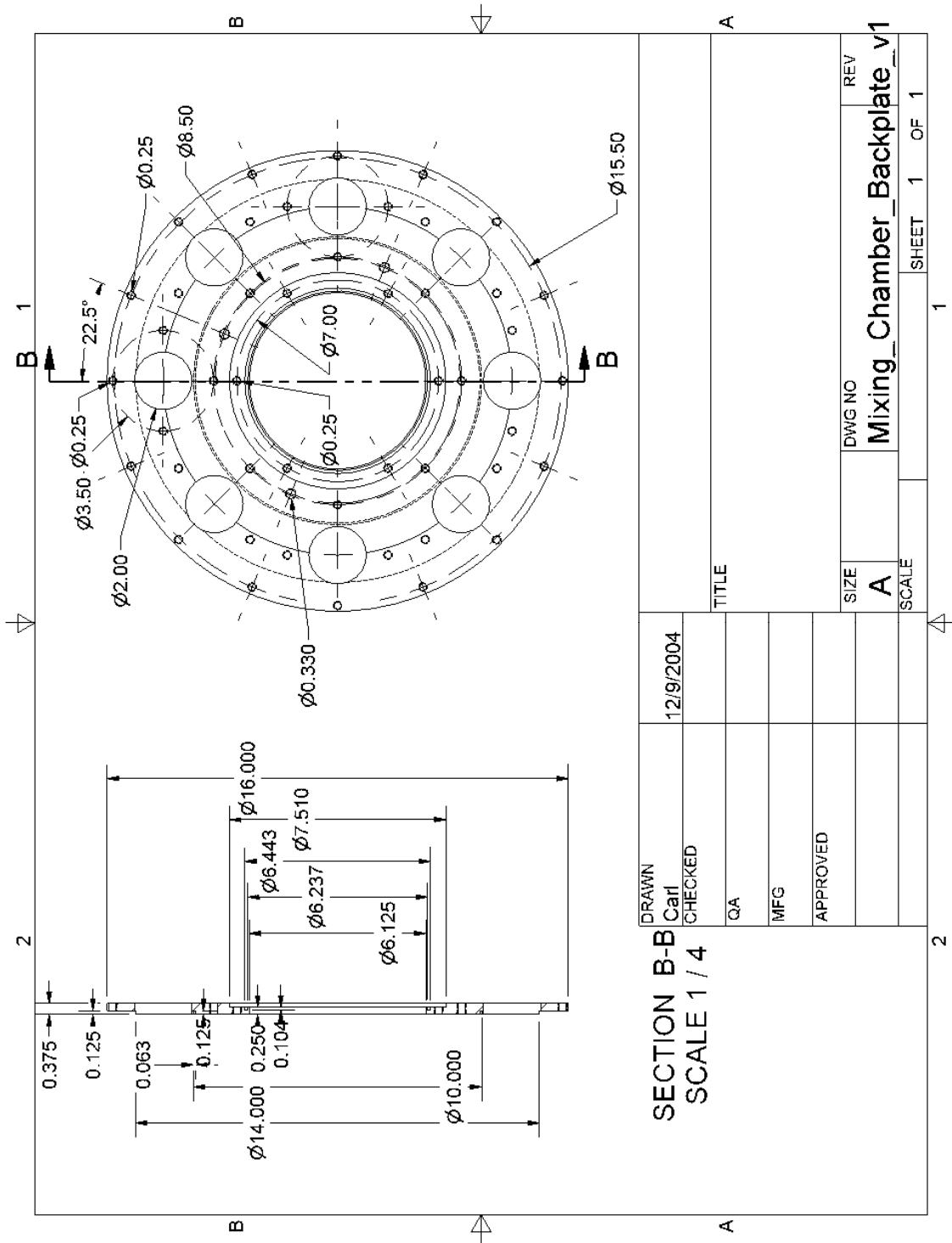
Figure 116.   Second Shock Nozzle Housing Tube
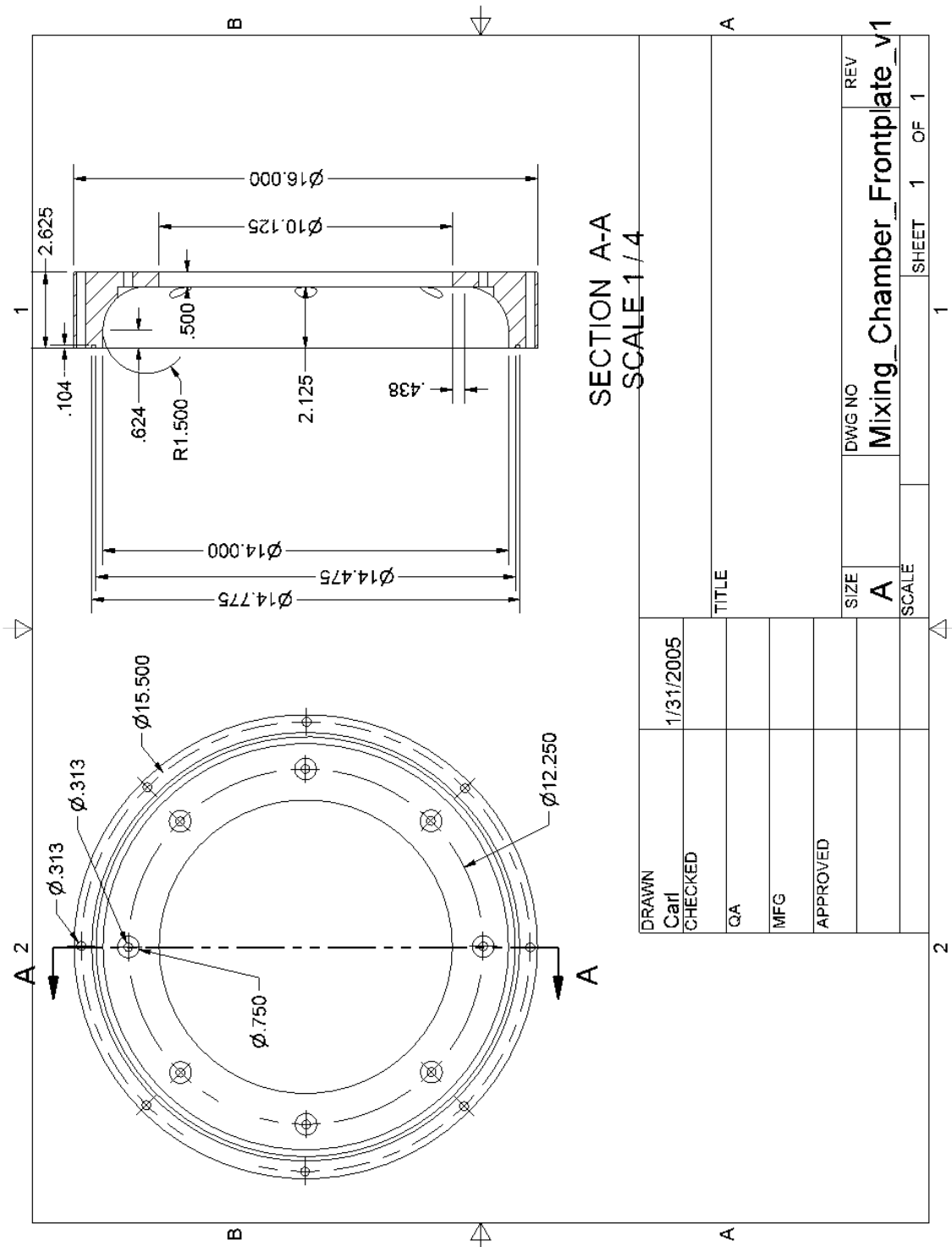
Figure 117. Mixing Chamber Backplate

Figure 118.   Mixing Chamber Frontplate

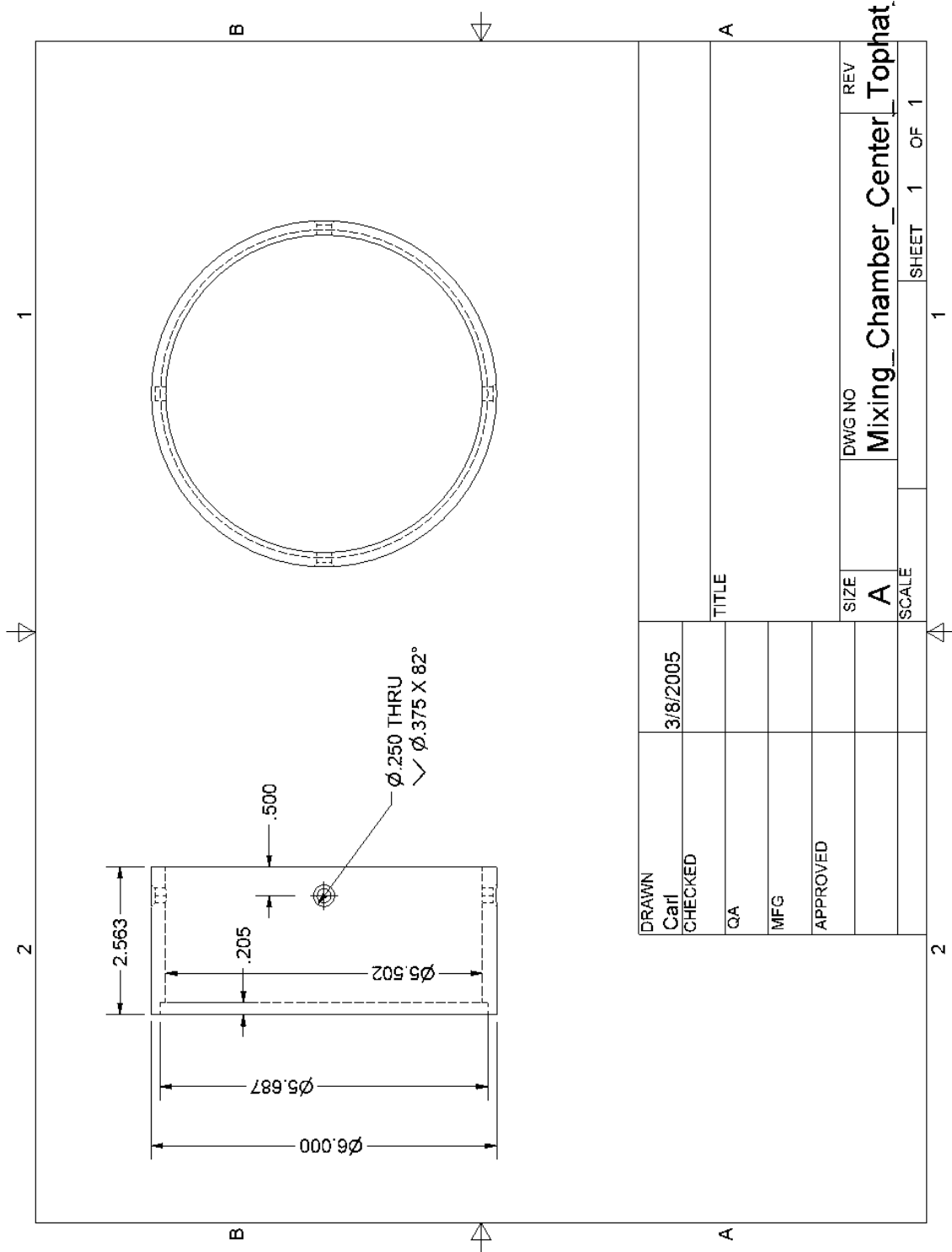Figure 119.   Mixing Chamber to Inner Liner Adaptor "Tophat" Assembly

135

Figure 120.   Mixing Chamber to Inner Liner Adaptor "Tophat" Flange

Figure 121. Mixing Chamber to Inner Liner Adaptor "Tophat" Tube

137
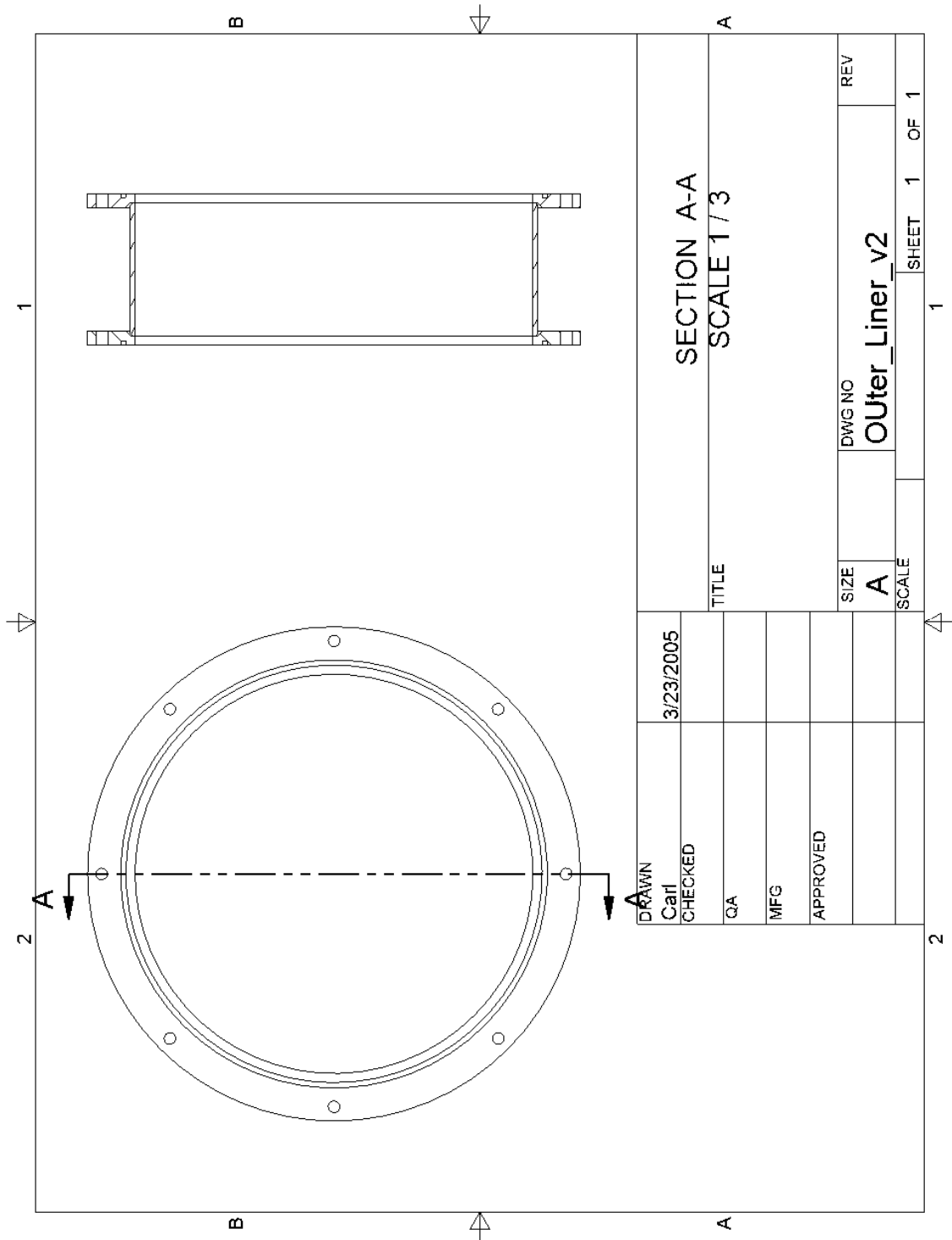
Figure 122.   Flow Conditioning Outer Wall Assembly (2 Flanges&Tube)
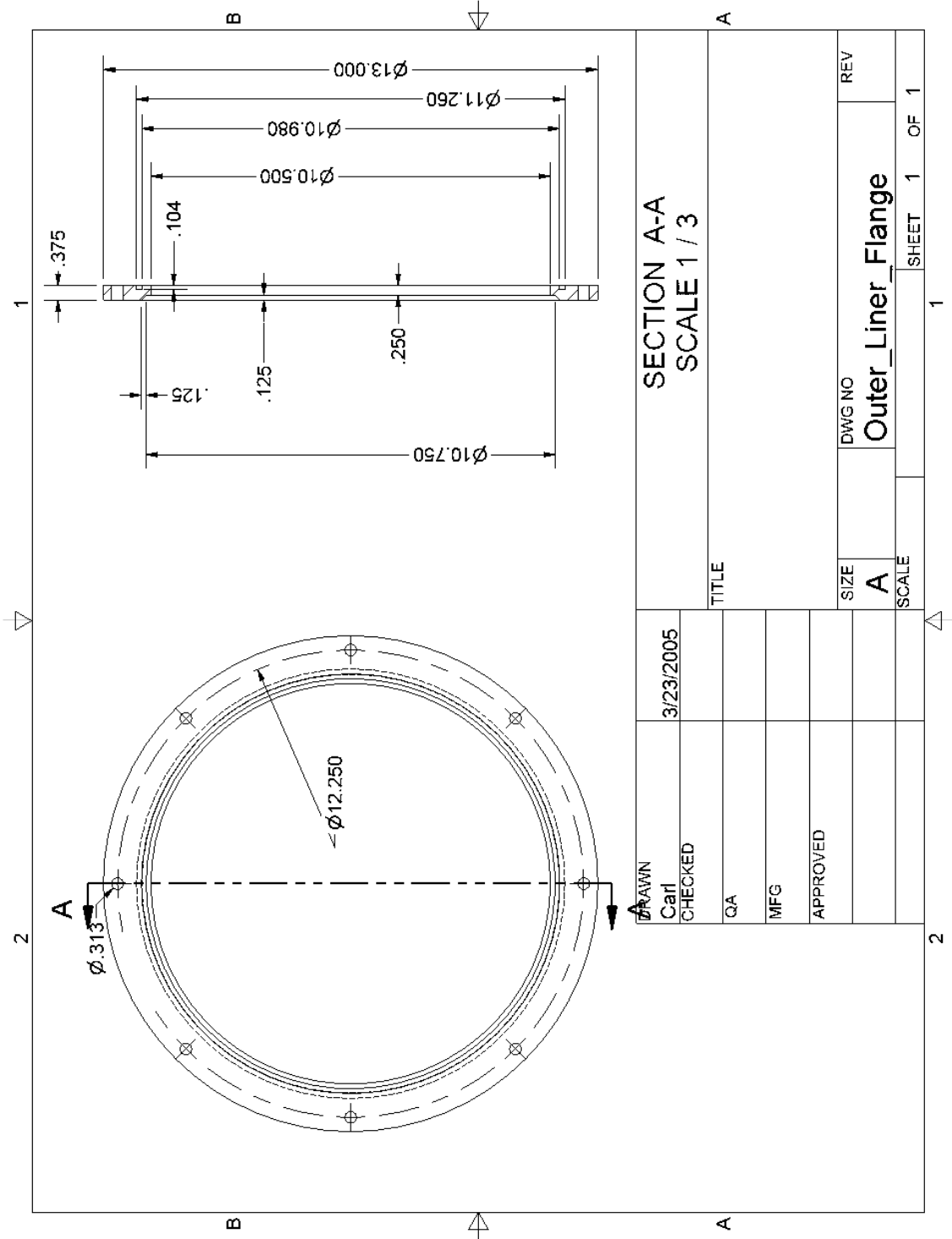
Figure 123. Flow Conditioning Outer Wall Flange

SECTION A-A
SCALE 1 / 3

Ø10.750

.063

.063 .063

3.500

Ø10.500

.063

A

A

DRAWN
Carl
CHECKED

QA

MFG

APPROVED

3/23/2005

TITLE

DWG NO
Outer_Liner_Tube
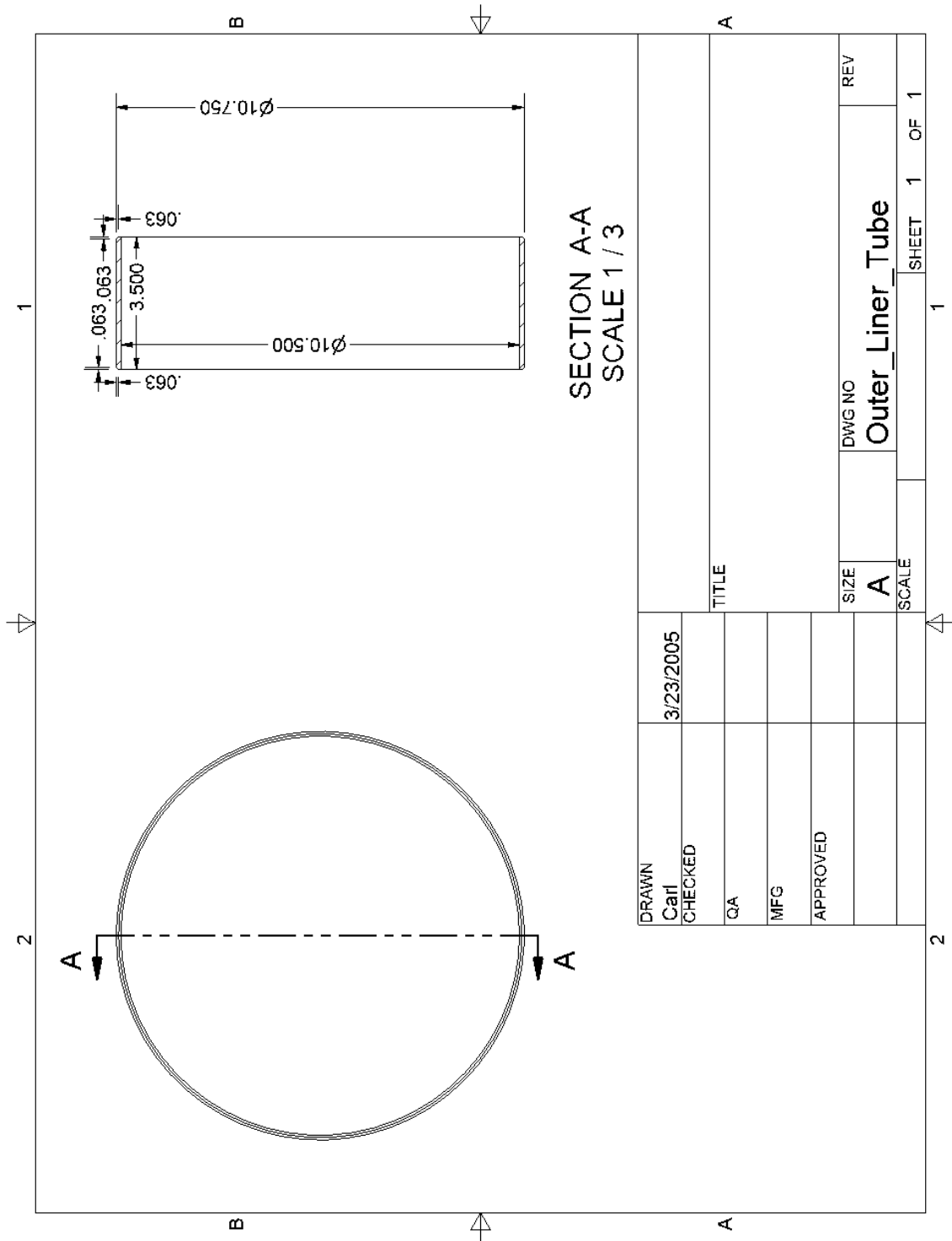
SIZE
A

SCALE

REV

SHEET   1   OF   1

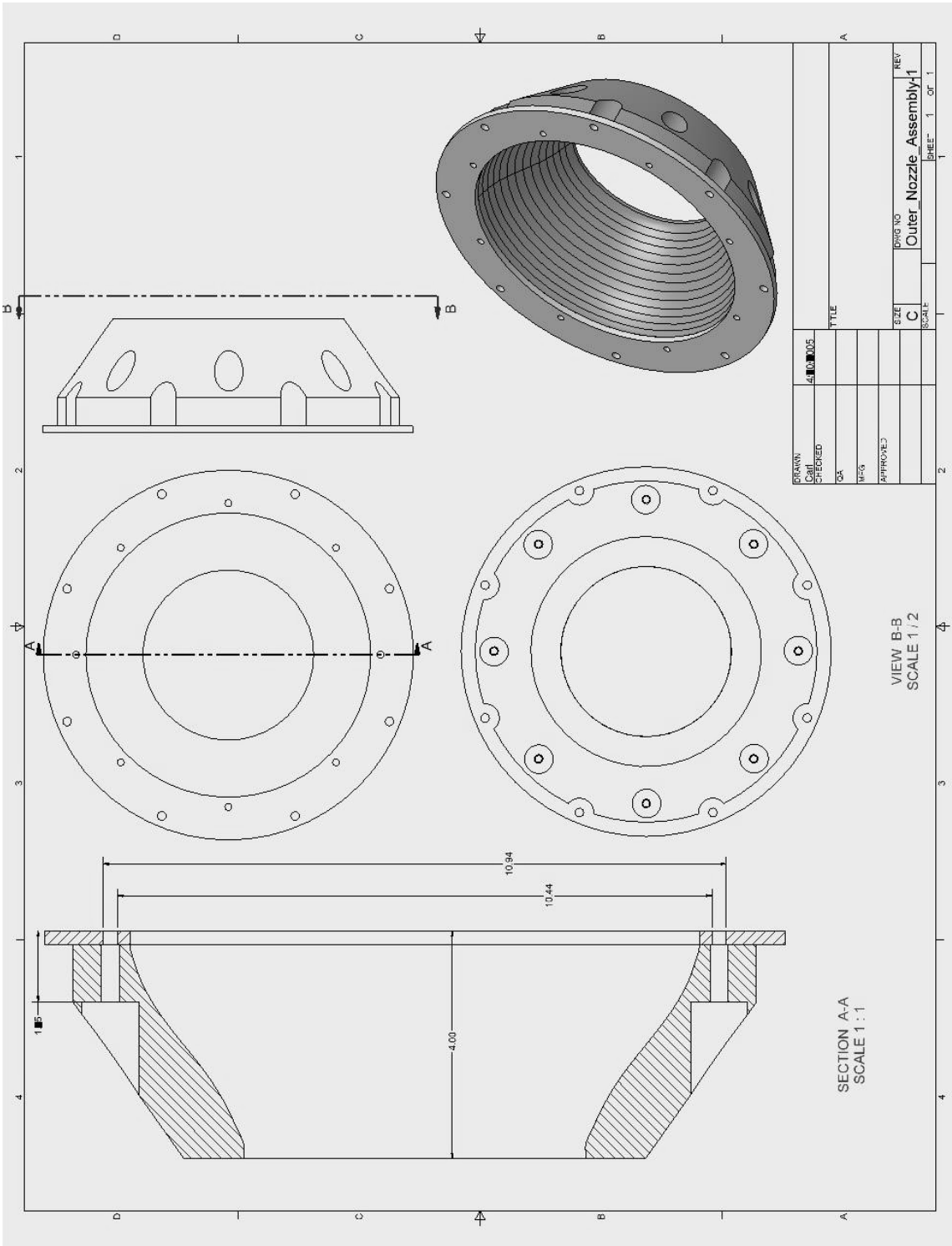Figure 124.   Flow Conditioning Outer Wall Tube

140

Figure 125.   Outer Airflow Nozzle Assembly
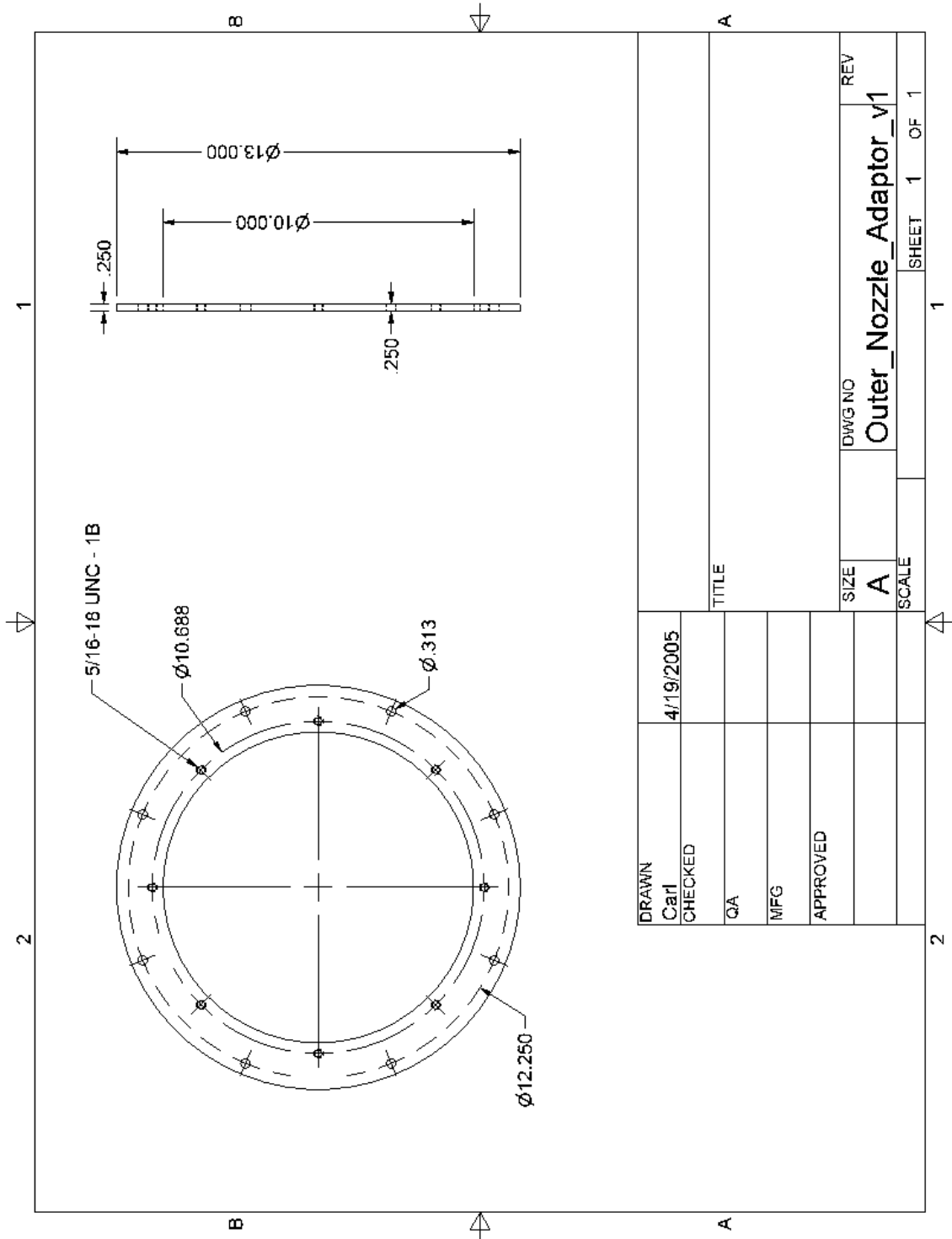
Figure 126.　Outer Airflow Nozzle Adaptor Flange
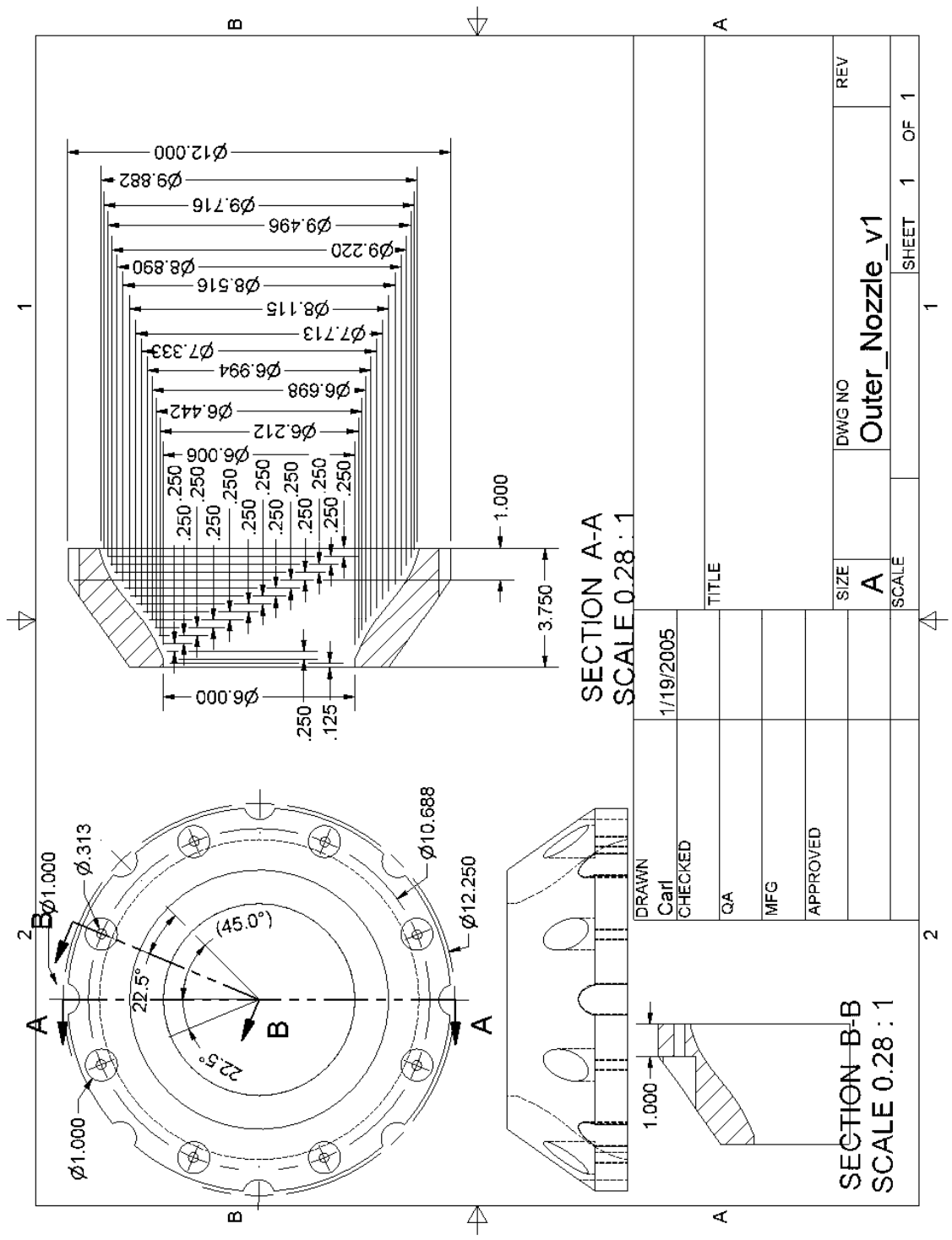
Figure 127. Outer Airflow Nozzle (View 1)
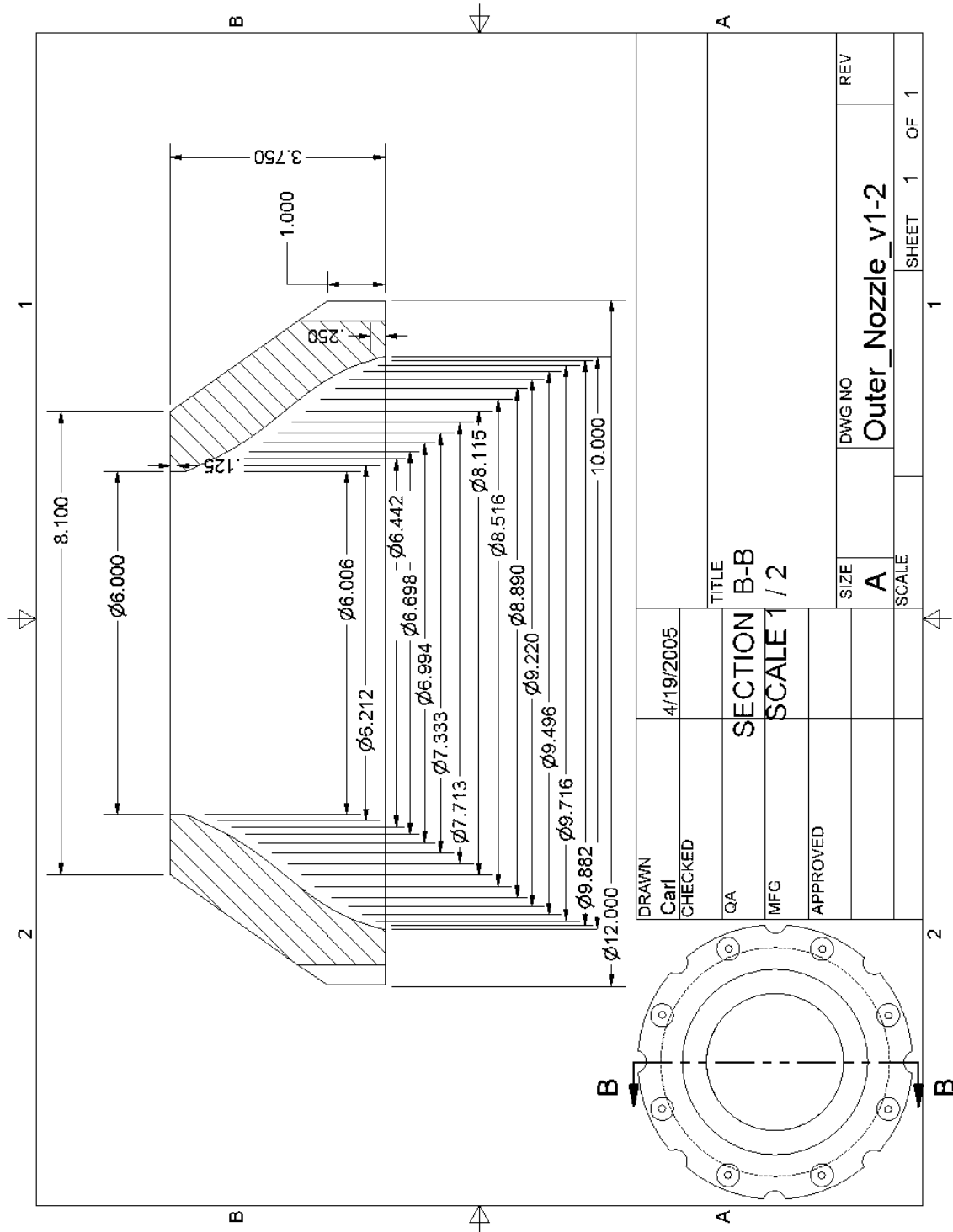
Figure 128. Outer Airflow Nozzle (View 2)

SECTION A-A
SCALE 3 / 4

ø5.250

2.375

7.360

1/4-20 UNC - 1B

1/4-20 UNC - 1B

ø5.500

A

A

DRAWN | Carl | 4/14/2005
CHECKED
QA
MFG
APPROVED

TITLE

DWG NO | Inner_Liner_v1

SIZE | A

SCALE

SHEET | 1 | OF | 1

REV
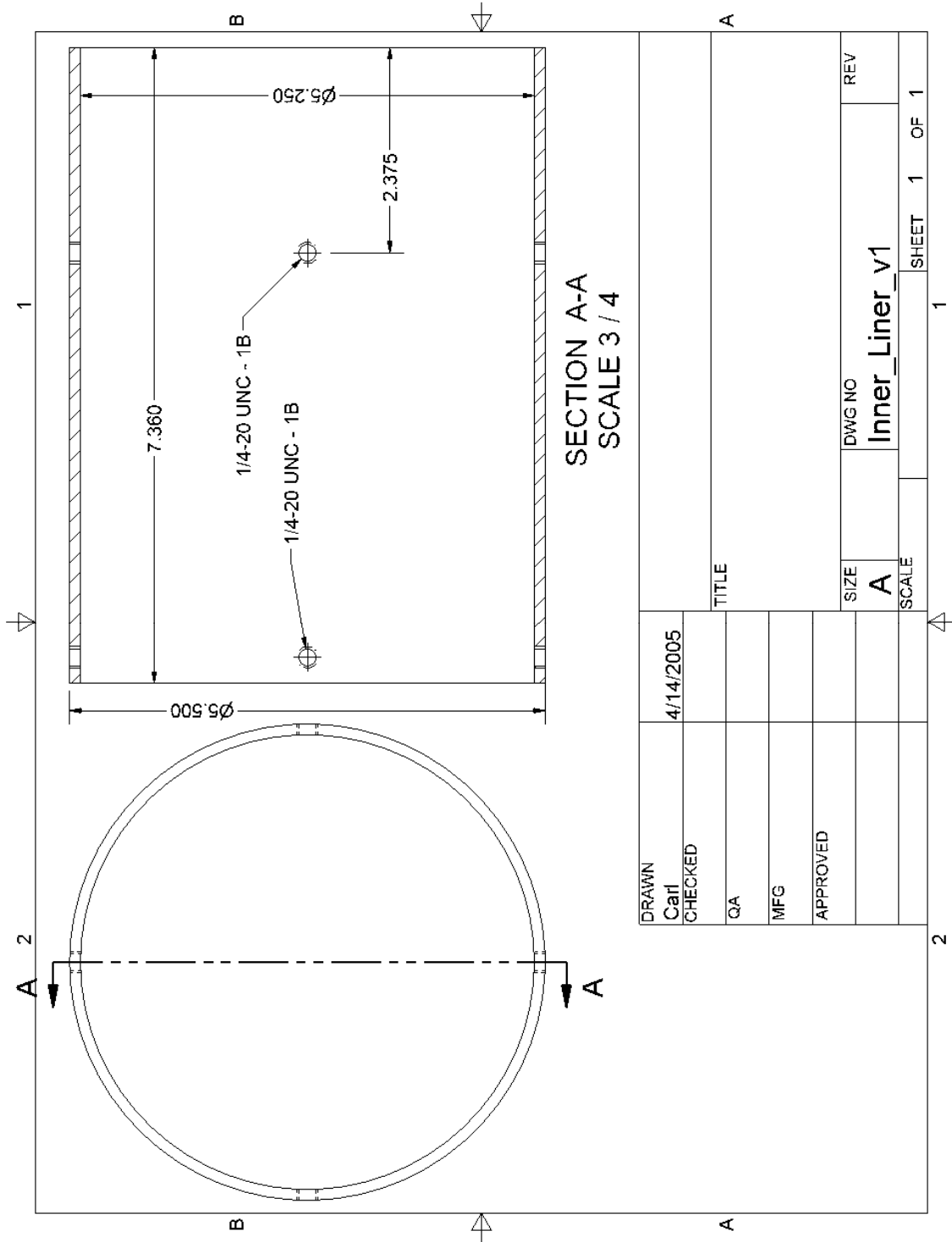
Figure 129.   Flow Conditioning Inner Liner
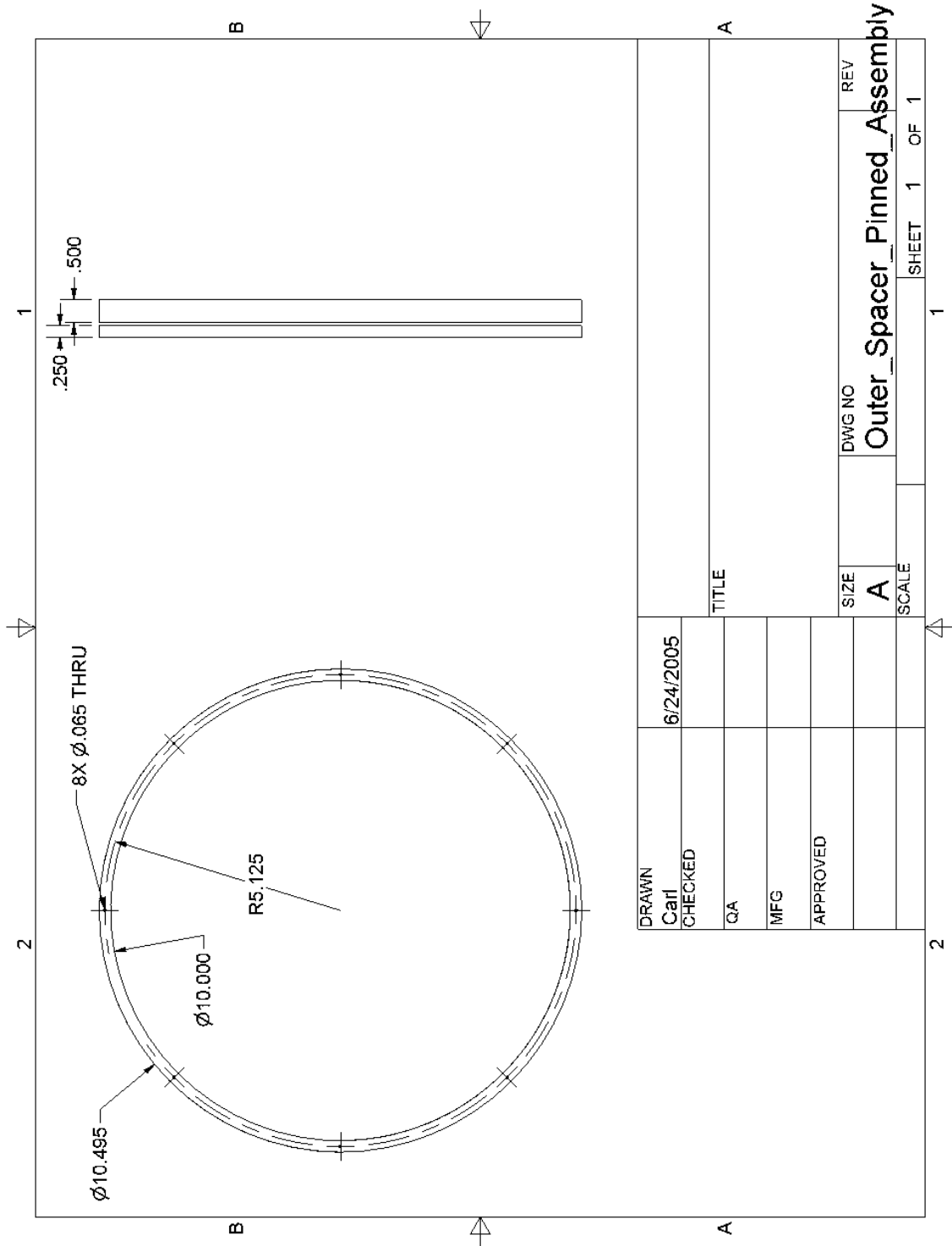
Figure 130.   Flow Conditioning Outer Spacers (3 thick, 1 thin)

Figure 131.   Flow Conditioning Inner Spacers (3 thick, 1 thin)
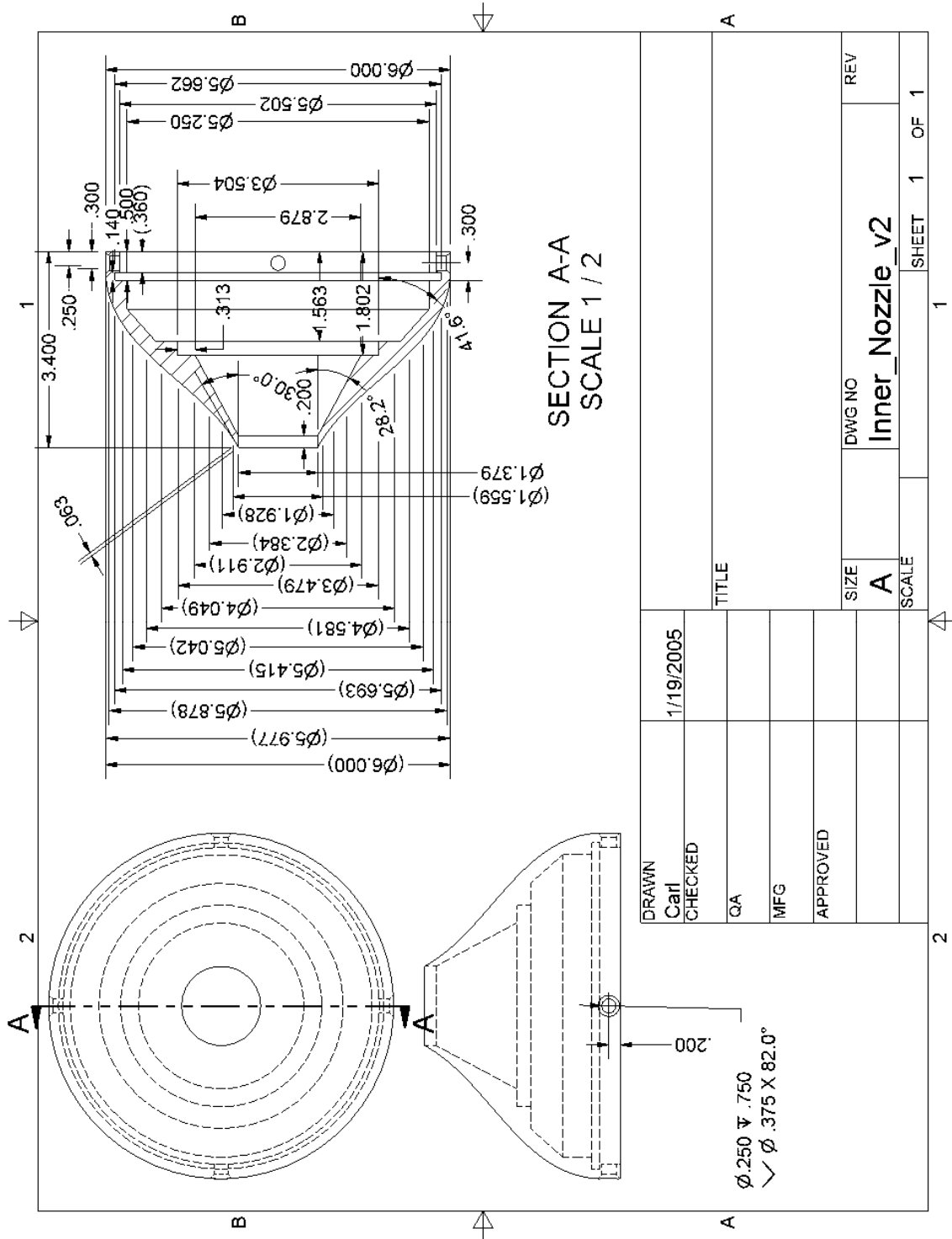
Figure 132.   Inner Airflow Nozzle

Figure 133.   Flow Conditioning: Perforated Cylinder (inside Mixing Chamber)

Note: 51% open 1/16" aluminum, 3/16" holes.

Figure 134. Flow Conditioning: Perforated Plates (x2)

Note: 51% open 1/16" aluminum, 3/16" holes.

Figure 135.   Honeycomb Flow Straightener

Note: ¼" Cell Stainless Steel Honeycomb with 0.008" Wall Thickness, from Indy Honeycomb.

THIS PAGE INTENTIONALLY LEFT BLANK

LIST OF REFERENCES

1.	Sutton, G. P. and Biblarz, O., *Rocket Propulsion Elements*, Seventh Edition, p. 182, John Wiley & Sons, Inc., 2001.

2.	Great Images in NASA, NASA Photographic Online Database, http://grin.hq.nasa.gov/ABSTRACTS/GPN-2000-000065.html, April 2006.

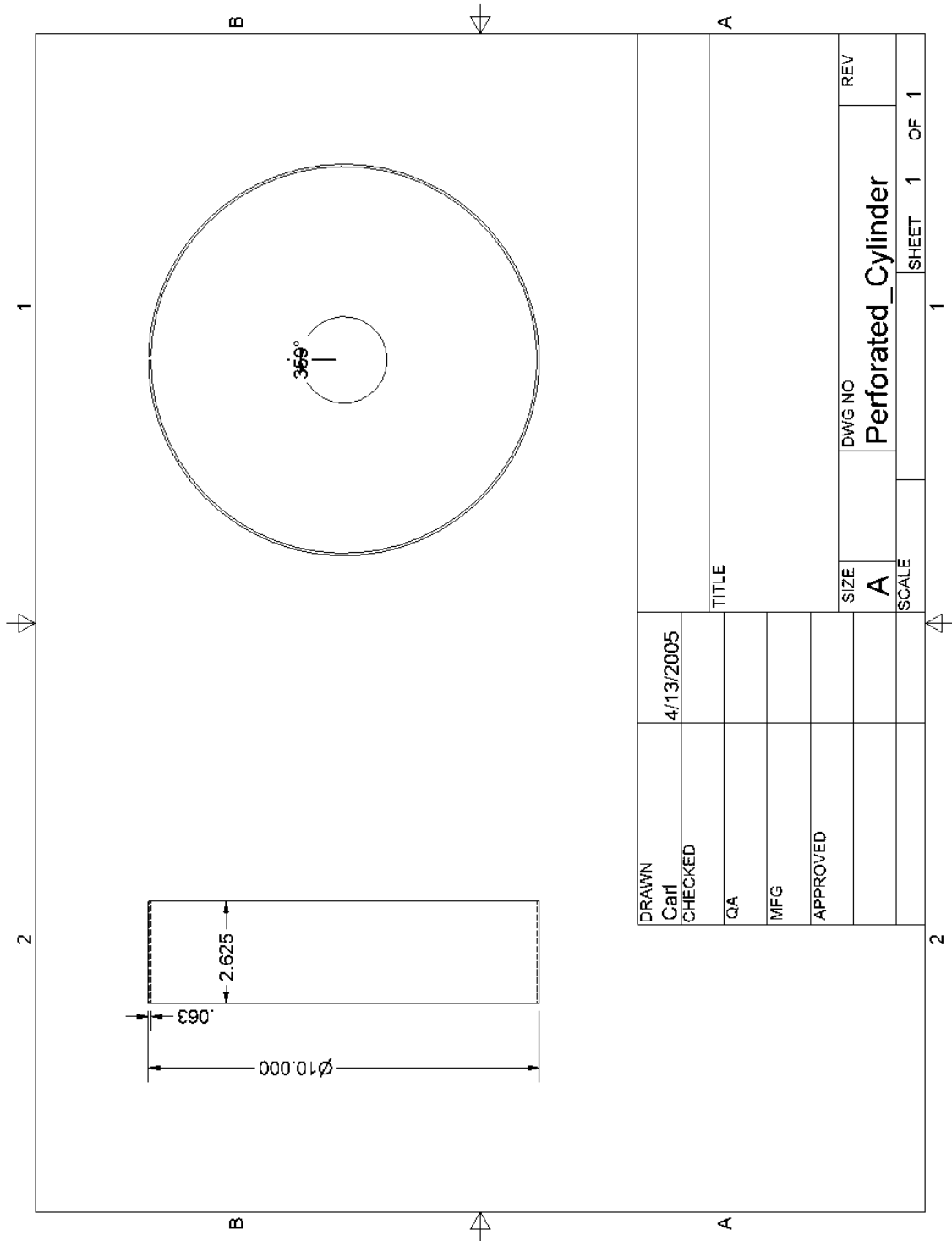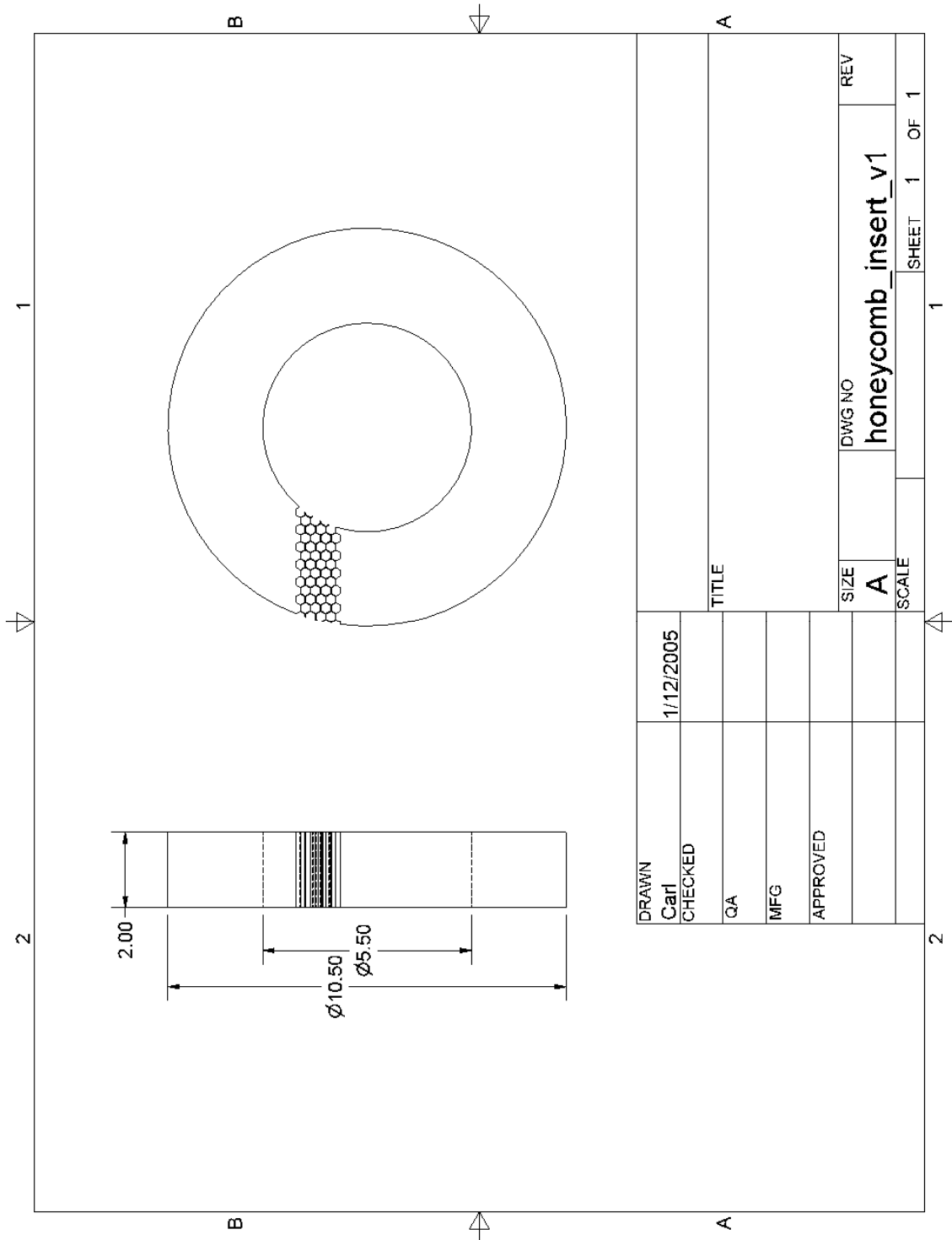3.	Brown, G. L. and Roshko, A., "On Density Effects and Large Structure in Turbulent Mixing Layers," Journal of Fluid Mechanics (1974) Vol. 64, pp. 775-816.

4.	Papamoschou, D. and Roshko, A., "The Compressible Turbulent Shear Layer: an Experimental Study," Journal of Fluid Mechanics (1988) Vol. 197, pp. 453-477.

5.	Tennekes, H. and Lumley, J.L., *A First Course in Turbulence*, pp. 133-135, The MIT Press, 1972.

6.	Glassman, I., *Combustion*, pp. 465-471, Academic Press, 1987.

7.	California Institute of Technology, Explosion Dynamics Laboratory Webpage, http://www.galcit.caltech.edu/EDL/public/flammability.html, March 2006.

8.	Bogdanoff, D. W., "Compressibility Effects in Turbulent Shear Layers," AIAA Journal Vol. 21, No. 6, 1983, pp. 925-926.

9.	Nixon, D. and Keefe, L., "Controlling Combustion and Maximizing Heat Release in a Reacting Compressible Free Shear Layer," AFOSR Contract F49620-91-0020, 1994.

10.	Nixon, D., "The Effects of Compressibility on a Supersonic Mixing Layer," AFOSR Contract F49620-88-0023, 1990.

11.	Nixon, D. and Keefe, L., "The Effect of Heat Release on a Compressible Free Shear Layer," AIAA Paper 92-0181, 30th Aerospace Sciences Meeting & Exhibit, January 1992.

12.	Murakami, E. and Papamoschou, D., "Mean Flow Development in Dual-Stream Compressible Jets," AIAA Journal, Vol. 40, No. 6, June 2002.

13.	Schadow, K. C., Gutmark, E., and Wilson, K. J., "Compressible Spreading Rates of Supersonic Coaxial Jets," Experiments in Fluids, vol 10, pp. 161-167, 1990.

14.	Seiner, J. M., "Advances in High Speed Jet Aeroacoustics," AIAA Paper 84-2275, AIAA/NASA 9th Aeroacoustics Conference, October 1984.

15.   Glassman, I., *Combustion*, pp. 298-308, Academic Press, 1987.

16.   _____. *Combustion*, pp. 472-485, Academic Press, 1987.

17.   Pergament, H. S., Dash, S. M., and Varma, A. K., "Evaluation of Turbulence Models for Rocket and Aircraft Plume Flowfield Predictions," Naval Weapons Center Contract Number N00123-78-0010, February 1979.

18.   Simmons, F. S., *Rocket Exhaust Plume Phenomenology*, pp. 21-22, The Aerospace Press, 2000.

19.   Sutton, G. P. and Biblarz, O., *Rocket Propulsion Elements*, Seventh Edition, p. 188, John Wiley & Sons, Inc., 2001.

20.   Personnal Communication, Warren T. Peters, NASA Marshal Space Flight Center, Combustion Devices, August 2006.

BIBLIOGRAPHY

Calhoon, W. H. Jr., "Computational Assessment of Afterburning Cessation Mechanisms in Fuel Rich Rocket Exhaust Plumes," AFRL Report, Contract # F04611-96-C-0001, December 4, 1998.

_____. "Evaluation of Afterburning Cessation Mechanisms in Fuel Rich Rocket Exhaust Plumes," AIAA 98-3618, 34th AIAA/ASME/SAE/ASEE Joint Propulsion Conference & Exhibit, July 13-15, 1998.

Gurevich, M. I., *Theory of Jets in Ideal Fluids*, Academic Press, 1965.

Gutmark, E., Schadow, K. C., and Bicker, C. J., "Mode Switching in Supersonic Circular Jets," Physics of Fluids A 1 (5), May 1989, pp. 868-873.

Kovasznay, L. S. G., "Turbulence in Supersonic Flow," Journal of the Aeronautical Sciences, Vol. 20, No. 10, October 1953.

Miller, M.F., Island, T. C., Seitzman, J. M., Bowman, C. T., Mungal, M. G., and Hanson, R. K., "Compressibility Effects in a Reacting Mixing Layer," AIAA-93-1771, 29th AIAA/ASME/SAE/ASEE Joint Propulsion Conference and Exhibit, June 28-30, 1993.

Miller, M. F., Island, T. C., Yip, B., Bowman, C. T., Mungal, M. G., and Hanson, R. K., "An Experimental Study of the Structure of a Compressible, Reacting Mixing Layer," AIAA-93-0354, 31st Aerospace Sciences Meeting & Exhibit, January 11-14, 1993.

Narayan, J. R., "Effect of Turbulence-Chemistry Interactions in Compressible Reacting Flows," AIAA 94-2311, 25th AIAA Fluid Dynamics Conference, June 20-23, 1994.

Pergament, H. S, and Jensen, D. E., "Influence of Chemical Kinetic and Turbulent Transport Coefficients on Afterburning Rocket Plumes," Journal of Spacecraft, Vol. 8, No. 6, June 1971.

Roshko, A., "Structure of Turbulent Shear Flows: A New Look," AIAA Journal, Vol. 14, No. 10, October 1976.

Watanabe, S. and Mungal, M. G., "Velocity Field Measurements of Mixing-Enhanced Compressible Shear Layers," AIAA 99-0088, 37th AIAA Aerospace Sciences Meeting and Exhibit, January 11-14, 1999.

THIS PAGE INTENTIONALLY LEFT BLANK

INITIAL DISTRIBUTION LIST

1.   Defense Technical Information Center
        Ft. Belvoir, Virginia

2.   Dudley Knox Library
        Naval Postgraduate School
        Monterey, California

3.   Anthony J. Healey
        Naval Postgraduate School
        Monterey, California

4.   Knox T. Millsaps
        Naval Postgraduate School
        Monterey, California

5.   Christopher M. Brophy
        Naval Postgraduate School
        Monterey, California

6.   Garth V. Hobson
        Naval Postgraduate School
        Monterey, California

7.   Robert G. Hutchins
        Naval Postgraduate School
        Monterey, California

8.   Oscar Biblarz
        Naval Postgraduate School
        Monterey, California

9.   Marty J. Venner
        Air Force Research Laboratory, Propulsion Directorate
        Edwards Air Force Base, California

10.   Thomas Smith
        Air Force Research Laboratory, Propulsion Directorate
        Edwards Air Force Base, California